Improving the calibration of MainzTPC using the isotope ^{37}Ar

von

Daniel Wenz

Masterarbeit in Physik
vorgelegt dem Fachbereich Physik, Mathematik und Informatik (FB 08)
der Johannes Gutenberg-Universität Mainz
am 11. Mai 2018

1. Gutachter: Prof. Dr. Uwe Gerd Oberlack
2. Gutachter: Prof. Dr. Josef Pochodzalla

Ich versichere, dass ich die Arbeit selbstständig verfasst und keine anderen als die angegebenen Quellen und Hilfsmittel benutzt sowie Zitate kenntlich gemacht habe.

Mainz, den

Daniel Wenz[1]
ETAP/XENON
Institut für Physik
Staudingerweg 7
Johannes Gutenberg-Universität D-55099 Mainz

[1] dwenz@students.uni-mainz.de

TABLE OF CONTENTS

LIST OF ACRONYMS

APD Avalanche Photodiode

CAD computer aided design

CMB Cosmic Microwave Background

DAQ Data Acquisition

DM Dark Matter

EC electron capture

ER electronic recoil

ESA European Space Agency

FADC flash analog-to-digital converter

GXe gaseous xenon

IC internal conversion

ISM interstellar medium

JGU Johannes Gutenberg-Universität Mainz

LAr liquid argon

LED light-emitting diode

LET linear energy transfer

LN2 liquid Nitrogen

LXe liquid xenon

MAW Moving Average Window

MOND Modified Newtonian dynamics

MWI Moving Window Integrator

NaN not a number

NEST Noble Element Simulation Technique

NIM Nuclear Instrumentation Module

NR nuclear recoil

PAX Processor for Analyzing XENON

PCB printed circuit board

PCI Peripheral Component Interconnect

PEEK Polyether ether keton

PMT photomultiplier tube

PTFE polytetrafluoroethylene

PTR Pulse-Tube Refrigerator

Q.E. quantum efficiency

R'n'D Research and Development

SCS Slow Control System

SiPM Silicon Photomultiplier

TeVeS Tensor–vector–scalar gravity

TPC time projection chamber

UTI Universal Transducer Interface

VME Versa Module Eurocard

VUV vacuum ultraviolet

WIMP weakly interacting massive particle

XML Extensible Markup Language

LIST OF FIGURES

LIST OF TABLES

INTRODUCTION

Since the initial idea by Luis W. Alvarez et al., in 1968 liquid noble gas detectors developed in the last five decades to a well-established detector type for rare event experiments such as neutrinoless double β-decay ($0\nu\beta\beta$), the standard model forbidden $\mu \rightarrow e\gamma$ decay and the direct search for Dark Matter (DM). Especially in the business of direct search of weakly interacting massive particle (WIMP) dark matter, the xenon dual-phase time projection chamber (TPC) adopted by experiments like LUX, PandaX and XENON has become the leading detector technology. These detectors are counting the scintillation light and ionization produced by a particle interaction with the liquid xenon. This provides accurate information about the deposit energy and type of the particle as well as a spatial information about the interaction side. While the technical aspects are improving with each new generation of these detectors, also their size and sensitive mass grow. This allows to exploit the excellent self shielding properties of liquid xenon in order to suppress the background from natural radioactivity and become more sensitive to WIMP interactions.

It is necessary to calibrate the liquid xenon and detector response with well known calibration sources as a reference for the unknown particle understudy. However due to the self shielding properties of large scale LXe detectors an adequate and homogeneous calibration of the detector response becomes more challenging with each new detector generation. Especially "classical" calibration sources like ^{137}Cs shining from the outside of the detector are absorbed within the very first layers of liquid xenon leading to a very localized calibration of the detector. This becomes even worse for lower particle energies. For WIMP interactions many theoretical models expect a exponentially falling signal spectrum with a mean energy of a few keV. Hence new calibration methods using *in situ* calibration sources inside the detector are currently widely understudy in the DM community. Gaseous calibration sources which can be introduced and removed from LXe are especially interesting. In this context the isomer ^{83m}Kr with its mono-energetic transitions of 9.4 keV and 32.1 keV represents the stated of the art for mono-energetic low energy calibration sources.

Joining this effort also the isotope ^{37}Ar is studied for an usage as a calibration source in the XENON1T and XENONnT experiment. ^{37}Ar decays via electron capture (EC) and is followed by the emission of a cascade of Auger electrons and X-rays. These Auger electrons and X-rays sum up to two mono-energetic lines and allow to calibrate the detector response down to an energy of 2.8 keV and 0.27 keV. Due to the very short attenuation length of these emissions a spatial dilution of the ^{37}Ar gas into the entire LXe volume is important and must be proved.

This thesis discusses the measurement of a ^{37}Ar sample with the MainzTPC, a small-size dual-phase LXe TPC which was designed for the study of the LXe response of low energetic interactions. At the start of this thesis, the MainzTPC has been rebuilt after a measurement campaign at the neutron time-of-flight facility nELBE at the Helmholtz Institut Dresden-Rossendorf. An initial test run after the reconstruction of the MainzTPC was used to calibrate and prepare the MainzTPC for the ^{37}Ar measurement. Moreover the feasibility of the detector to measure the low energetic events of ^{37}Ar was investigated. The injection of the ^{37}Ar calibration gas was done with a sub-system of the MainzTPC gas-system, the so-called dosimetry branch. This branch is equipped with a photomultiplier tube (PMT) to estimate the sample activity before its injection. With this branch a dosing concept and filling procedure for the ^{37}Ar was developed. The ^{37}Ar sample itself was produced in cooperation with the Nuclear Chemistry of the Johannes Gutenberg-Unversität Mainz.

Additionally several hardware issues were addressed. The liquid level experience periodic drops whose origin was so far not understood. In this context during a maintenance of the MainzTPC and its gas-system the spillway for the liquid level adjustment was replaced with a newer version to improve the stability of the level. Additionally a comparative study of the liquid level fluctuations for the new and old spillway shows that the stability of the liquid level did not improve.

The results presented in this thesis show that the MainzTPC is capable to measure the 2.8 keV transition of ^{37}Ar. Moreover a spatial diffusion of the ^{37}Ar isotope into liquid xenon is observed. This opens the way for having ^{37}Ar as a calibration source in the XENON1T experiment.

The thesis is organized as in the following: Chapter 1. deals with theoretical fundamentals for this thesis. It introduces DM and WIMPs. Furthermore the basic concepts of liquid noble gases as a detector medium and the working principle of dual-phase TPCs are explained. Additionally a summary about so far used gaseous calibration sources is given and the isotope ^{37}Ar is introduced and placed in this context. Subsequent Chapter 2. discusses the MainzTPC experiment and gives an overview about the MainzTPC itself, all relevant subsystems like cryogenics and electronics as well as an overview about the gas-system of the MainzTPC and the dosimetry branch. Chapter 3. discusses the measurements which were performed and which actions had to be taken to achieve those. Afterwards Chapter 4. presents and discusses the results of the preparations for the ^{37}Ar run and the ^{37}Ar measurement itself. In the end in Chapter 5. a short summary is given as well as a conclusion of the measurements. Additionally a short list for future improvements is recommended.

CHAPTER 1

THEORETICAL FUNDAMENTALS

1.1 DARK MATTER

Also in the new astronomic age of the multi-messenger observation the missing mass or Dark Matter problem remains unsolved. Many astronomical and cosmological observations indicate that a new type of particle/particles beyond the Standard Model must exist. In the following section some of these evidences are summarized and presented. Moreover some important information about the WIMP are reported.

1.1.1 *Evidences*

Through the last nine decades astronomers collected a variety of different evidences for the existence of so-called Dark Matter. These evidences were observed at different scales and times (redshifts) of the universe. The lower end of the scale starts with small sized objects like galaxies, continues with larger and more mass rich structures like galaxy clusters and ends out the scale of the entire universe. In the following some of these evidences are presented.

The first and oldest evidences for the missing mass or DM problem arose from the observations of the movement of stars and gas-clouds in galaxies as well as the movement of galaxies in galaxy clusters. Due to the great success of Keplers laws and the later by Isaac Newton derived law of gravity for the prediction of the planetary movement in our own solar system, astronomers thought that this would also hold true for the movement of stars in galaxies or the movement of galaxies in a cluster [Kap18]. Already in 1933 Fritz Zwicky and the Mt. Palomar observatory showed by applying the verial theorem to eight galaxies of the Coma Cluster, that their tangential velocities are not matching with the luminous mass of the cluster. However it took another 40 years until Vera Rubin showed, that the missing mass problem is a regular feature of galaxies [Zac07, UR16]. By using the Doppler shift of the H_α emission line, she studied the tangential velocity distribution of the interstellar medium as a function of the radial distance towards the galactic center in over 60 different galaxies. Based on Newtons law of gravity and assuming, that the major fraction of the galaxy mass M is

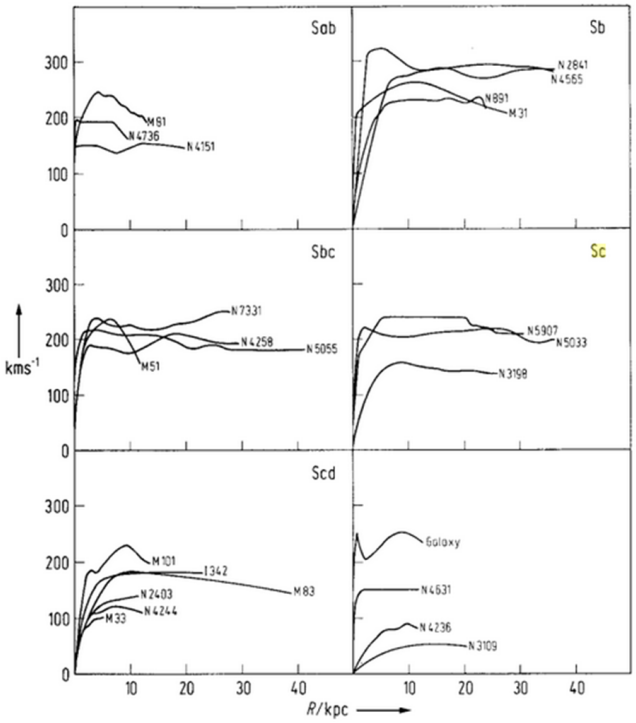

Figure 1.1 – *Rotational velocities as a function of the galaxy radius for different galaxy types. The galaxy type is indicted in the upper right corner of each plot. The galaxy names are written next to the curves [HvR09].*

concentrated in the bulge region a tangential velocity distribution according to

$$\frac{mv^2}{r} = G\frac{m \cdot M}{r^2}$$
$$v(r) = \sqrt{\frac{G \cdot M}{r}}, \tag{1.1}$$

was expected. However instead of the expected $v \propto r^{-1/2}$ proportionality they found that the tangential velocity stays constant outside of the bulge region. In other words this means that the mass distribution outside of the bulge region scales linearly with the radius r [UR16]. Some rotation curves of different galaxy types are shown in Figure 1.1.

These observations allow to set-up first constraints to the missing mass or DM problem. Since DM seems to be non-luminous in any region of the electromagnetic spectrum it has to be electrical neutral. Further is its density 100 to 1000 times higher than the average density of the ISM in a galaxy [HvR09].

An additional observation which discards non-luminous matter as an explanation for the missing mass problem is the observation of the weak gravitational lensing in the aftermath of the so-called Bullet Cluster (1E0657-56) [Ber10].

Gravitational lesning was predicted by Einstein in his theories of General Relativity

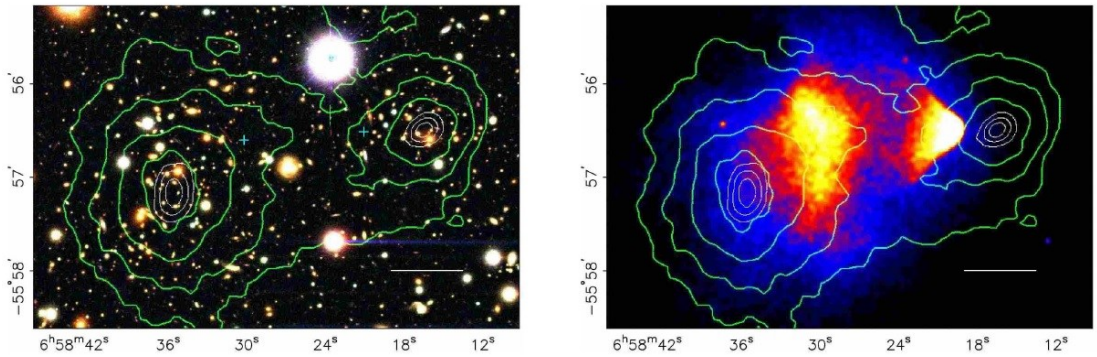

Figure **1.2** – *Two pictures of the Bullet Cluster. The picture on the left hand side shows the bullet cluster in the optical range of electromagnetic spectrum measured by the Hubble space telescope, while the picture on the right hand side shows the x-ray emissivity measured by the Chandra X-ray Observatory. The x-ray emissions have their origin in the baryonic gas clouds which were heated up during the cluster collision. The green contours indicate lines of equal deflection from the weak lensing. The white oval indicate the overall mass fraction centers of 68.3 %, 95.5 % and 99.7 % for the cluster. The grey bar indicates a distance of* 200 *kpc [Ber10, Ald18].*

and provides a strong tool, that allows cosmologists to probe the mass-to-light ratio of many galaxies and galaxy clusters. Gravitational lensing is caused by very massive objects which are in the line of sight between an observer and the object under study. The high mass of these intermediate objects curve the geodecis of space-time and lead to a deflection of the light on its path towards the observer. The result is a distorted image or multiple occurrence of the lensed background object. In the case of the strong lensing effect the distorted image can even have an arc or ring like structure, so-called Einstein rings. Measuring the strength of the deflection determined by the deflection angle the total mass of the lens can be calculated. For a variety of galaxy clusters a typical mass-to-light ratio of 400 was measured [Ber10, UR16].

Observations of the weak lensing effect in cluster collisions allows to discard non-luminous baryonic matter like gas-clouds of the interstellar medium (ISM) as a solution for the missing mass problem. The most famous example of such a collision is the so-called Bullet Cluster 1E0657-56 shown in Figure **1.2**. The picture on the right hand side of Figure **1.2** shows the Bullet Cluster in the x-ray regime of the electromagnetic spectrum. It unveils an offset between the galaxy cluster centers and the gas clouds of the inter stellar medium. While the galaxy clusters and mass centers passed nearly collisionless through each other, ordinary baryonic matter got stuck and heated up in between the two clusters due to their interaction through the electromagnetic force. Hence this separation of non-luminous ordinary matter from the mass centers of the lenses and the measured mass-to-light and gas-to-total-mass ratios are a strong evidence for the non-baryonic nature of DM. Further these observations allow to set-up constraints for the self interaction corss-section of DM [Ber10]. Already 72 cluster collisions of these kind were studied all leading to similar results [UR16].

One remaining question is, if a wrong understanding of gravity itself could be an explanation for this observations. This argument is historically motivated by the prediction of the planetary movement of Mercury. It took about 200 years until astronomers

understood, that the faster movement of Mercury compared to the predictions by Newtons law of gravity are caused by effects of Einstein's general relativity and a modification of the until then valid law of gravity. Today, theories like MOND or Tensor–vector–scalar gravity (TeVeS) are also able to explain the lensing effects and the rotational curves [Ber10]. Also the question: "Why are there no galaxies with a lower or even without any DM content?" leave a little doubt on the particle DM theory. Although these doubts can be eliminated through observations of the Cosmic Microwave Background (CMB) and structure formation on an universal level, first the very recently published (29. March 2018) observation of a galaxy which is lacking of dark matter [vD+18] is discussed here first.

Based on observations of rotational curves and gravitational lensing it can be shown that the mass of the DM content M_{halo} and the total stellar mass M_{stars} are correlated to each other. However in [vD+18] it is demonstrated, that this is not true for the ultra-diffuse galaxy NGC1052-DF2. The tangential velocity of ten cluster like objects in NGC1052-DF2 were studied. From their velocity dispersion a total mass M_{total} of $3.4 \cdot 10^8\,M_\odot$ ($M_\odot \doteq$ solar mass) was calculated. The stellar mass of NGC1052-DF2 is about $2 \cdot 10^8\,M_\odot$ leading to a M_{halo}/M_{stars}[1] of almost one which is a factor of atleast 400 lower than expected. Hence the absence of DM in NGC1052-DF2 shows the complementary of the Bullet Cluster. It proofs that DM can be separated from baryonic matter and therefore falsifies alternative gravity theories like MOND or TeVeS. Although it prompts some new questions about its formation history and if there are more objects like NGC1052-DF2 which are lacking of DM.

An evidence for particle DM on the universal scale can be found in the CMB or structure formation of the universe. The CMB represents the surface of last scattering when the universe became transparent to photons. It follows very accurately the spectrum of a black-body with a temperature of 2.726 K and has anisotropies only in the order of micro Kelvin[2]. These little temperature anisotropies contain information about the late-time evolution of the universe its geometry and content. The latest and most accurate measurements of the CMB were performed by the Planck satellite of the European Space Agency (ESA). A picture of the µK anisotropies of the CMB measured by Planck is shown in the upper picture of **1.3**. These anisotropies can be explained by density fluctuations in the baryon-photon-fluid, in which denser spots corresponds to a slightly hotter spot in the CMB and vise versa [GBS05, UR16, Zac07]. As any scalar field on a sphere can be expanded as a series of spherical harmonic multipoles the anisotropies of the CMB are usually expressed as

$$\frac{\delta T}{T}(\theta,\phi) = \sum_{l=2}^{+\infty} \sum_{m=-l}^{+l} a_{l,m} Y_{l,m}(\theta,\phi)\,, \tag{1.2}$$

where $Y_{l,m}(\theta,\phi)$ are the spherical harmonics [GBS05]. This term expresses the angular coherence of a temperature fluctuation and results in a power law spectrum which is shown in the lower plot of Figure **1.3**.

[1] The upper limit of M_{halo} is $1.5 \cdot 10^8\,M_\odot$ with a confidence level of 90 %

[2] After subtracting the anisotropy caused through the motion of the earth with respect to the rest frame of the milky way.

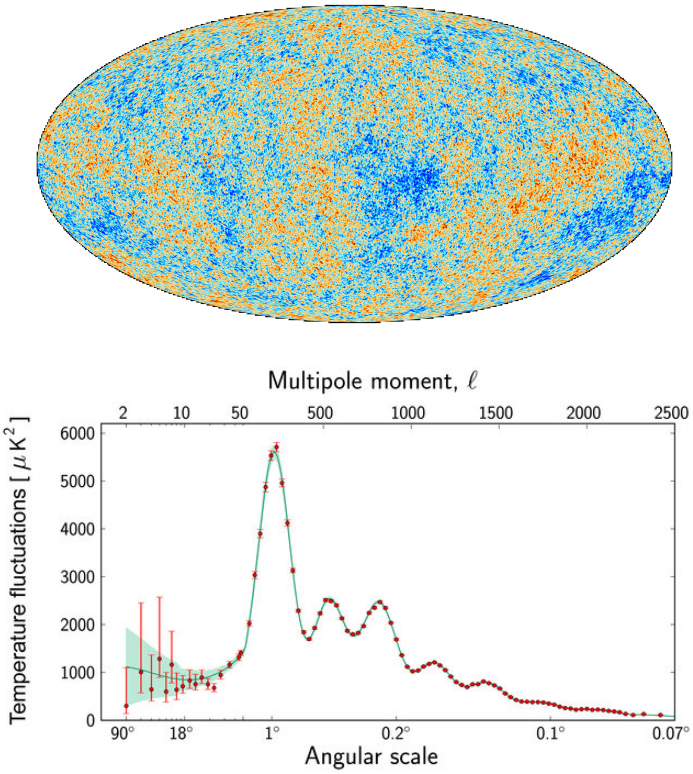

Figure 1.3 – *Micro-Kelvin fluctuations of the Cosmic Microwave Background and the resulting power-spectrum of the multipol-expansion. The upper picture shows the CMB measured by the Planck satellite. The lower plot shows the resulting power-spectrum of the temperature fluctuations. The fitted line represents the best-fit of the ΛCDM model[ESA, Col16].*

From the relative height and position of the so-called acoustic peaks of the power spectrum one can determine a variety of different cosmological parameters by calculating the best fit-parameters for a given model. The cosmological model which fits best is the so-called ΛCDM-model where Λ represents the dark energy or cosmological constant and CDM stands for cold dark matter. This model has usually 6 or 7 parameters whose affect on the relative peak position and height can be seen in Figure 5.1 of the Appendix A. on page 113. Based on the Planck results from the year 2015 [Col16] it can be shown that we are living in a flat-universe with a baryon fraction of $\Omega_B = 0.049$, a dark matter fraction of $\Omega_{DM} = 0.265$ and a fraction of $\Omega_\Lambda = 0.686$ for dark energy [UR16]. These values are in a good agreement with boundaries coming from other observations such as the Big Bang nucleosynthesis which yields $\Omega_B = 0.044 \pm 0.007$ [Zac07], or boundaries coming from the detailed study of the rotational curves and gravitational lensing.

The terminus "cold" dark matter in the ΛCDM model refers to the fact that dark matter particles have to be non-relativistic in order to be able to explain the structure of the universe. The observations of large scale structure in the universe shows a web like structure of strings, filaments and clusters. From n-particle simulations it can be

shown that these structure cannot be formed by baryonic matter on their own. It requires mechanism which allows baryonic matter to fall into pre-defined structures in order to form galaxies in the right mass range and to explain the large scale structures one can observe today. This mechanism can be simulated through cold dark matter which froze out much earlier after the Big Bang than ordinary baryonic matter. It then had enough time to form structures baryonic matter can fall into by gravitation [UR16]. One candidate which would have the right abundance to fit these requirements is the so called WIMP which is introduced in the next section.

1.1.2 *Dark Matter Candidates and Detection Methods*

In order to be a suitable particle dark matter candidate the particle has to be neutral (since it is dark), it needs to have a small cross-section, it has to be cold, it has to match the estimated relic density and needs to be consistent with Big Bang nucleosynthesis. Additionally it has to be consistent with so far made observations [Ber10]. One candidate which fulfills all these requirements is the so-called WIMP. The terminus WIMP is a placeholder for a variaty of different candidates. They have a mass range of 10 GeV up to the TeV scale [Fen10] and an interaction cross-section in the order of the electro-weak scale [UR16]. Their models predict that they were produced during a thermal freeze-out after the Big Bang leaving naturally today's observed relic density of DM. This context is also often referred to the so-called WIMP miracle, which means that a variety of different WIMP candidates such as supersymetric particles like neutralinos are having the correct properties to reproduce the today's relic density of DM [Zac07, Fen10]. Also a multiplicity of other particles like axions or sterile neutrions are good DM candidates but will not be further discussed here and the reader is referred to [Fen10].

The detection of DM particles like WIMPs can be achieved by either one of the following three methods [UR16]:

1. Indirect detection through DM annihilation and the observation of mono-energetic γ-rays or neutrinos ($\chi\,\chi \rightarrow \mathrm{SM}\,\mathrm{SM}$[3]).
2. Indirectly as missing transverse energy in collidor experiments ($\mathrm{SM}\,\mathrm{SM} \rightarrow \chi\,\chi$).
3. Directly through scattering on a target nulcei ($\mathrm{SM}\,\chi \rightarrow \mathrm{SM}\,\chi$)

Experiments like DAMA/LIBRA, LUX or XENON1T are using the latter method to search for DM. From the WIMP freeze-out after the Big Bang, we can conclude that interactions between DM and standard model particles beyond the gravitational force must exist. This allows to measure the elastic scattering between WIMPs and standard model particles. This elastic scattering transfers some momentum and energy to the target nucleus, a so-called nuclear recoil (NR). The recoiling nucleus is underlying secondary scatterings with additional atoms of the used scintillator, producing scintillation light according to its properties. Assuming elastic scattering the energy transfer

[3] χ represents a DM particle and SM represents any standard model particle

on the recoiling target nuclei E_R can be described in the center-of-mass frame by

$$E_R = \frac{v^2 \cdot \mu^2}{m_N}(1 - \cos(\theta)) \quad \text{with} \quad \mu = \frac{m_N m_W}{m_N + m_W}, \tag{1.3}$$

in which v is the WIMP velocity relative to the target, θ the scattering angle in the center-of-mass frame, m_N and m_W the mass of the recoiling nucleus and WIMP respectively [Bau12]. Assuming a target mass of 132 GeV[4] and a WIMP mass on the lower end of the mass range of 20 GeV this formula yields a mean recoil energy of $\langle E_R \rangle = 2.6\,\text{keV}$ for a mean WIMP velocity of $\langle v \rangle = 220\,\text{km/s} = 0.75 \cdot 10^{-3}\,\text{c}$ relative to the target [Bau12]. In general the NR energy spectrum is given by a falling exponential distribution with a mean value of a few keV for most models [A+17c].

The differential scatter rate $\frac{dR}{dE_R}$ of a detector is simply given by the number of target atoms N_N, the WIMP particle flux ϕ_W and the differential cross-section $\frac{d\sigma_{WN}}{dE_R}$. Hence the scatter rate can be described by

$$\frac{dR}{dE_R} = N_N \underbrace{\frac{\rho_0}{m_W} \int_{v_{min}}^{v_{esc}} dv f(v)}_{\phi_W} \frac{d\sigma_{WN}}{dE_R} \tag{1.4}$$

where ρ_0 represents the local DM density and v_{min} and v_{esc} are the minimal and maximal WIMP velocity which can be detected. The minimal velocity is thereby given by the detector threshold and the maximal velocity by the escape velocity [Bau12]. The differential reaction cross-section is given by

$$\frac{d\sigma_{WN}}{dE_R} = \frac{m_N}{2\mu^2 v^2}\left[\sigma_{SI} F_{SI}^2(E_R) + \sigma_{SD} F_{SD}^2(E_R)\right] \tag{1.5}$$

in which F_i are the nuclear form factors and σ_i the cross-sections of the spin-dependent (i = SD) and spin-independent (i = SI) interaction channel respectively. The cross-sections can then be expressed by

$$\sigma_{SI} = \frac{4\mu^2}{\pi}\left[Z f_p + (A - Z) f_n\right]^2 \tag{1.6}$$

and

$$\sigma_{SD} = \frac{32\mu^2}{\pi} G_f^2 \frac{j+1}{j}\left[a_p \langle S_p \rangle + a_n \langle S_n \rangle\right] \tag{1.7}$$

where a_j and f_j are the WIMP coupling constants for protons (j = p) and neutrons (j = n) for spin-dependent and spin-independent case respectively. $\langle S_p \rangle$ and $\langle S_n \rangle$ are the expectation values of the proton and neutron spin operators. They are important for unpaired protons or neutrons of even-odd or odd-even nuclei. Further the spin-independent corss-section is scaling quadratic with the atomic number of the target nuclei [Bau12].

For these two reasons xenon is an interesting target material, since it has a high

[4] A mass of 132 GeV corresponds rougly to the mass of a xenon atom.

molecular weight and a nearly 50/50 abundance of even-even and even-odd xenon atoms. This allows to probe both the spin-independent and spin-dependent (for neutrons only) interaction channel. Other important parameters of xenon for its usage as a scintilltor are discussed in the following section.

1.2 LIQUID NOBLE GAS PROPERTIES AND THE DUAL-PHASE TIME PROJECTION DETECTOR PRINCIPLE

Through the last five decades liquid noble gas detectors have been developed from an initial idea by Luis W. Alvarez et al. in 1968 [A+71, AD10] to a well-established detector type for rare event experiments such as neutrinoless double β-decay ($0\nu\beta\beta$), the standard model forbidden $\mu \rightarrow e\gamma$ decay and direct search for Dark Matter. Beside their success in rare event detection experiments they have also been used in other branches of particle physics and astrophysics as well as in medical imaging [AD10].

In the following there is an introduction to the fundamental mechanics of liquid noble gases for their usage as a detector medium as well as the underlying detector concepts. The first Subsection 1.2.1 deals with noble gas properties, emphasizing on liquid xenon due to its usage in the MainzTPC and XENON1T. Subsection 1.2.2 discusses the principle of a dual-phase time projection chamber.

1.2.1 *Liquid noble gas properties*

liquid argon and liquid xenon are suited for rare event experiments due to their unique feature of producing both charge carriers and scintillation photons through the interaction with radiation [CA13, AD10]. If measured together this feature allows an exact determination of the properties and the energy of the incident particle. Further, the production of charge carriers can be used to receive a spatial resolution of the interaction position by applying a homogeneous drift field (see therefore Section 1.2.2).

The scintillation photons of LAr or LXe have their origin in the de-excitation of excited diatomic molecules (so-called excimers) which can be formed through either the direct excitation of atoms

$$\begin{aligned} R^* + R + R &\rightarrow R_2^* + R \\ R_2^* &\rightarrow 2\,R + h\nu\,, \end{aligned} \tag{1.8}$$

or by the recombination of ionization electrons with noble gas ions

$$\begin{aligned} R^+ + R &\rightarrow R_2^+ \\ R_2^+ + e^- &\rightarrow R^{**} + R \\ R^{**} &\rightarrow R^* + \text{heat} \\ R^* + R + R &\rightarrow R_2^* + R \\ R_2^* &\rightarrow 2\,R + h\nu \end{aligned} \tag{1.9}$$

where R stands for either Xe or Ar[CA13, AD10]. The wavelengths of the emitted

Table 1.1 – *Important parameters for liquid noble gas scintillators. The energy W_{ph} which is required to produce one scintillation photon in liquid noble gases is LET dependent and is here given for 1 MeV impinging α- and β-particles as well as the minimal amount of energy W(min) which is theoretically required to produce one scintillation photon. Further given is the average energy (W-value) which is required to create one electron-ion pair. [AD10, Ber10, CA13, Sch12].*

	Argon	Xenon
Atomic number	18	54
Molecular weight [g/mol]	40.0	131.3
Density at boiling point [g/cm^3]	1.40	2.94
Boiling point at 1 atm [K]	87.3	165.0
Costs (relative)	$	$$$$
Scintillation Wavelength [nm]	128	178
Energy for one scintillation photon [eV]		
W_{ph}(min):	19,5	13.8
W_{ph}(1 MeV α):	27.1	17.9
W_{ph}(1 MeV β):	24.4	21.6
Energy for one electron-ion pair [eV]		
W-value in Gas:	26.4	22.0
W-value in Liquid:	23.6	15.6

scintillation photons are part of the vacuum ultraviolet (VUV) region of the electromagnetic spectrum and have their origin in the transitions from the excited triplet ($^3\Sigma_u^+$) or singlet state ($^1\Sigma_u^+$) to the ground state ($^1\Sigma_g^+$) of the excimer [CA13]. It peaks for liquid xenon around 178 nm [AD10] and is stated together with other important properties of LAr and LXe in Table 1.1.

Measuring the shape of these a scintillation process shows that the two possible de-excitation transitions from the triplet and singlet state of the excimers have different decay times [CA13, AD10]. By applying a high electric drift field in the order of 10 kV/cm it can be shown, that the production mechanisms of the excimers through the recombination and direct excitation channel are not equally distributed [CA13]. Figure 1.4 shows for impinging fast electrons the recombination (R) and excitation (Ex) channels branching ratio together with the life-times of the singlet ($^1\Sigma_u^+$) and triplet ($^3\Sigma_u^+$) excimer states for fast electrons and α-particles. For α-particles the recombination and excitation branch in Figur 1.4 are joint together. This can be explained by the higher linear energy transfer (LET) value for alpha particles compared to electrons with the same energy. In this case recombination occurs more intense and faster along the particle track and hence, even with high electric fields, the scintillation mechanism becomes indistinguishable between excitation and recombination [CA13].

Comparing the decay times for electrons and α-particles in Figure 1.4 shows that the joint effective decay time for α-particles is shorter than for electrons. This holds true also for the nuclear recoil on Xe atoms and hence a detailed shape analysis of the scintillation process can be used for discrimination and distinction between NR induced from neutrons or WIMPs and ER from electrons or γ-rays scatter in a detector. For nuclear and electronic recoil with a recoil energy of 20 keV, effective scintillation

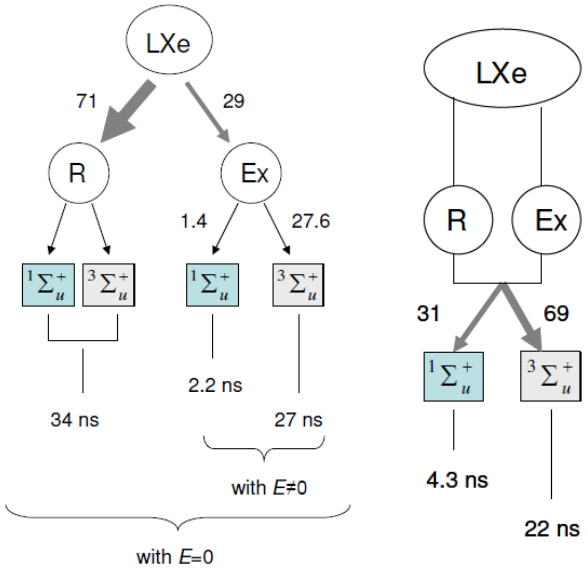

Figure 1.4 – *Decay times of the singlet and triplet states from the recombination (R) and excitation (Ex) channels of Xenon excimers. On left hand side the decay times for fast electrons with an energy of 0.5 to 1 MeV and on the right hand side for α-particles with an energy of 5 MeV are presented. The thickness as well as the numbers next to the arrows indicate the branching ratios. The curly brackets under the diagram for fast electrons indicate wich component can be measured with* $(E \neq 0)$ *and without an high electrical field* $(E = 0)$ *[CA13].*

life-times of 33 ns and 19 ns were measured. So far it is not well understood why higher LET values lead to a supression of the slow decay component [CA13][5].

The scintillation yield of liquid xenon with 40 to 50 photons/keV for 1 MeV electrons is comparable to the scintillation yield of NaI scintillators [CA13, AD10]. However, for γ-ray and electron energies in a range between 1 and 10 keV the scintillation yield mechanism is not fully understood yet in which range also the released energy of the ^{37}Ar decay lies [CA13, S$^+$11]. The scintillation yields for γ-rays and electrons is shown together in Figure 1.5. The plot shows that the scintillation yield decreases for low electron and γ-ray energies, even though their LET value increases. This comes from the fact, that for low energies more electrons escape from the interaction side before they can recombine with noble gas ions [CA13]. Further it can be seen from the plot, that the scintillation yield for a 2.5 keV γ-ray and electron differ by roughly 10 photons/keV. This is due to the fact, that the absorption of γ-rays is rather inducing an emission of a bunch of electrons with different energies, than the emission of a single monoenergetic-electron [CA13]. This difference between electrons and γ-rays must be taken into account when performing a calibration of liquid xenon detectors in the low energy regime using for example ^{37}Ar. The dip in the scintillation yield between 20 keV and 50 keV comes from a xenon K-edge resonance producing low energy Auger electrons [S$^+$11].

Since the scintillation in liquid argon and xenon is produced either through direct

[5] Also one of the main design goals for the MainzTPC was it to improve the understanding of the decay times and shapes of the scintillation in LXe for NR and ER. This can be further read in [Bes17].

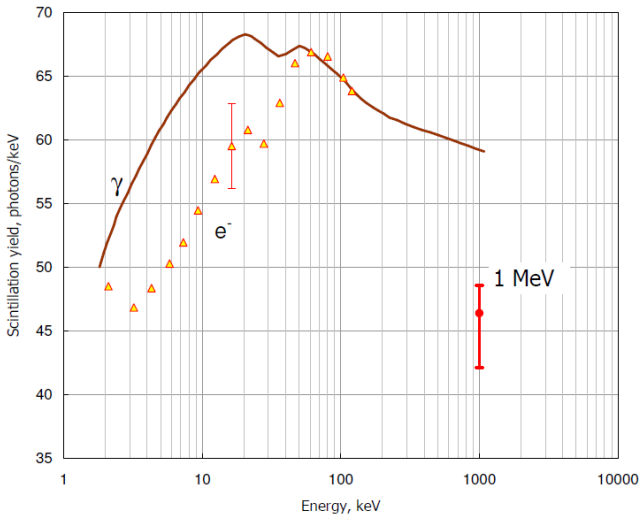

Figure 1.5 – *The scintillation yield of LXe as a function of energy for γ-rays (solid line) and electrons from a Compton scattering set-up (triangles) [CA13]. The drawn line for the γ-rays is based on a modulation with NEST for different data sets. The data sets combined with the model fit are shown in Figure 5.2 in the Appendix A. on page 114. The red circle represents the light yield for a 1 MeV electron.*

excitation or electron-ion recombination, the scintillation yield changes when an electric field is applied to the liquid scintillator. The applied field will inhibit the emission of the scintillation light coming from recombination due to the drift motion of the charge carriers and hence will gradually decrease the light yield with increasing drift field strength. If a detector is used which is sensitive for light and charge carriers, it can be further shown, that the relationship between charge and light yield is strongly anti-correlated. This anti-correlation depends on the LET region and is only perfectly anti-correlated where the scintillation yield is at its maximum [CA13, AD10]. This anti-correlated fashion is shown in Figure 1.6 for different electric fields and particle interactions, like electronic recoil, nuclear recoil and α-particles. Further it can be seen in Figure 1.6, that the light/charge ratio changes not much with the drift field strength for high LET interactions such as collisions with α-particles and nuclear recoil. As already mentioned in the discussion about the scintillation shape this behavior can be explained by the denser inoization tracks of such an interaction and therefore faster recombination of the electron-ion pairs. A more quantitative prediction for the charge and light yield of γ-rays and electrons based on the Noble Element Simulation Technique (NEST) [S$^+$11, S$^+$13] can be found in the Appendix A. in Figure 5.3 (on page 114).

Besides changing the scintillation yield, an electric drift field allows to use the ordered motion of the generated electron-ion pairs as an additional read-out channel of the scintillator. Since the mobility of heavy ions is five orders of magnitudes lower than for electrons only electrons are suitable to be read out by a charge sensitive detector [CA13, AD10]. The drift velocities for electrons in liquid noble gases, as function of the drift field, and in the gaseous phase, as a function of the reduced field, are shown in Figure 1.7. One advantage for drifting electrons in a charge sensitive noble

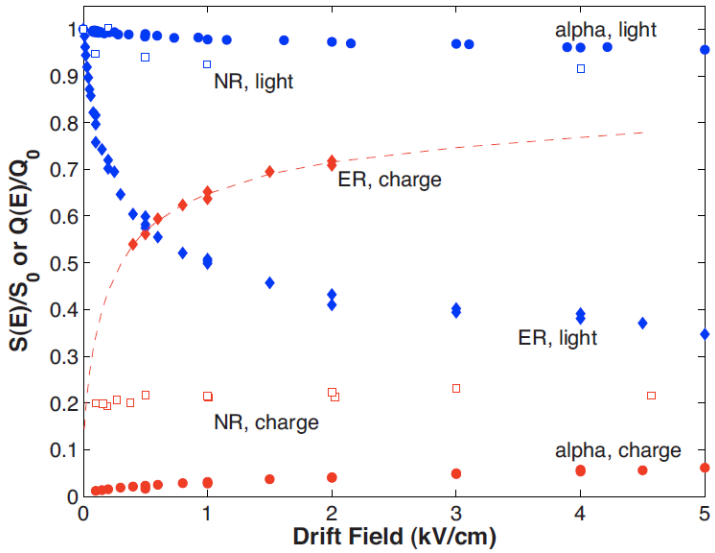

Figure 1.6 – *Relative scintillation (light) and charge yields (charge) for 122 keV ER, 56.5 keV NR and 5.5 MeV α-particles as a function of the electric drift field in LXe. The charge and scintillation yields are normalized to their yields for a zero drift field [AD10].*

gas detector is that further excitation or ionization of the noble gas atoms can occur, if the electrons are accelerated to sufficient high kinetic energies between two collisions. This can be achieved in gaseous argon or xenon where an excitation of further atoms leads to a secondary scintillation process which is proportional to the initial number of electrons. This effect is called electroluminescence. If the electrons are accelerated to even higher energies, exceeding the ionization potential of the noble atoms an avalanche produced by a cascade of secondary electrons allowing very high amplifications in gas detectors. However, due to discharges caused by secondary avalanches through a photoelectric feedback from VUV photons and impurities this avalanche technique was never successfully established in dual-phase liquid noble gas detectors like the XENON1T experiment [AD10]. Instead dual-phase liquid noble gas TPCs like the MainzTPC or XENON1T are both using the electroluminescence effect for an amplification of the charge signal. The number of emitted electroluminescence photons N_γ which are created by one electron are shown in Figure 1.8 and are given by

$$N_\gamma = \alpha \cdot N_e \left(\frac{E}{p} - \beta \right) p \cdot d \,, \tag{1.10}$$

where N_e represents the number of drifted electrons, d the drift distance, E the electric field strength, p the Xenon gas pressure, β the threshold of the reduced field and α the amplification factor [CA13, AD10]. Since the electroluminescence is directly proportional to the number of initially created charge carriers it is important to extract as much electrons from the liquid into the gas phase as possible. This can be achieved by applying an extraction field between the liquid-gas interface to help the electrons to overcome the potential barrier of the liquid gas interface. All electrons which are

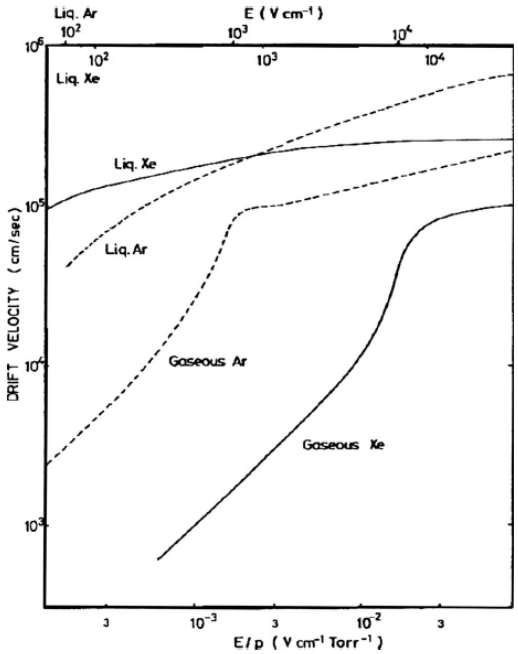

Figure 1.7 – *Drift velocities of electrons in liquid and gaseous xenon and argon. The drift velocity is represented as a function of the reduced field (field strength divided by the pressure) for the gaseous phase and as function of the electric field for the liquid phase [AD10].*

not able to overcome this barrier by the first attempt are scattered back into the liquid. After several collisions inside the liquid those leftover electrons drift again towards the liquid-gas interface, where the same procedure repeats. This leads to a transition distribution comparable to the thermal evaporation from a Maxwell-Boltzmann distribution tail. Such an effect can by avoided by a sufficient high electric extraction field [CA13]. The extraction efficiency as function of the extraction field is shown on the right hand side in Figure 1.8.

All the properties of liquid xenon which were presented are important for its usage as detector medium. One typical example for a detector which exploits these is a so-called dual-phase time projection chamber which is going to be introduced in the following section.

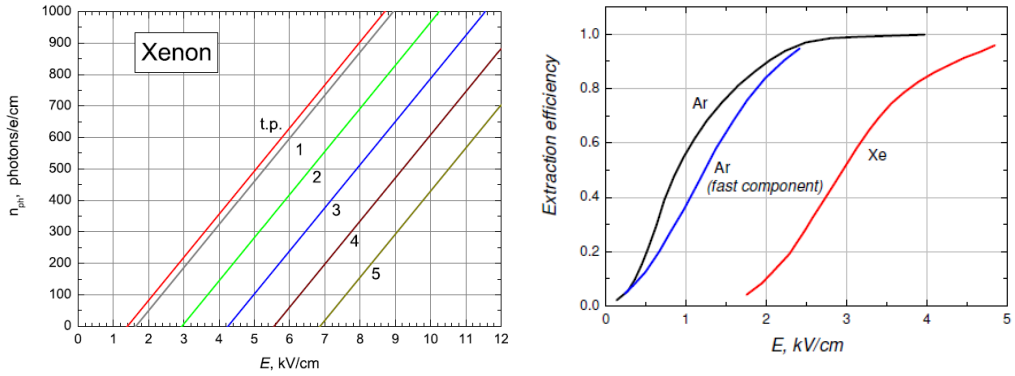

Figure 1.8 – *The number of electronluminescence photons in Xenon and the Extraction efficiency of electrons in Argon and Xenon as a function of the extraction field. The plot on the left hand side shows the number of electroluminescence photons as a function of the electrical extraction field for a satured gas at different pressures. The pressure in bar is indicated by the numbers next to the colored lines (t.p. stands for the triple point $p = 0.8175\,bar$). The picture on the right hand side shows the extraction efficiencies of electrons for a given electric extraction field in liquid Argon or Xenon based detectors [CA13].*

1.2.2 *Dual-Phase Time Projection Chamber*

Based on the properties of liquid xenon, as a detector using LXe has either to be sensitive to charge carriers, scintillation photons or both. One detector type for noble gases which is sensitive to both types of signal channels is a so-called dual-phase time projection chamber. The TPC principle was invented by David Nygren back in 1970 [Nyg76] and firstly proposed for LAr by Rubba in 1977 [AD10]. It exploits the correlation between the drift time of free charge carriers in a certain medium and the applied drift field strength in order to get a spatial resolution of the interaction side. However, compared to the first build liquid noble gas (single-phase) TPCs, current designes for direct DM search and other rare event experiments are operating in the dual-phase (liquid and gas) mode. This allows an enhanced read out of the charge signal which is producd by the impinging particle. One further advantage is that both signal channels (charge and scintillation) can be read out through only one type of sensor [AD10, CA13]. In the following the concept of a dual-phase time projection chamber, including the basic detection medium properties of liquid xenon, are explained.

The most common configuration of a dual-phase time projection chamber as used in the XENON1T [A$^+$17c] or LUX [A$^+$13] experiment is sketched on the left hand side of Figure 1.9. It consists of two separated photomultiplier tube arrays at the ceiling and at the floor of a cylindrical vessel which contains the liquid and gaseous phase of xenon. In between of those two arrays are several meshes which are used to apply an homogeneous drift field in the liquid phase between cathode and gate mesh and an extraction field between the gate and anode mesh. The space between gate and node mesh is also containing the liquid-gas interface. Depending on the polarities of the voltages which are applied to the meshes and PMTs additional screening meshes

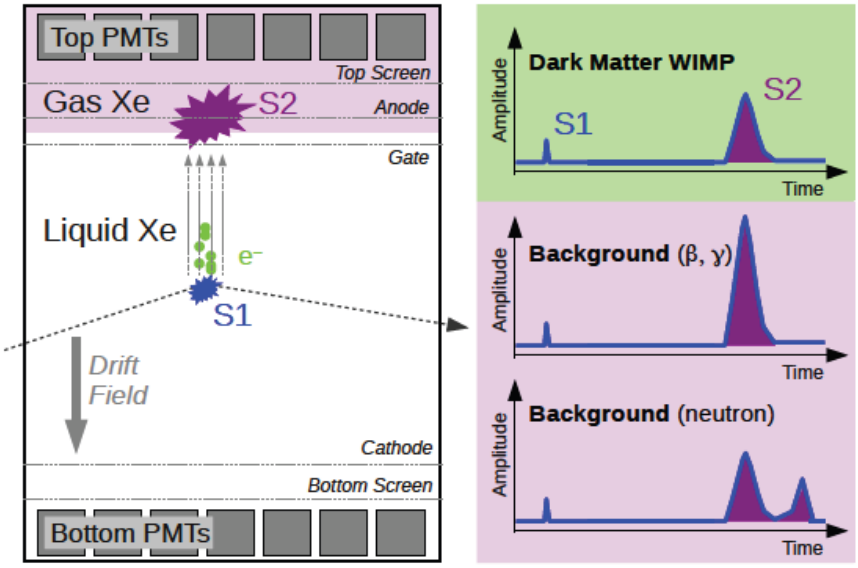

Figure 1.9 – *Schematic of a LXe dual-phase time projection chamber. The left hand side of the schematic shows the working principle of the TPC while the right hand side sketches the shape of the first (S_1) (colored in blue) and second scintillation signal (S_2) (colored in violet) for impinging WIMP or background particles. [A+17c]*

have to be put in front of the PMT arrays to ensure a proper operation of the PMTs [A+17c].

When a particle enters the liquid target of the detector and interacts with the LXe it produces VUV photons, electrons and heat through the excitation, ionization and elastic collisions of xenon atoms. The number of photons and electrons which are initially produced depends on the impinging particle type; and its energy. While neutrons or WIMPs are scattering off the xenon nuclei and hence produce NR with more dense ionization tracks due to multiple elastic scatterings of the recoiling xenon nuclei with other xenon atoms; electrons or γ-rays are scattered by the atomic electrons of xenon producing an ER with less dense ionization tracks. Because of these different densities the recombination of electron ion-pairs occurs varyingly strong, leading to a discriminative number of created charge carriers (free electrons) and scintillation photons between these two different interaction types. While the emitted photons are directly detected by the VUV sensitive PMTs of the TPC giving a primary scintillation signal called S_1, the electrons are drifted from the interaction side towards the liquid gas interface of the detector by the applied electric field, reaching the extraction field. The purpose of this extraction field is twofold: firstly it extracts the electrons from the liquid into the gas phase. Secondly, they are accelerated and gain enough energy to excite further Xenon atoms leading to an enhanced second scintillation signal based on the electroluminescence effect. This second scintillation signal is also recorded by the PMT arrays and is called S_2 [AD10, A+17c].

Recording both the S_1 and S_2 signal of an interaction provides the key features of a liquid noble gas TPC. First of all it allows a three-dimensional position reconstruction

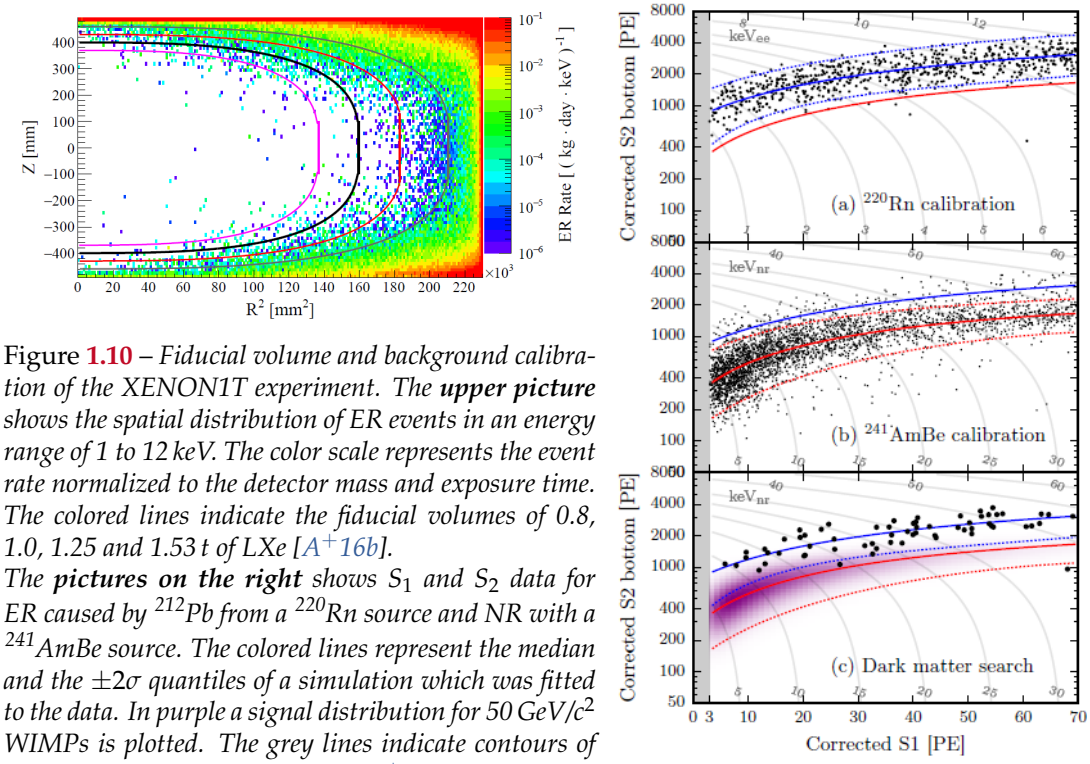

Figure 1.10 – *Fiducial volume and background calibration of the XENON1T experiment. The* ***upper picture*** *shows the spatial distribution of ER events in an energy range of 1 to 12 keV. The color scale represents the event rate normalized to the detector mass and exposure time. The colored lines indicate the fiducial volumes of 0.8, 1.0, 1.25 and 1.53 t of LXe [A⁺16b].*
The ***pictures on the right*** *shows S_1 and S_2 data for ER caused by ^{212}Pb from a ^{220}Rn source and NR with a ^{241}AmBe source. The colored lines represent the median and the $\pm 2\sigma$ quantiles of a simulation which was fitted to the data. In purple a signal distribution for 50 GeV/c^2 WIMPs is plotted. The grey lines indicate contours of constant combined energy scales [A⁺17d].*

of the interaction side. This can be achieved by using the S_2 signal for a reconstruction in a horizontel plane prallel to the PMT arrays and through the correlation between the time difference of $S_2 - S_1$ and the drift velocity in vertical direction. The ratio of S_1/S_2 can further be used for particle discrimination. For NR an enhanced electron-ion recombination occurs due to a more dense particle track structure. Therefore less charge carriers are drifted towards the liquid-gas interface leading to a bigger S_1/S_2-ratio. Thus the ratio of S_1/S_2 provides an important tool for the background discrimination between NR and ER in rare event experiments. In addition the difference of the NR cross-section for WIMPs and neutrons allows a discrimination of neutron scatter, based on multi-scatter S_2 signals in large scale LXe detectors. This is important since those signals are comparable in other regards like signal shape and size. The S_1 and S_2 signals of different background particles as well as for WIMPs are sketched in Figure 1.9 on the right. Further S_1 and S_2 data points of the XENON1T calibration together with some simulated for 50 GeV/c^2 WIMPs are plotted on the right hand side of Figure 1.10 [AD10, A⁺17c].

Also the energy resolution of the detector impoves if the S_1 and S_2 signal are readout simultaneously [A⁺07, S⁺15, CA13]. The energy of an impinging particle is measured in a dual-phase TPC in terms of the PMT signal charge and is hence given by the initial number of charge carriers and scintillation photons produced during the interaction with the LXe. While the total number of produced quanta (photons and electrons) is constant for a given particle energy, the ratio between the VUV photons and electrons can fluctuate due to the statistical nature of the electron-ion recombina-

tion. This leads to strong variations of the S_1 and S_2 signals which worsen the energy resolution of the detector if they are read out separately. Exploiting the fact that the scintillation and charge yield are anti-correlated for a given electric field allows to use a combined energy scale instead[6]. This combined energy scale is proportional to the total amount of produced quanta and hence is not affected by such fluctuations. It therefore improves the overall energy resolution of the detector [CA13, A+07, S+15]. The different energy resolutions for S_1- and S_2-only as well as for the combined energy scale are shown together in Figure **1.11** for the 662 keV full energy peak of ^{137}Cs. The measurement was taken at a drift field of 1 kV/cm leading to an energy resolution of (10.3 ± 0.4) %, (4.8 ± 0.1) % and (1.7 ± 0.1) % for the S_1-, S_2-only measurement and combined energy scale respectively [A+07]. The angle θ between the x-axis and the major axis of the ellipse in the S_2 versus S_1 scatter plot of Figure **1.11** is the so-called anti-correlation angle. It can be found through a two dimensional Gaussian fit of the 662 keV ellipse leading to an angle of 24.8 °, or in a different representation to an anti-correlation coefficient between charge and light of $\rho_{sq} = -0.87$ for the presented data [A+07]. The combined energy scale E_c

$$E_c = E'_c \cdot \frac{E_0}{E'_0} = \frac{E_{S1}\sin(\theta) + E_{S2}\cos(\theta)}{\sin(\theta) + \cos(\theta)} \tag{1.11}$$

can then be derived as a projection E'_c of the light E_{S1} and charge E_{S2} energies onto an axis perpendicular to the major axis of S_1 S_2 ellipse which is re-normalized to the real peak energy E_0 [A+07]. However, more often the term

$$E_c = W \cdot \left(\frac{S_1}{g_1} + \frac{S_1}{g_2}\right) \tag{1.12}$$

is used for practical reasons, where $W = 13.7$ eV is the average energy required to produce one electron-ion pair based on a weighted average from NEST, and g_1 and g_2 the primary and secondary scintillation gains [A+17c].

In addition to the ability to discriminate between electronic and nuclear recoil, one other key feature of liquid scintillator based detectors compared to experiments which use scintillation crystals like NaI is the capability to enlarge the detector volume to large and homogeneous scales more easily. Using further the natural self-shielding of LXe, due to its high atomic number and density, together with the feature of a three-dimensional position reconstruction in a dual-phase TPC, a so-called fiducialization of the detector volume becomes possible [A+17c]. This allows to distinguish background events from possible WIMP interaction. Due to their low cross-section WIMPs can also produce nuclear recoil in the center of the active volume unlike background particles such as electrons, γ-rays and neutrons which are more likely absorbed in the very first centimeters of the cylindrical LXe volume. For the XENON1T detector this fidudulization of the detector volume is shown in the upper picture of Figure **1.10**. In addition a large scale detector improves the expected event rate since the rate scales linearly by the number of target. However, this fiducialization does not help against

[6] See also Figure **1.6** in Section 1.2.1 for the anti-correlation between charge carriers and scintillation photons.

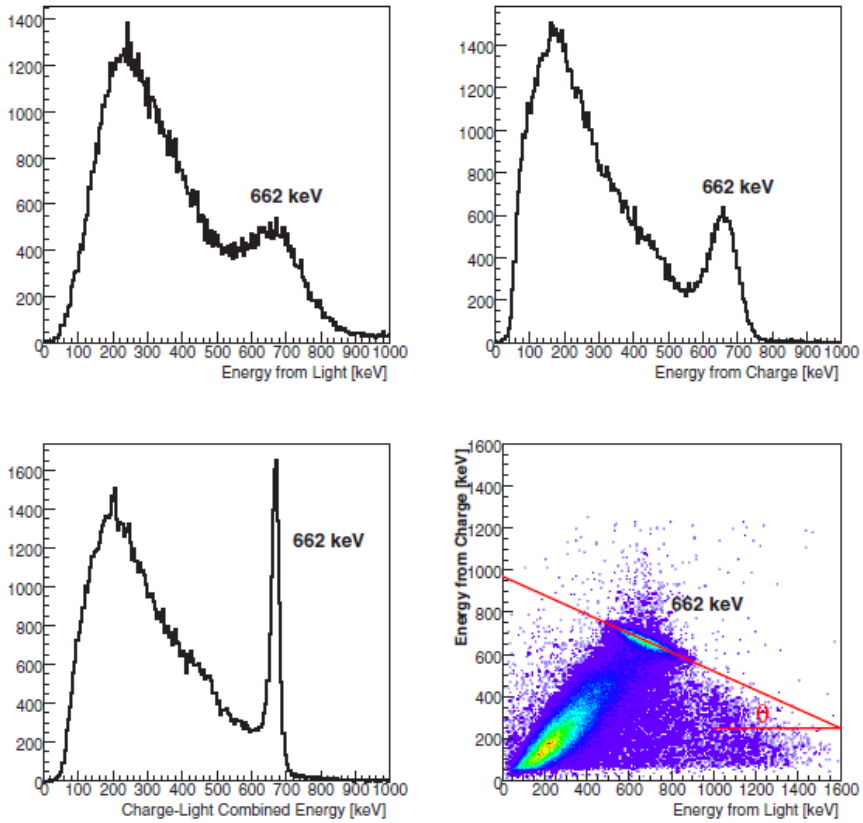

Figure 1.11 – *Combined energy scale of a single-phase TPC for the 662 keV full energy peak of ^{137}Cs at a drift field of 1 kV/cm. The top row shows the energy spectrum of ^{137}Cs measured for the scintillation and charge signal channel. While the bottom row shows the resulting combined charge-light energy scale and the charge versus light scatter plot for ^{137}Cs [A$^+$07].*

detector intrinsic background coming from impurities of the used detector materials and the liquid xenon itself [A$^+$17c].

The problem with impurities in large-scale LXe detectors can be divided into two sub-categories. In the first category are electronegative impurities like water and oxygen which are constantly outgassed from the used detector materials. They worsen the charge and light yield of the detector by absorbing the generated electrons and photons, or producing false single- and multi-electron signals by their ionization through absorbed VUV photons. The second sub-category are detector intrinsic radioactive impurities such as ^{nat}Kr which contribute to the overall background of the detector [A$^+$17c].

In order to improve the level of contamination of electronegative impurities in experiments like the MainzTPC and XENON1T the xenon is constantly recirculated through a purification system [Hil14, A$^+$17c]. Both experiments are using a so-called hot getter which binds the electronegative impurities by chemical bindings to a large zirconium surface in order to free the xenon from them. Noble gases are unaffected by this process.

Further, in XENON1T a cryogenic distillation is in use which has mainly the purpose to filter ^{nat}Kr from the Xenon gas. It exploits the different vapor pressure for a given temperature of two gases in order to separate them from each other [A$^+$17c]. These two purification methods should be kept in mind during the search and development of new internal calibration gases like those which are going to be introduced in the next section.

1.3 GASEOUS CALIBRATION SOURCES AND THE ISOTOPE ^{37}AR

A proper detector calibration is one of the keys to study new particles and unknown physics. Like shown in Section 1.2.1 the response of LXe to an impinging particle depends on the particle type and its energy which is also reflected in its LET-value. Further each dual-phase TPC has its own unique signal signature in terms of charge and light yield which needs to be understood and parameterized. Therefore it is indispensable to calibrate the detector with a source whose energy and properties are well known for comparison to the unknown particle.

Unfortunately a uniform calibration of the inner most detector volume, becomes very challenging due to the excellent self shielding property of LXe for large scale LXe TPCs. Sources emitting from the outside into the detector are absorbed within the very first centimeters. This holds especially true for low energetic calibration sources. Therefore gaseous isotopes which allow an *in situ* calibration are beneficial for an uniform detector calibration and allow to understand the detector performance for even low energetic events. During the calibration of XENON1T a ^{83m}Kr and ^{220}Rn calibration gas were sucessfully introduced into the active volume of the detector for this purpose [A$^+$17c].

In the following Section 1.3.1 there is a short introduction to the most relevant calibration methods for a LXe TPC, including the calibration of the electronic and nuclear recoil responds. Afterwards ER calibration of LXe TPC through gaseous isotopes and their relevant properties are discussed based on four already used isotopes in XENON100, XENON1T and LUX. In the end of Subsection 1.3.1, $^{37}_{18}Ar_{19}$ is motivated in this context. Subsequent Section 1.3.2 deals with ^{37}Ar itself; discussing its decay mode, follow-up processes and reviewing its possible ways of synthesizing.

1.3.1 *Calibration Techniques and Gaseous Calibration Methods*

Dual-phase liquid xenon TPCs are able to discriminate between nuclear and electronic recoils, therefore two different calibration campaigns have to be conducted. Nuclear recoils of xenon atoms can be induced through collisions of impinging neutrons and hence the detector can be calibrated with mono-energetic and continuous neutron sources. In the case of the XENON1T detector a Deuterium-Deuterium generator with neutron energies of 2.2 MeV and 2.7 MeV and AmBe as continuous α-neutron source are used for this purpose [A$^+$17c]. Those sources are not suited for an *in situ* calibration due to their properties like size or half-life and therefore are placed next to the

detector. This is the only option since any so far discovered isotope which is decaying through a spontaneous neutron emission has a decay time of less than one second [JRC12]. Hence, synthesizing a neutron emitting calibration gas is not possible.

For electronic recoils, a broader range of different decay modes, like γ-deexcitation, the β-decay, internal conversion, or follow-up processes like Auger electrons or X-rays can be used as a calibration source. Whereof also many isotopes in a gaseous state of matter exist which decay or deexcite through one of those processes. Depending on the calibration purpose, calibration sources with either mono-energetic transitions or continuous energy spectra are required. While mono-energetic sources are used for an absolute energy calibration as well as a position dependent calibration of the detectors charge and scintillation yield; continuous source like β-emitter are more appropriated to set-up ER selection/discrimination curves[7]. Two of these selection curves were already shown in Figure **1.10** on page 18 for nuclear and electronic recoils.

Using an *in situ* source like ^{37}Ar adds further requirements to the properties of the used isotope, beside an appropriated energy scale and spectrum, Like a variety of requirements concerning their decay time, reactivity and state of matter of the daughter nuclei. These key features are discussed in the following in reference to four already used gaseous calibration isotopes in XENON100, XENON1T or LUX.

^{83m}Kr was used as a calibration source in a variety of experiments. Beside DELPHI [C$^+$95], STAR [E$^+$01] and KATRIN [Ang04] it was also succesfully used in liquid noble gas dual-phase detectors like XENON1T [A$^+$17c] and LUX [A$^+$17a]. ^{83m}Kr evolves from ^{83}Rb which decays with an half-life of 86.2 d [A$^+$17a] via electron capture into one of many exciteted states of ^{83}Kr. All of those excited states have a life time in the picoseconds time scale and leads to the isomeric state ^{83m}Kr [M$^+$10]. Like shown in the decay scheme on the left hand side of Figure **1.12** the decay of ^{83m}Kr is subdivided through an intermediate state. The two transitions have a transition energy of 32.1 keV and 9.4 keV respecitively. The energy is mainly emitted by a mixture of internal conversion (IC) photons, Auger electrons and x-rays [M$^+$10]. The effective decay time of ^{83m}Kr is given by its first transition with an half-life of 1.83 h [M$^+$10]. However the half-life of the second transitions (154 ns) is long enough to be exploited in a LXe TPC for a unique two-pulse structure discrimination like shown on the right hand side of Figure **1.12**.

Although the transition energy of 9.4 keV lays within the energy range of interest for the WIMP direct detection, for the combined energy scale only its summed signal of 41.5 keV is useable. This is stemming from the fact, that the two S_2 signals from the individual transitions cannot be separated properly due to the short decay time of the intermediate state. Apart from its use as data point for the absolute energy calibration of the ER responds, ^{83m}Kr is also used in XENON1T and LUX for monitoring the overall light collection and extraction efficiency of the detector, as shown in Figure **1.15** [A$^+$17c, A$^+$16a].

Since the decay time of ^{83m}Kr is short, it can stay inside the detector medium without the need of high cool down times. In the case of the XENON1T all remnants of the ^{83m}Kr or ^{83}Kr are filtered out by the cryogenic distillation together with the ^{nat}Kr [A$^+$17c].

[7] The same holds also true for the NR calibration

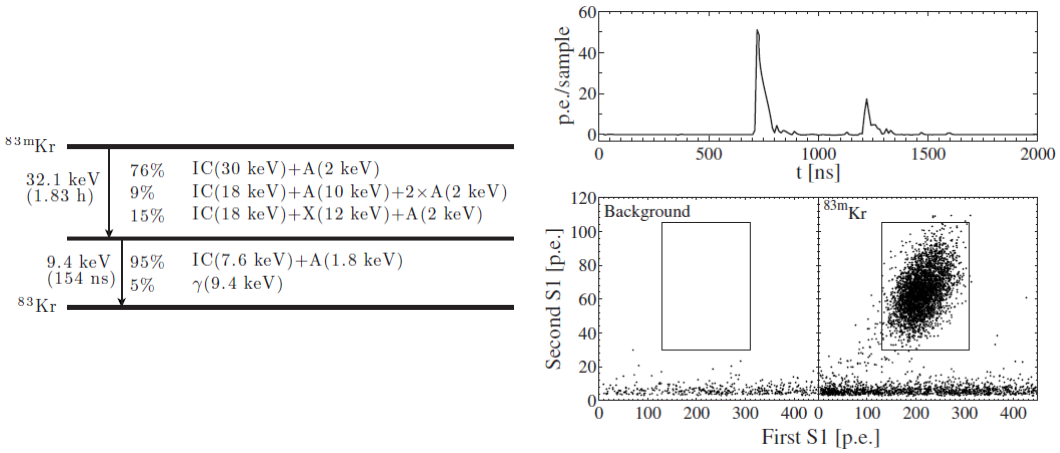

Figure 1.12 – *Decay scheme of ^{83m}Kr and two-pulse structure discrimination of the ^{83m}Kr decay. The decay scheme of ^{83m}Kr on the left hand side shows the decay energies, decay times as well as the different decay modes of the two transitions. The upper picture of the right hand side shows a typical S_1 pulse distribution for the 32.1 keV and 9.4 keV transition measured with the "Xürich" TPC. The lower plot shows the unique two S_1 signal discrimination for ^{83m}Kr [M+10].*

^{220}Rn is a part of the Thorium chain and was studied in XENON100 [A+17b] as well as in XENON1T [A+17c]. In both experiments ^{228}Th was electrolytically deposited on a stainless steel disk which decays via

$$^{228}\text{Th} \xrightarrow[\tau_{1/2}=1.9\,\text{y}]{\alpha} {}^{224}\text{Ra} \xrightarrow[\tau_{1/2}=5.5\,\text{s}]{\alpha} {}^{220}\text{Rn}$$

into ^{220}Rn [JRC12]. Only a fraction of the ^{220}Rn emanates from the steel disk (40 ± 10 % in the case of XENON100 [A+17b]) and offers a variety of different α- and β-decays and can be used to study the convective motion of the liquid xenon as well as the detector response for electronic recoils in the low energy region. Latter is the main purpose for having ^{220}Rn as a calibration source in XENON1T. It decays along the Thorium decay chain towards the stable ^{208}Pb which is shown in Figure 1.13 on the left hand side.

While the convective motion of the LXe is studied by a delayed coincidence between the short lived isotopes ^{220}Rn and ^{216}Po, the decay of ^{212}Pb is used for the calibration of low energetic electronic recoils. In 12.3 % of the time it decays with a Q-value of 569.8 keV to its ground state leading to electronic recoils in the for XENON1T desired energy range of 2 to 30 keV [A+17b]. This results in a continuously distributed electronic recoil band in the S_2 versus S_1 parameter space which is shown in Figure 1.10 on page 18. Although it is well suited as a ER background calibration source, due to its continuous spectrum it can neither be used for an absolute energy calibration nor for a position dependent determination of the charge or light collection efficiency.

Studying the convective motion of LXe and hence the fluid dynamics of the detector helps to improve the experiment in two ways. First it probes for any eventual dead regions of the detector which are not affected by the recirculation [A+17b] and therefore

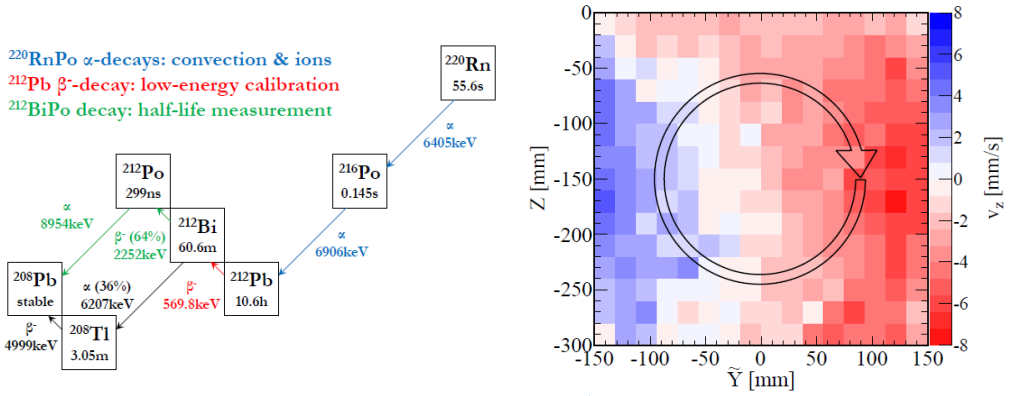

Figure 1.13 – *Decay scheme of the ^{220}Rn decay chain and the convectional motion of the liquid xenon in the XENON100 TPC. The picture on the left hand side shows a scheme of the ^{220}Rn decay chain. The decays highlighted in blue were used for the study of the fluid dynamics of the XENON100 detector, while the ^{212}Pb decay highlighted in red is used for the low energy ER calibration in XENON1T. The picture on the right hand side shows the velocity of the convectional motion in z-direction of the XENON100 TPC which is indicated by the colorbar. Plotted is the height of the TPC versus the parameter $\widetilde{Y}$ which represents a projection of the events onto a cross sectional plane through the TPC [A+17b].*

helps to improve the xenon purfication. Secondly the natrual ^{222}Rn is the main contributor for the ER background in the XENON1T experiment [A+17c]. Hence a new way of discrimination based on the decay chain or motion pattern would be of benefit [A+17b]. The convective motion of the LXe in the XENON100 detector is shown in Figure 1.13.

One drawback of using ^{220}Rn is, that the daughter nuclei stay inside the LXe due to their state of matter. Since the effective decay time of the decay chain is given by the half-life of ^{212}Pb with its 10.6 h this does not result in a long cool down of the detector [A+17b].

Tritiated methane **CH_3T**, was used as a calibration source in the LUX experiment [A+16a]. It emits the well studied β-spectrum of tritium which has an endpoint energy of 18.6 keV and an half-life of 12.3 years [A+17c]. The majority of the tritium decays (62.4 %) have a decay energy between 1 and 8 keV and hence are well suited as a calibration source for ER spectrum [A+16a]. Like ^{220}Rn it is used for the calibration of the ER selection curves, but it can neither be used for an absolute energy calibration nor for a position dependent probing of the charge and light collection efficiency. A scatter plot of the tritium spectrum measured by the LUX detector is presented in Figure 1.14.

Due to its long decay time tritium has to be actively removed from the LXe in order to avoid any background contribution of its remnants. Implementing tritium into a host molecule like tritiated methane has some advantages compared to the usage of pure T_2. One advantage of CH_3T is the larger molecule size and therefore smaller diffusion coefficient. Since large parts of liquid xenon TPCs are made out of plastics like polytetrafluoroethylene (PTFE) due to their high VUV reflectivitance, small molecules

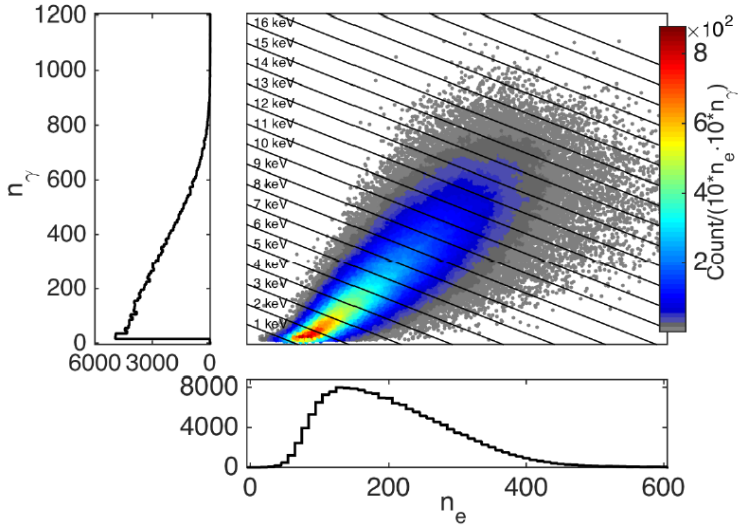

Figure **1.14** – *Tritium spectrum measured by the LUX TPC. The scatter plot shwos the number of scintillation photons versus the number of ionization electrons for the CH_3T source. [A+16a].*

like T_2 diffuse easily into those materials. Further CH_3T is not absorbed onto surfaces unlike T_2. Another advantage of methane as a host molecule comes from the fact, is its easy removability by standart noble gas purifiers like hot zirconium getters [A+16a].

Xenon itself can also be used as a calibration gas in a LXe TPC. To be more specific the two isomeric states ^{129m}Xe and ^{131m}Xe are used for this purpose. They have an half-life of 8.9 d and 11.8 d and deexcite via emission of γ-rays or through IC [N+07]. ^{129m}Xe has a transition energy of 236.2 keV while ^{131m}Xe has s slightly lower transition energy of 163.9 keV [A+17c]. Both isotopes have a comparable abundance of 26.4 % and 21.2 % [N+07]. They are produced by inelastic collisions with neutrons through

$$^{129}\mathrm{Xe}(n,n')^{129m}\mathrm{Xe} \tag{1.13}$$

and

$$^{131}\mathrm{Xe}(n,n')^{131m}\mathrm{Xe}\,; \tag{1.14}$$

either directly inside the active volume during the nuclear recoil calibration, or externally in a separate volume. Independent of the place of production a ^{241}AmBe source can be used for this purpose [A+17c, N+07]. The fast neutron cross-section is with 1.6 b for reaction (1.13) and 1.3 b for reaction (1.13), like their natural abundance comparable to each other [N+07]. Since both isotopes emit mono-energetic γ-rays or electrons they are used for the absolute energy calibration of the detector.

The draw back of this method is that neither ^{129m}Xe nor ^{131m}Xe can be separated from the remaining xenon and hence the detector has to cool down after usage or after the nuclear recoil calibration.

Looking at the so far used calibration sources makes clear that, one point which needs to be examined carefully when choosing a new calibration isotope concerns its remnants and their contribution to the detectors overall background and impurity.

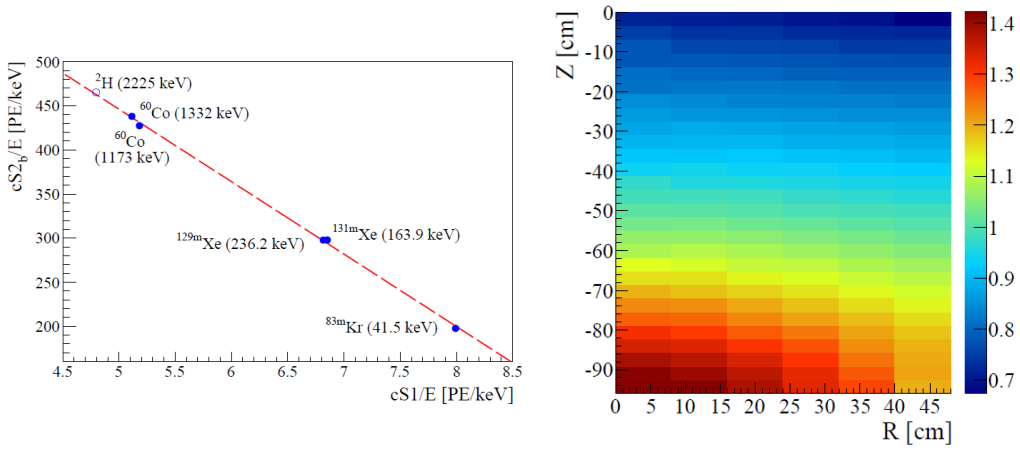

Figure 1.15 – *Energy calibration and azimuthally averaged light collection efficiency of the XENON1T detector. The plot on the left hand side shows the position corrected ionization (cS2) versus scintillation (cS1) signal for different calibration sources. The lowest calibration data point is given through the summed signal of the ^{83m}Kr source. The plot on the right hand side shows the position depended light collection efficiency of the XENON1T detector measured with the ^{83m}Kr source. The color scale represents the collected light normalized to the mean light yield.*

Further it can be seen that although a calibration of the electronic recoil selection spectrum down to an energy of 2 keV is possible with either ^{220}Rn or CH_3T possible, the lowest point of an absolute energy calibration is given by the summed 41.5 keV transition of ^{83m}Kr. In addition ^{83m}Kr is used for the parametrization of the detectors position dependent charge collection using its summed 41.5 keV transition and the overall light collection efficiency using its 32.1 keV transition. The absolute energy calibration for electronic recoils in the XENON1T TPC and its light collection efficiency map are shown together in Figure 1.15.

A new calibration isotope with even lower mono-energetic transitions which can be diffused into a dual-phase LXe TPCs is a benefit in those regards. One isotope which fulfills those requirements is ^{37}Ar which is introduced in the next section.

1.3.2 *The Isotope ^{37}Ar*

$^{37}_{18}Ar_{19}$ decays with an half life of 35.01(2) d [B+11] via electron capture according to the reaction

$$^{37}\mathrm{Ar} \rightarrow {}^{37}\mathrm{Cl} + \nu_e \tag{1.15}$$

to ^{37}Cl. The electron is either captured from the K,L or M shell with a probability of 0.9021(24), 0.0872(20) and 0.0106(7) respectively [B+11]. The emitted mono-energetic neutrino has an energy of 811.05(20) keV, 813.60(20) keV, or 813.85(20) keV. Due to the EC induced rearrangement of the atomic shell the decay is mainly followed by a low energetic emission of Auger electrons and X-rays [B+11, M+17]. The total energy release of this cascade is 2.8224 keV, 0.2702 keV or 0.0175 keV for K,L or M shell correspondingly. [B+07]. The different average energies of the Auger electrons and energies

Table 1.2 – *Properties of the follow-up processes of the ^{37}Ar decay. Listed are the energies, emission probabilities and in average per decay emitted energies for Auger electrons and X-rays of the K- and L-shell electron capture [B+11]. It shall also be noted that the probability of the L-Auger electron emission exceeds one due to cascade effects in the atomic shell. In general it holds true that the number of vacancies in the L- or M-shell due to vacancies in the K- or L-shell respectively can be greater than one [B+11].*

Emission type	Shell	Energy [keV]	Electrons or Photons per disintegration	Energy per disintegration [keV]
X-rays	$XK_{\alpha 1}$	2,6224	0.0546(14)	0.143(4)
	$XK_{\alpha 2}$	2,6208	0.0276(7)	0.0723(18)
	$XK_{\beta 1}$	2,8156	0.0071(4)	0.020(1)
	$XL_{\beta 1}$	0.240	0.0020(4)	0.00048(10)
			X-ray total:	0.236(5)
Auger	K-LL	2.31(7)	0.689(6)	1.59(5)
	K-LM	2.57(4)	0.119(6)	0.306(5)
	K-MM	2.8	0.0051(5)	0.014(2)
	L	0.17-0.26	1.665(8)	0.38(4)
			Auger total:	2.29(6)

of the X-ray emissions as well as their emission probability for the K and L capture are given in Table 1.2. On average an energy of 2.532(5) keV is emitted per decay through Auger electrons and X-rays. Furthermore Table 1.2 shows, that an emission of Auger electrons is more likely than the emission of X-rays. Any energy losses through internal Bremsstrahlung can be neglected because the branching ratio of 0.0005 or less [B+07].

Due to its short life time, ^{37}Ar has no natural abundance and has to be synthesized by one of the three following reactions. Either through the reaction

$$^{37}\mathrm{Cl}(\mathrm{p},\mathrm{n})\,^{37}\mathrm{Ar} \tag{1.16}$$

which requires high-energy protons [K+75, W+85], the reaction

$$^{36}\mathrm{Ar}(\mathrm{n},\gamma)\,^{37}\mathrm{Ar} \tag{1.17}$$

[Hax88], or the reaction

$$^{40}\mathrm{Ca}(\mathrm{n},\alpha)\,^{37}\mathrm{Ar} \tag{1.18}$$

[B+06, A+00] which require thermal or fast neutrons correspondingly.

Since the most laboratories and facilities do not have access to thermal neutrons from a reactor or high-energetic protons from a cyclotron the most appropriated way for the production of ^{37}Ar is reaction (1.18). The reaction has a peak cross-section of 0.2 b [A+00] for neutron energies between 6 and 7 MeV [A+00]. They can be produced with a high flux α neutron source like ^{241}Am^{9}Be which has a maximal neutron energy of 11 MeV [M+17]. However this production mechanism has some drawbacks in the extraction procedure of ^{37}Ar from calcium. Depending on the used production mech-

Table 1.3 – *Table with some properties of different Argon isotopes. Listed are the natural abundances, thermal neutron cross sections, decay modes and half-life times. The thermal neutron cross sections corresponds to the (n,γ) reactions of the isotopes. Only for ^{37}Ar its the summed cross sections for the reaction (n,p) and (n,α) with an individual cross section of $69 \pm 14\,b$ and $1970 \pm 330\,b$ [Hax88].*

Isotope:	^{36}Ar	^{37}Ar	^{40}Ar	^{41}Ar
Natural Abundance [%]	0.337	-	99.60	-
Cross Section $\sigma_n[b]$	5.2 ± 0.5	2040 ± 340	0.66 ± 0.1	0.5 ± 0.1
Decay Mode	stable	EC	stable	β^-
Half-life	-	35.01 d	-	1.83 h

anism ^{37}Ar can be gained from ^{40}Ca through either one of the two following methods. In the first method some CaO powder is firstly irradiated by fast neutrons. Followed by a high temperature baking at 900 °C in order to evolve the ^{37}Ar from the powder [B$^+$06, A$^+$00]. In the second method $CaCl_2$ is first dissolved in water, which is then also irradiated by fast neutrons. In this process some of the ^{37}Ar vaporizes and ends up in a mixture of ^{37}Ar and water vapor above of the solution. Although this method does not requires any high temperature baking, it requires an extensive purification system in order to get a clean and water vapor free ^{37}Ar calibration gas [M$^+$17].

If an easy access towards a proton cyclotron is available, reaction (1.16) may be favored since it requires less effort of extracting ^{37}Ar from other reaction remnants. The reaction has a maximum cross section of 300 to 382 mb in a proton energy range of 7.0 to 12.3 MeV [K$^+$75].

The purest way of the ^{37}Ar production can be achieved through reaction (1.17). However it has two drawbacks. The first one is the requirment of thermal neutrons. Luckily the Nuclear Chemistry of the Johannes Gutenber-Universität Mainz possess a research reactor of the type TRIGA Mark-II and offers one of the only few facilities in Germany for the irradiation of materials with thermal neutrons. The second drawback is about the natural abundance of ^{36}Ar. It only has a natural abundance of 0.337 %. Hence an ^{36}Ar enriched isotope mixture has to be used which leads to higher production costs. However this option still represents the simplest and cleanest solution and was chosen for this work.

The thermal neutron cross-section σ_{Ar36} of ^{36}Ar is with its (5.2 ± 0.5) b [Hax88] one order of magnitude higher compared to the other two reactions (1.16) and (1.18). It is stated together with the reaction parameters of other for the synthesizing process important argon isotopes in Table 1.3. Comparing the thermal neutron corss-sections of Table 1.3 it becomes clear that an enrichment of ^{36}Ar above 10 % is mandatory if ^{36}Ar shall be the primary neutron absorber [Hax88]. An even higher enrichment helps to produce the desired amount of ^{37}Ar in less time, and therefore helps to suppress a burn-up of the ^{37}Ar due to its higher thermal neutron cross-section of $\sigma_{Ar37} = (2040 \pm 340)\,b$ coming from the reactions $^{37}Ar(n,\alpha)^{34}S$ and $^{37}Ar(n,p)^{37}Cl$. This burn-up process would lead to a maximum ratio of 1/400 between ^{37}Ar and ^{36}Ar given through their thermal neutron cross-sections [Hax88]. The number of produced ^{37}Ar atoms N_{Ar37} after a certain exposure time T can be derived from a set of differen-

tial equations

$$\begin{aligned} &1.) \quad \frac{\mathrm{d}N_{\mathrm{Ar36}}}{\mathrm{d}t} = -\sigma_{\mathrm{Ar36}} \cdot F_{\mathrm{n}} \cdot N_{\mathrm{Ar36}}(t) \quad \text{with} \quad N_{\mathrm{Ar36}}(0) = N^0_{\mathrm{Ar36}} \\ &2.) \quad \frac{\mathrm{d}N_{\mathrm{Ar37}}}{\mathrm{d}t} = \sigma_{\mathrm{Ar36}} F_{\mathrm{n}} N_{\mathrm{Ar36}}(t) - \lambda_{\mathrm{Ar37}} N_{\mathrm{Ar37}}(t) - \sigma_{\mathrm{Ar37}} F_{\mathrm{n}} N_{\mathrm{Ar37}}(t) \\ &\qquad\qquad \text{with} \;\; N_{\mathrm{Ar37}}(0) = 0 \end{aligned} \tag{1.19}$$

where $N_{\mathrm{Ar36}}(t)$ and $N_{\mathrm{Ar37}}(t)$ representing the number of ^{36}Ar and ^{37}Ar at a time t, N^0_{Ar36} the initial number of ^{36}Ar atoms, λ_{Ar37} the decay constant of ^{37}Ar and F_{n} the thermal neutron flux. A detailed description of the ^{37}Ar production process used for this work can be found in Section 2.2.2.

CHAPTER 2

THE MAINZ TIME PROJECTION CHAMBER (MAINZTPC) EXPERIMENT

The MainzTPC experiment was developed over the course of different Bachelor, Diploma, Master and Doctoral Theses in [Bes17, Hil14, Jen12, Kja12, Mak17, Mor12, Sch13, Sis12, Sisd]. It is a Research and Development (R'n'D) experiment for liquid xenon applications and was designed especially for the systematic study of the scintillation process as well as the study of the scintillation and charge yield of LXe for low energy electronic and nuclear recoils. The experiment can be subdivided into several different subunits whereof the actual detector, called MainzTPC, is a small dual-phase liquid xenon time projection chamber. It is designed as a primary target for Compton scatter experiments and can be operated together with a germanium detector for the study of low energy ER. A detailed study of the ER Compton scatter measurements can be found in [Sisd] and a description about the design of the Compton scatter set-up in [Sch13]. Furthermore the MainzTPC experiment was used in a Compton setup at the neutron time-of-flight facility nELBE at the Helmholtz-Zentrum Dresden-Rossendorf [A^+] for the study of low energey NR which can be further read in [Bes17].

The MainzTPC was rebuilt in Mainz and operated without any additional detector for the measurements of this work. In the following Section 2.1 the detector design of the MainzTPC and its liquid level read-out including the xenon liquefaction itself are discussed. The subsequent Section 2.2 deals with the MainzTPC gas-system which main tasks are the xenon storage, recirculation and purification as well as the introduction of calibration gases. Section 2.2 deals further with the production of the ^{37}Ar test sample. Afterwards Section 2.3 explains the read-out electronics of the MainzTPC sensors.

2.1 THE MAINZTPC

The MainzTPC is a small dual-phase liquid xenon TPC. The design was optimized for its usage as the primary target in Compton scatter experiments. Hence during the design and consruction phase which is described in [Bes17, Sisd] the following requirements were stressed.

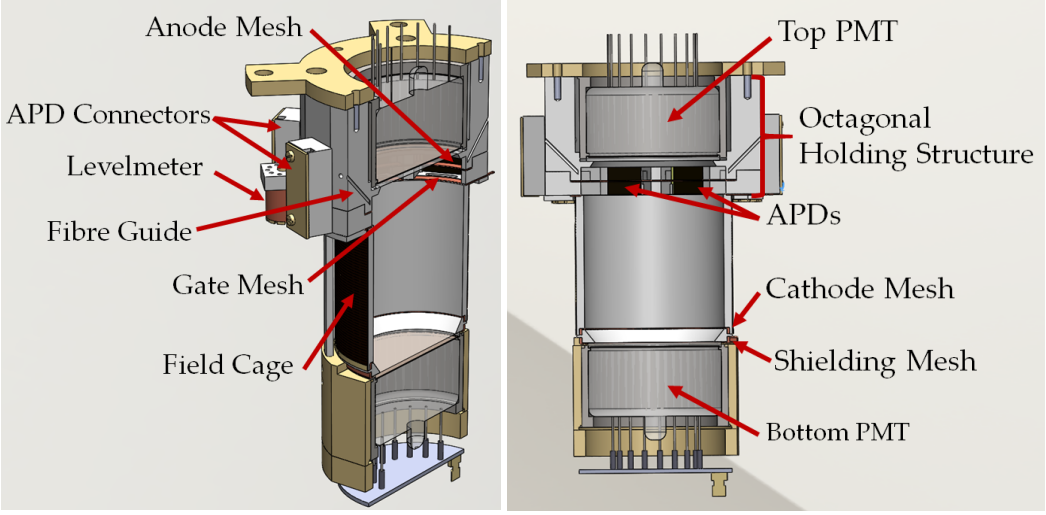

Figure 2.1 – *CAD cut drawings of the MainzTPC. The parts mentioned in the text are indicated by the red arrows. The arrows which indicate the meshes are pointing towards the mesh holding frame since the meshes themselves are not displayed. The left picture is in a slightly isometric perspective while the right picture presents a side view of the MainzTPC cut drawing*

- A small target volume in order to suppress multiple Compton scatters of incident γ-rays.
- As little passive material as possible which is important because of two reasons. First of all passive materials which are placed inside the beam line worsen the energy resolution of the detector as a result of unwanted interactions. Secondly passive materials which are placed not necessarily inside the beam line could cause "false" coincidence signals between the MainzTPC and the secondary detector of the Compton set-up due to back-scattered particles.
- A high light and charge collection efficiency, ensuring a low energy threshold and a good energy resolution.
- A uniform and stable drift and extraction field for a precise spatial resolution and high extraction efficiency of the generated electrons. The high extraction efficiency goes together with a high charge collection efficiency of the previous point.

These experimental requirements in addition to the technical and mechanical constraints led to the MainzTPC design which is shown in Figure 2.1[1].

As it can be seen in Figure 2.1 the design of MainzTPC is slightly different compared to other dual-phase time projection chamber models like they are used by the LUX or XENON collaboration. Instead of using an array of photomultiplier tubes on the bottom and top side only one monolithic 2 inch PMT is mounted on each side of the cylindrical detector volume. This maximizes the light collection since non-photosensitive

[1]The CAD model was designed by Bastian Beskers. The pictures themselves were made during this work.

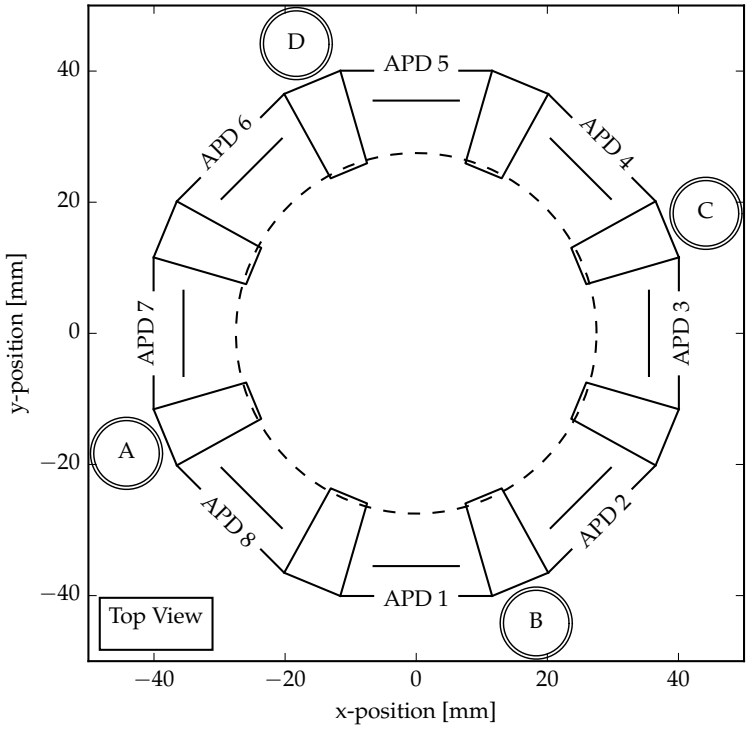

Figure 2.2 – *Top view of the MainzTPC. Shown are the positions of the eight APDs and the four TPC levelmeter which are discussed in Section 2.1.2. The APDs are indicated through long black dashes in front of their labels. The black double circles which are labeled A,B,C and D are representing the TPC levelmeters. The inner dashed circle represents the TPC meshes. The octagonal on which the APD labels are sitting shows the outer edge of the octagonal APD holding structure mentioned in the text. The black boxes which are staying perpendicular to the octagonal holding structure and overlapping with the dashed mesh circle are representing the mesh holders which also limit the field of view of the eight APDs. All measures are taken from the CAD model of the MainzTPC.*

areas are avoided. The photomultiplier tubes are of the type R6041 from the company Hamamatsu and were especially developed for applications in liquid xenon. Their quantum efficiency (Q.E.) is above 30 % for the LXe scintillation wavelength of 178 nm and have a fast time reponse with a 2 ns rise time and 0.8 ns transit time spread [B+14, Bes17].

However, the drawback of the two monolithic PMTs and the therefore high collection efficiency is the loss of the ability for any xy-position reconstruction of the detector. In order to compensate this additional Avalanche Photodiodes (APDs) are used in the MainzTPC as a second type of a photosensitive sensor. Eight APDs are placed on the edges of an octagonal shaped holding structure which also contains the top PMT. All APDs are facing radially inwards to the center of the TPC and are placed next to the liquid gas interface which is located between the gate and anode mesh. The APDs are of the model S1315 from the manufacturer RMD Inc., measuring an active area of $(14 \times 14)\,\mathrm{mm}^2$ and providing a Q.E. of 34 ± 5 % at 178 nm which was measured in [B+14]. The position of the eight APDs are shown in Figure 2.2.

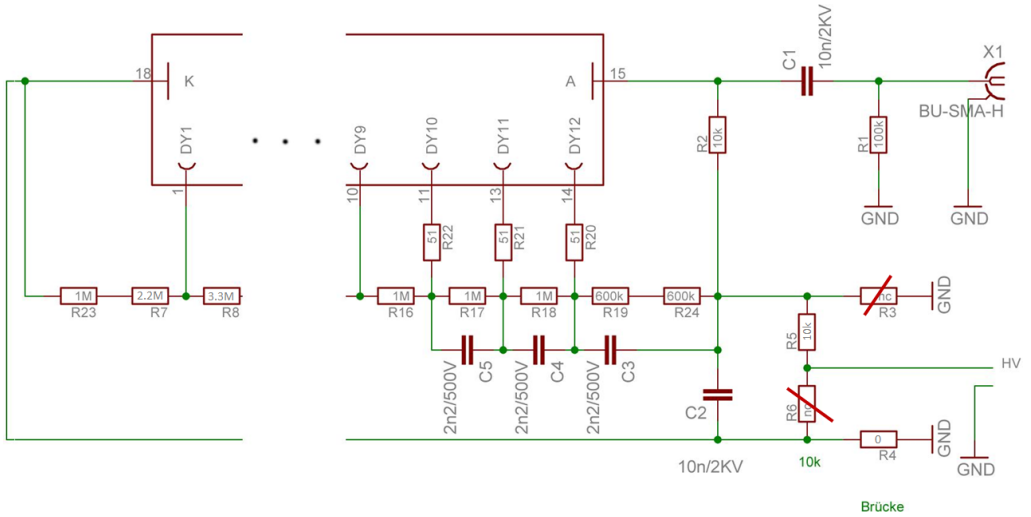

Figure 2.3 – *Schematic of the MainzTPC PMT base configuration used at the time of this thesis. The base was designed by Thomas Jennewein in [Jen12] and slightly modified in [Bes17]. It can be powered with either negative or positive high voltage depending on the mounting of the resistor R4 till R6. The resistor between dynode two and dynode three has also a value of* 3.3 MΩ *while the following dynodes are separated through a* 1 MΩ *resistor.*

The inner cylinder wall of the TPC is largely covered with polytetrafluoroethylene (PTFE) since this material has a high reflectance for VUV light. The cylindrical photon-sensitive volume of the detector has a total height of 72 mm measured between top and bottom PMT and a diameter of 53 mm, given through the PMT diameter. The distance between cathode and gate mesh is 50.5 mm which together with the diameter of the TPC defines the active liquid volume[2]. Further the active volume is surrounded by a flexible printed circuit board (PCB) which is connected on one side to the cathode through a 100 MΩ and on the other side to the gate mesh through a 200 MΩ resistor. The printed circuit acts as a field-shaping cage in order to minimize field distortions. It is a set of parallel arranged, conductive stripes which are separated through 0.2 mm spacers. They have a pitch of 1 mm and two neighboring stripes are connected with a 100 MΩ resistor. This results in a total resistance between cathode and gate mesh of 5.2 GΩ. The distance between the gate mesh which is acting as a Frisch-Grid and the anode mesh is 5 mm. An additional shielding mesh is placed between the cathode mesh and the bottom PMT since both the cathode and gate mesh are operated with negative voltages while the PMTs are biased with a positive high voltage. This ensures a proper operation of the bottom PMT since a positive bias voltage means, that the PMT housing and cathode sit on ground. A schematic of the PMT base is shown in Figure 2.3. The anode mesh can be operated either with slightly positive voltages or it is set to ground as well. All meshes were produced by the manufacturer PRECISION EFORMING LLC and are made out of Silver coated Nickel. They have a pitch of 268 µm and wire diameter of 14 µm and resulting in a transparency of 88 % [Bes17].

A photography of the MainzTPC and the cathode mesh is presented in Figure 2.4.

[2] All measures were taken from the CAD model of the MainzTPC

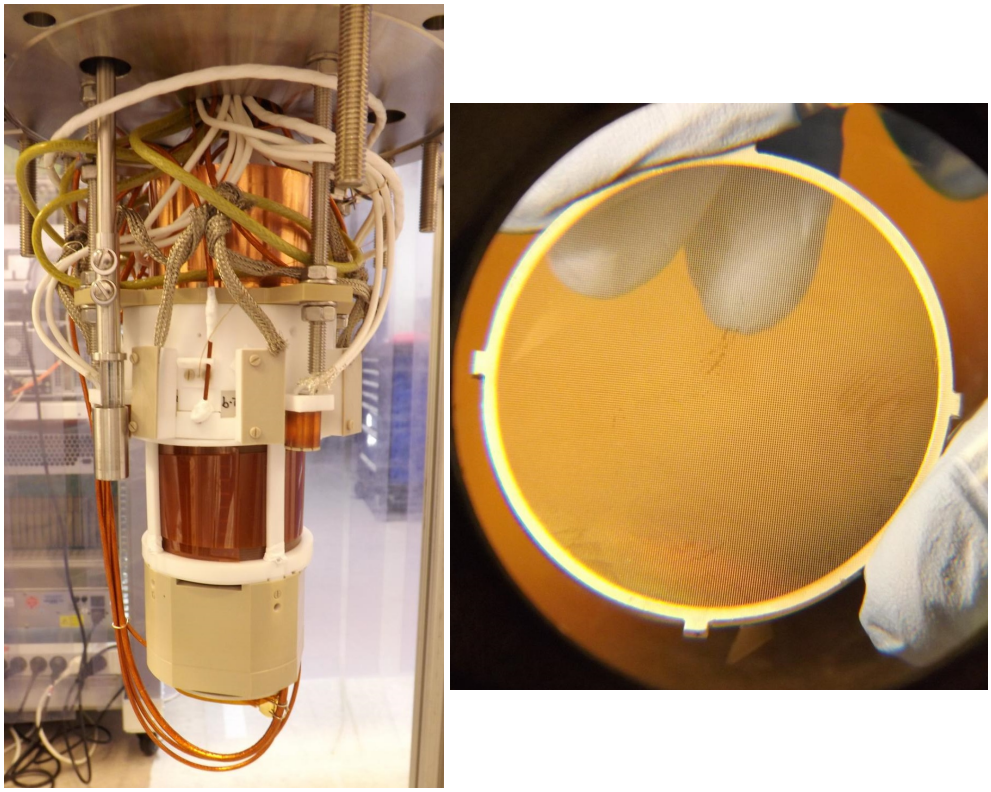

Figure 2.4 – *Photography of the MainzTPC and its cathode mesh. The image on the left hand site shows the MainzTPC fully mounted and wired. The steal tube next to the very left APD connector which is fixed to another steel rod by two screws is the old spillway for the LXe level adjustment (see Section 2.1.1). The copper housing which sits on top of the MainzTPC serves as an electromagnetic shield. The photo on the right shows the cathode mesh of the MainzTPC and was taken through a base magnifier. Both images were taken during the maintenance of the MainzTPC November 2017.*

Both pictures were taken during the maintenance of the MainzTPC in November 2017. The photography on the left hand side shows beside the sensor and mesh cables also one of the four glass fibers[3] which allow the calibration of the APDs and PMTs through an external light sources. The fiber is fed into a bore which guides it close to the inner PTFE wall of the octagonal shaped holding structure. Not using a clearance hole insures a diffuse transmission of the introduced light for a more uniformly distributed light exposure of the sensors.

Further in Figure 2.4 a small steel tube can be seen next to the very left APD connector. It acts as a spillway to set the liquid Xenon level inside the MainzTPC. This height adjustment of the LXe level as well as the Xenon liquefaction infrastructure are explained in the subsequent Section.

[3] One has to go close to the photography since the fiber is very narrow. It is coming from the upper right crossing the APD cable before it enters the fiber guide.

2.1.1 *Liquid Level and Xenon Liquefaction*

Under standard conditions xenon is in the gaseous state of matter and hence has to be liquefied before it enters the detector. This liquefaction process requires a supplementary infrastructure which provides a constant cooling power and a thermal isolation of the system. The cryogenic system of the MainzTPC was developed by Bastian Beskers and is described in [Bes17]. The cryogenic system and the LXe circuit of the MainzTPC are schematically shown in Figure **2.5** and are summarized in the following.

In order to minimize the heat transfer and thus the overall required cooling power, both the MainzTPC and its cryogenic system are thermally isolated from the surrounding environment. Therefore the vessel of the MainzTPC and the vessel in which the GXe is liquefied are put into separate cryostats which are connected with each other through an intermediate pipe. The whole system is evacuated by a turbo molecular pump of the model TURBOVAC 150 which is supported by a scroll pump of the model SCROLLVAC SC15D both from the manufacturer Leybold [Leya, Leyb]. The isolation vacuum of the MainzTPC is in the order of $3.4 \cdot 10^{-3}$ mbar. In addition to the suppression of the conductive heat transfer through the isolation vacuum, the vessel of the MainzTPC is largely covered with a ten-layered reflective Mylar foil reducing the amount of heat load coupled into the system by thermal radiation.

The main cooling power for the MainzTPC is provided by a Pulse-Tube Refrigerator (PTR) model 2S132W from the manufacturer QDrive. It sits on top of the cryostat which contains the vessel for the xenon liquefaction and provides its cooling power via a copper cold head. Once the GXe condensates at the copper cold head it drops down onto the vessel which then guides the LXe with its funnel-shaped body through a pipe towards the MainzTPC. The PTR itself is operated in constant power setting and counter-heated with two 25 W load resistors which are mounted to the PTR cold head outside of the vessel.

In addition to the PTR an extra copper spiral is mounted to the liquefaction vessel. Through this copper spiral additional cooling by liquid Nitrogen (LN2) can be supplied if the PTR cooling fails or as an additional source of cooling power during the initial liquefaction process when the system is still warm.

Due to the recirculation, cool GXe which is coming from the MainzTPC is constantly exchanged by warm GXe from the gas-system. In order to improve the thermal stability of the cryogenic system and lower the thermal load the warm inflowing GXe is precooled through a heat exchanger of the model GBS-300 from the company GEA [GEA] with the cold evaporated GXe.

The whole thermodynamics of the MainzTPC, its LXe circuit and gas-system is controlled and monitored through a variety of temperature and pressure sensors. The different sensors are read out through several different devices which are embedded into a superior Slow Control System (SCS). The heart of this SCS is a cryogenic temperature controller model CTC100 of the manufacturer Stanford Research Systems. This device is acting as a PID-controller which provides a certain power to the counter heaters depending on the temperature difference between the temperature of the PTR cold head $T_{\mathrm{PTRcoldfinger}}$ and the set temperature value. For a more detailed description of the SCS the reader is referred to [Bes17, Kja12].

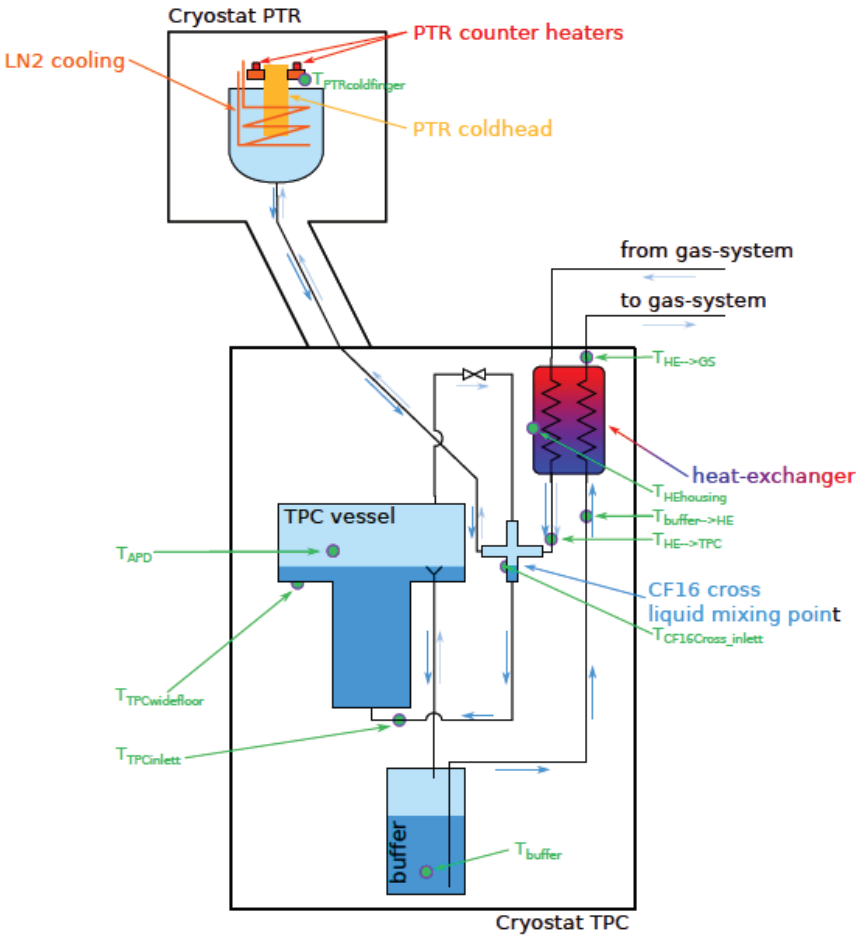

Figure 2.5 – *Schematic of the cryogenic system of the MainzTPC. The schematic shows the liquefaction process of the gaseous (light blue) and the level of the liquid xenon (dark blue) inside the MainzTPC. The flow of the Xenon is indicated by the small arrows next to the pipes. The position of different temperature sensors are indicated in green. All other devices indicated by arrows are explained in the text. The schematic was taken from [Bes17].*

Once the xenon is liquefied and inside the MainzTPC its level can be set with a spillway whose height can be adjusted by a linear feed-through. The linear feed-through has a precision of 0.0001 inch and can cover a height adjustment of 1 inch in total [Bes17]. The spillway is fitted through a clearance fit into a pipe guiding the drained LXe into a buffer volume which acts a siphon. Although the height adjustment of the LXe level works in principle, the spillway system causes periodical level fluctuations which were already extensively studied in [Bes17]. These level fluctuations affect the electroluminescence which depends on the drift distance in GXe and the strength of the electric field and hence worsen the overall S_2-resolution of the detector. A new spillway which shall improve this behavior was also studied during this work. It had been developed and designed with the aid of our bachelor research assistant David Maksimovic. The old spillway is presented in Figure 2.4 left hand side,

Figure 2.6 – *Picture of the new spillway of the MainzTPC. Shown is the MainzTPC after its maintenance November 2017. The new spillway was designed by our Bachelor research assistant David Maksimovic and has compared to the old model a deep v-cut. Further all edges which are in contact with the LXe were sharpened in order to minimize the surface barrier the liquid has to overcome.*

the new spillway is shown in Figure 2.6. An analysis of the level fluctuation with the new spillway and a discussion about its development are given in Section 4.7.

In order to be able to study the liquid level of the MainzTPC it has to be measured in an adequate way. For this purpose the MainzTPC is equipped with five levelmeters. Four of them are placed next to the MainzTPC itself and one sits inside the buffer volume. Their design and working principle are presented in the following Section.

2.1.2 *Liquid Level Readout*

The liquid level of the MainzTPC is measured by four levelmeters sitting symmetrically distributed next to the APD connectors on the outer side of the octagonal shaped holding structure. The position of one levelmeter is shown in Figure 2.1 on the left hand side. The working principle of the levelmeter is based on the proportionality of the capacity of a plate capacitor and the dielectric constant ϵ_r of the medium between the two plates. In the case of gaseous and liquid xenon is the dielectric constant given by $\epsilon_{GXe} = 1.00126$ and $\epsilon_{LXe} = 1.96$ [Bes17, Gei18].

The levelmeter in the MainzTPC have a cylindrical shape and are made out of oxygen-free copper. The inner cylinder of the levelmeter is a full cylinder measuring a radius of $r_1 = 5.0\,\text{mm}$ and a height of $h = 10\,\text{mm}$, while the outer cylinder is a hollow cylinder with an inner radius of $r_2 = 5.5\,\text{mm}$, a wall strength of 0.5 mm and an height of 12 mm. The design capacity C of the MainzTPC levelmeter can be estimated by the formula for a long double cylinder

$$C = 2\pi\epsilon_0\epsilon_r \frac{h}{\ln(r_2/r_1)} \tag{2.1}$$

where ϵ_0 is the permittivity of the free space and ϵ_r the dielectric constant. The empty

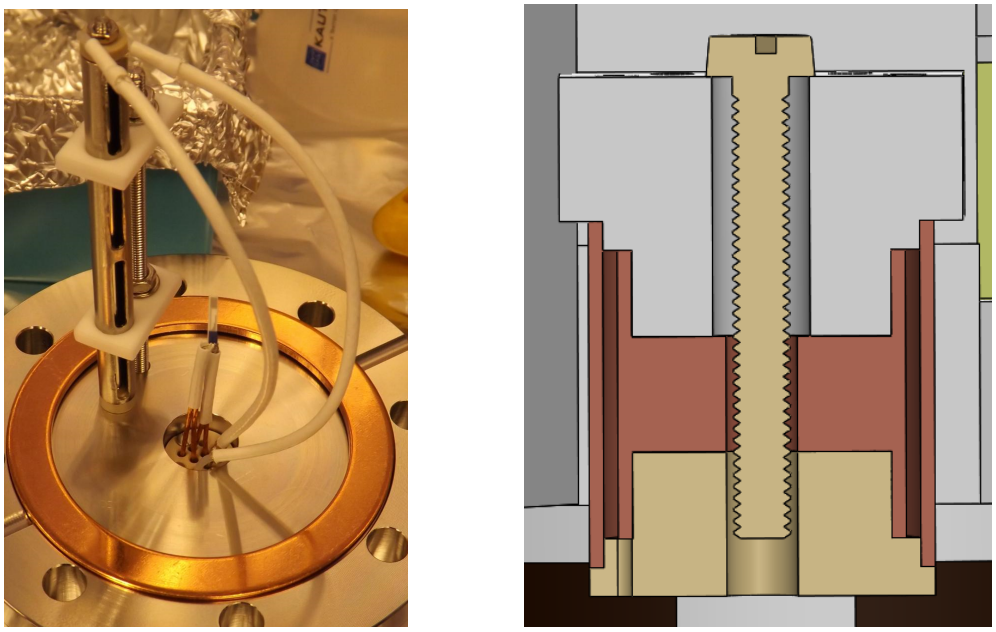

Figure 2.7 – *Photography of the buffer and CAD cut drawing of the TPC levelmeter. The picture on the left hand side shows a photography of the MainzTPC buffer levelmeter. Further the temperature sensor T_{buffer} can be seen in the center of this image. The image was taken during the maintenance of the MainzTPC November 2017. The picture on the right shows a CAD cut drawing of the MainzTPC levelmeter. The brownish colored part represents the inner full and outer hollow cylinder.*

levelmeter has therefore a capacity of $C_{\text{empty}} = 5.84\,\text{pF}$, only filled with gaseous xenon (GXe) and a capacity of $C_{\text{full}} = 11.44\,\text{pF}$ when it is filled completely with liquid xenon [Bes17]. One additional levelmeter is placed inside the buffer volume. It is made out of a stainless steel tube with a height of 88.9 mm, an inner diameter of 6.35 mm and a wall strength of 0.825 mm as well as a stainless steel rod as inner cylinder with a diameter of 3.175 mm. The buffer levelmeter has a design capacity of $C_{\text{empty}} = 7.14\,\text{pF}$ when it is empty and a capacity of $C_{\text{full}} = 13.99\,\text{pF}$ when filled with LXe [Bes17]. The liquid level h_{LXe} measured by any capacitive levelmeter can be calculated by

$$h_{\text{LXe}} = h\,\frac{C_{\text{LXe}} - C_{\text{empty}}}{C_{\text{full}} - C_{\text{empty}}}\,, \tag{2.2}$$

where h represents the height of the inner cylinder and C_{LXe} the measured levelmeter capacity of a given LXe level. The buffer and TPC levelmeter are shown together more detailed in Figure 2.7.

The capacities of the levelmeter are measured by an Universal Transducer Interface (UTI) chip developed by the manufacturer SmarTec [Sma16] which is readout by their commercially available evaluation board. It uses a two-port measurement technique in order to short-cut any parasitic capacitance coming from the used cable. Hence a measurement down to even femto-Farad becomes possible [Sma16]. Each board and UTI chip is capable to read out four capacities, whereof one capacity has to be a well defined reference capacity to compensate for any UTI internal sources of uncertainties.

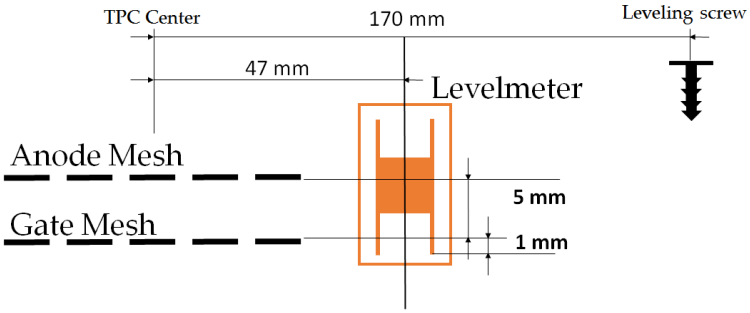

Figure 2.8 – *Schematic of the MainzTPC level adjustment. The schematic shows all relevant distances for leveling the TPC. The center between the anode and gate mesh lies* 3.5 *mm above the lower edge of the inner levelmeter cylinder.*

Otherwise the measured vaues of two different UTI boards would not be comparable. Each channel is operated in a 0-12 pF readout mode. Also higher capacities can be read out in this mode, as long as the measured capacity is still in the same order of magnitude. However a higher capacity can only be measured at the cost of accuracy. For a more detailed description of the measurement routine of the UTI evaluation boards is the reader refereed to [Gei18, Sma16].

For the MainzTPC two of the evaluation boards are used which from now on are referred to UTI-1 and UTI-2. UTI-1 is measuring the levelmeter B, C and D of the MainzTPC, and UTI-2 is measuring the levelmeter A and the buffer levelmeter. The position of the four levelmeter is sketched in Figure 2.2 on page 32. UTI-2 can be also used for the capacity measurement of the anode and gate mesh if required. The four TPC levelmeter are connected via a multi-pin feed-through to the two UTI evaluation boards which are sitting inside a steel housing. The buffer levelmeter is connected to UTI-2 via a separated multi-pin feed through.

Beside measuring the average height of the liquid xenon level, the four levelmeters are used also to measure the tilt of the MainzTPC and can therefore be used to straighten the liquid level. Depending on the measured tilt three leveling screws can be turned independently from each other in order to adjust the overall tilt of the MainzTPC and its outer cryostat. All relevant distances for the leveling of the MainzTPC are presented in Figure 2.8.

2.2 GAS-SYSTEM

Operating a LXe dual-phase TPC requires beside a cryogenic system for the xenon liquefaction an additional subsystem for the storage and purification of the xenon gas. These two aspects were merged together in the gas-system of the MainzTPC, which was developed in [Hil14]. In addition to the xenon storage and purification it provides, the possibility to introduce gaseous calibration sources into the MainzTPC. The gas-system of the MainzTPC is sketched in Figure 2.9. It can be subdivided into three main units each taking care of one of the mentioned aspects.

When the MainzTPC is not operated the xenon is stored in one of two commercially

available aluminum gas bottles labeled with A and B in Figure 2.9. They are separated from the rest of the gas-system through high pressure valves labeled with HP-Vx. In order to reduce the high pressure of the stored xenon to a more moderate operation pressure, it is regulated by a pressure reducer (HP-PR1)[4] down to 2 to 3 bar while filling the MainzTPC. After each measurement run the used xenon has to be recovered since it is more expensive than other gases like nitrogen or helium. In order to do so one of the gas bottles is put into a dewar which is then filled with LN2. This leads to a freeze-out of the xenon on the inner bottle walls which causes a vacuum inside the bottle and sucks the used xenon from the TPC and the rest of the gas-system in. While filling and recuperating the xenon flow is always measured by the SCS with a flowcontroller (A-FC) model HFC-302-H from the manufacturer Hastings [Tel]. This allows a mass integration of the flowing xenon and ensures a proper recovery of the used xenon.

During the operation of the MainzTPC the most important part of the gas-system is the recirculation and purification section. The xenon is constantly circulated from the MainzTPC and its buffer volume through the gas-system and back. This constant flow leads to a periodic evaporation and condensation of the xenon and thus to a stable liquid level. The evaporated xenon is circulated by a double-diaphragm pump (A-MP) of the type N143AN.12E from the manufacturer KNF [KNF] allowing a maximal flow rate of 30 slpm. Using a double-diaphragm pump pump ensures, that no xenon is lost if the diaphragm gets damaged. The pump inlet and outlet pressure is permanently monitored by the SCS through the pressure sensors A-P1 and A-P2. Further the pump by-pass valve (A-V2) allows a regulation of the pump inlet pressure which should always be above 1 bar. This ensures that no impurities diffuse through the pump membrane into the system. The normal pump inlet pressure is set to 1.25 bar during recirculation. While the diaphragm pump is the heart of the recirculation system (circulating the xenon) a so-called hot getter is the kidney or liver of the MainzTPC. It chemically binds electronegative impurities like H_2O, O_2 or N_2 to a hot zirconium surface and separates them from the circulated xenon. The hot zirconium surface getter is from the manufacturer SAES group, type PS4-MT3. Its nominal recirculation speed is 5 slpm where the optimal purification level of less than 1 ppb is reached [sae02].

The dosimetry branch of the gas-saystem is the third sub-unit of the gas-system. It allows the safe introduction and precise dosing of calibration gases. It is explained more detailed in the following section.

2.2.1 *Dosimetry Branch*

The part of the gas-system most outstanding for this work is the dosimetry branch. The basic concept was already designed in [Hil14], but was not used. After a first concept study of the initial design some changes were made which led to the dosimetry branch sketched in Figure 2.9. Its basic concept is described below, while a detailed discussion of the calibration gas injection can be found in Section 3.3.1.

[4] In the following paragraphs the labels inside of the round brackets are referring to the schematic labels in Figure 2.9.

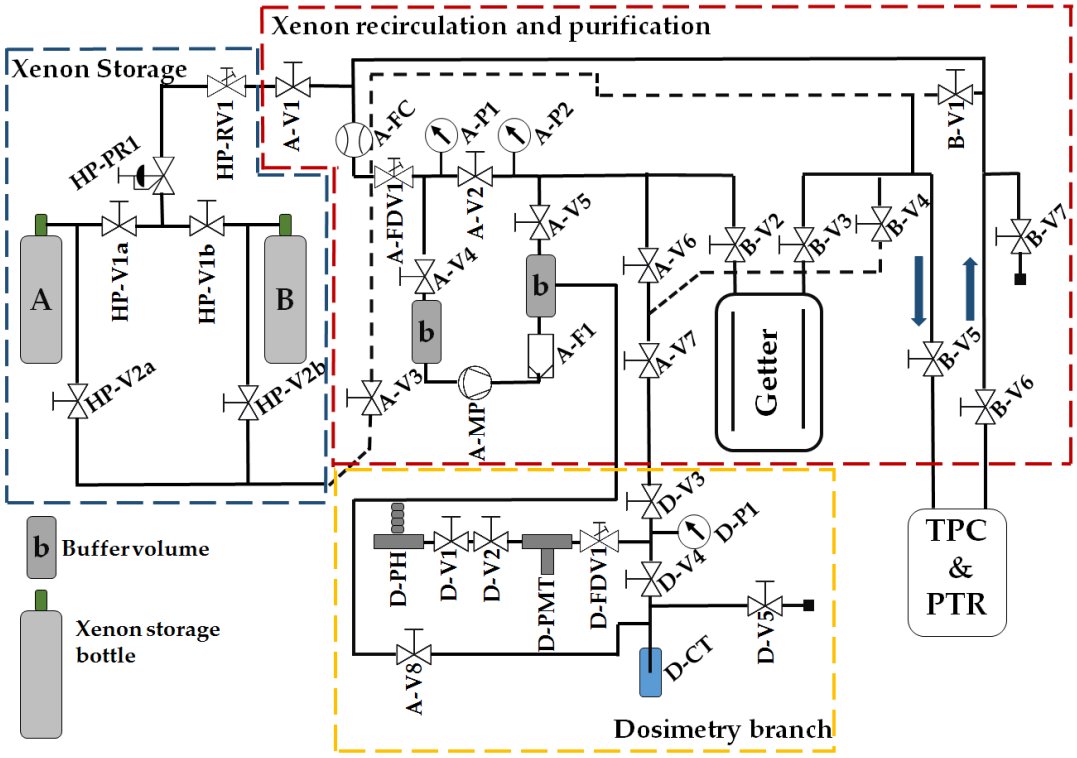

Figure 2.9 – *Schematic of the MainzTPC gas-system. The gas-system is subdivided into three main parts: a high pressure side for the xenon storage (blue dashed frame), a recirculation and purification circuit for xenon gas while operating the MainzTPC (red dashed frame) and a dosimetry branch for the induction of gaseous calibration isotopes (orange dashed frame). The piping of the gas-system is done in two layers. The front layer is presented with solid black lines while the second layer which is placed slightly deeper into the gas-system from the front perspective is shown with black dashed lines. The blue arrows indicate the regular flow direction of the gaseous xenon.*

The dosimetry branch itself can be subdivided further into a dosimetry unit and a filling unit. Both are shown together in Figure 2.10. The dosimetry unit consists out of several volumes seperated by valves in order to ensure a precise and controlled dosage. Those volumes include a mechanism for opening a quatz ampule in (D-PH) and a PMT for an initial activity measurement in (D-PMT). The latter is important since the 2.8 keV X-rays and Auger electrons emitted due to the ^{37}Ar decay are too weak to penetrate the quartz ampule. Thus the activity can only be measured, when the ampule was opened. This is the major change compared to the dosimetry branch designed in [Hil14]. In the initial design the activity would have been measured while the recirculation of the xenon calibration gas mixture after its introduction procedure. For the activity measurement the dosimetry unit contains GXe at around 2 bar.

Since the ^{37}Ar sample is stored in a sealed quartz ampule it has to be opened first. Therefore a guillotine like mechanism in D-PH was developed and designed in [Hil14]. A CAD model of the guillotine can be found in Figure 5.4 in the Appendix on page 115. It is placed inside the bellow shown on the very left of Figure 2.10. By pushing this bellow completely downwards a sharpened edge will cut off the head of the mounted

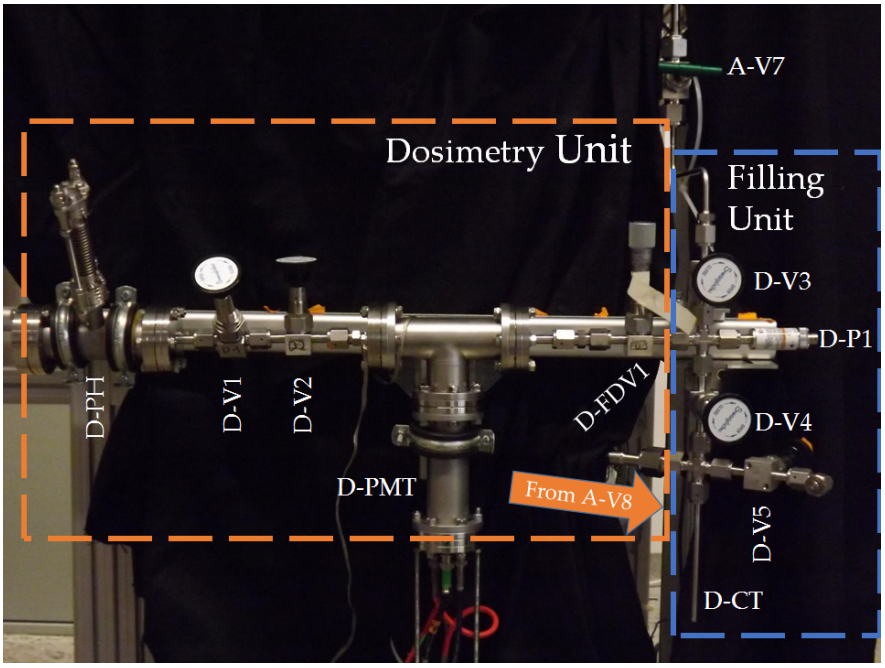

Figure 2.10 – *Dosimetry branch of the MainzTPC gas system. The dosimetry branch is subdivided into a dosimetry unit and a filling unit indicated by the colored dashed boxes. The rest of the gas system is curtained off by a black blanket. In order to aid the reader the connection which is coming from the valve A-V8 is indicated by an orange arrow.*

quartz ampule. In order to keep the ampule in place it is put inside a Polyether ether keton (PEEK) holder. The ampule together with its the PEEK holder is shown in the subsequent Section 2.2.2 in Figure 2.12. Once the ampule is opened the stored calibration gas will diffuse into the surrounding xenon.

After the diffusion process the intermediate volume between the valves D-V1 and D-V2 allows a first rough dosing of the calibration gas and its initial activity A_0. The rough dosing activity A_r is given by the volume ratio

$$A_\mathrm{r} = \frac{V_\mathrm{r}}{V_\mathrm{DPH} + V_\mathrm{r}} A_0 \tag{2.3}$$

of the guillotine unit V_DPH and the intermediate volume V_r, where the initial calibration gas activity is calculated by the decay law and the passed time between the date of irradiation and the date of usage. After a certain amount of time valve D-V1 is closed and valve D-V2 is opend. The rough dosed amount of ^{37}Ar spreads then across the T-volume (D-PMT) where a 1 inch squared PMT of the type R8520-06-AL from the manufacturer Hamamatsu is placed. It is the same type of PMT as used in XENON100 [A$^+$12]. It sits in the pipe junction of the T-shaped volume facing upwards into a small PTFE cylinder which is shown in Figure 2.11. The PTFE cylinder defines a fixed and simple volume and therefore allows a proper measurement of the activity per unit volume $A_\mathrm{mes}/V_\mathrm{mes}$. Further the PTFE maximizes the light collection efficiency of the PMT since it has a higher VUV reflectance compared to stainless steel. The total amount of

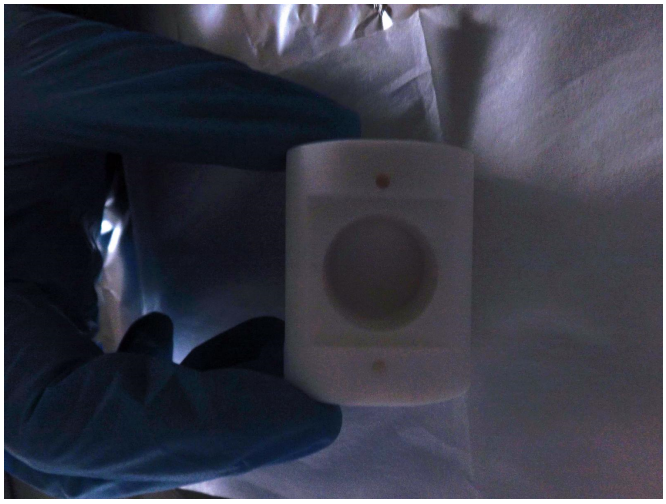

Figure 2.11 – *Photography of the PTFE measurement chamber of the dosimetry PMT. The cylindrical volume V_{mes} has a height of 35 mm of and a diameter of 20.1 mm, measured with a caliper. The squared recess on top of the cylindrical volume serves as holder for the 1 inch PMT.*

activity inside the T-piece (D-PMT) A_T is then simply given by the activity per unit volume times the unoccupied volume of the T-piece V_{DPMT}.

In the last step the filling unit is used for a precise fine-dosing of the measured activity A_T. In order to do so the intermediate volume of the 1/4 inch VCR[5] union cross between the fine regulation valve (D-FDV1) and the valve D-V4 is evacuated with the aid of a small cold trap (D-CT). The pressure during this process is monitored with a pressure gauge with the corresponding sensor (D-P1) which is also mounted to the VCR cross. Once the pressure gauge of D-P1 shows less than 1 mbar the valve D-V4 is closed. Afterwards a small out flow of the xenon calibration gas mixture from the T-piece volume into the 1/4 inch VCR cross can be set with the fine regulation valve D-FDV1. The total introduced activity A_{int} is then given by

$$A_{int} = A_T \cdot \frac{V_{cross} \cdot p_{mes}}{V_{DPMT} \cdot p_{pre}} \tag{2.4}$$

where V_{cross} is the volume of the VCR Union cross, p_{pre} the pre-set pressure in the dosimetry unit and p_{mes} the measured pressure of D-P1 while introducing the gas.

Since most of the dosimetry branch volumes have a rather complex shape, they were not measured classically with a caliper. Instead dry nitrogen was used for the volume estimation. This procedure is discussed in more detail in Section 3.3.1.

2.2.2 *The Ar^{37} probe*

For the measurements during this work an ^{36}Ar sample already prepared in [Hil14] was used. The sample contained an ^{36}Ar enriched isotope mixture with an abundance

[5] VCR is a product series from the manufacturer Swagelok [Swa]

of 99.935 % ^{36}Ar, 0.064 % ^{38}Ar and 0.001 % ^{40}Ar. This isotope mixture had been filled with a filling set-up of the group from Professor Heil into a small evacuated quartz tube, which was sealed afterwards by the in-house glassblower of the Institute for Physics. The obtained quartz ampule had a total amount $m^{\text{amp}}_{\text{Ar36}} = 0.288\,\text{mg}$ of ^{36}Ar in it which was calculated in [Hil14] by simply using the volume ratio

$$m^{\text{amp}}_{\text{Ar36}} = \frac{V_{\text{amp}}}{V_{\text{tot}}} m^{\text{tot}}_{\text{Ar36}} \tag{2.5}$$

of the filling set-up, where $m^{\text{tot}}_{\text{Ar36}}$ is the total amount of ^{36}Ar inside the storage bottle and $\frac{V_{\text{amp}}}{V_{\text{tot}}}$ is the ampule volume divided by the total volume of the filling set-up[6] and the storage bottle. For a further reading about the filling set-up and filling process the reader is referred to [Hil14].

The received quartz ampule was irradiated according to the reaction (^{36}Ar(n,γ)^{37}Ar) with thermal-neutrons coming from the TRIGA Mark-II of the Nuclear Chemistry department at the Johannes Gutenberg-Universität Mainz. The sample was irradiated in the central exposure pipe for $T = 165\,\text{min}$ with a thermal-neutron Flux of $4.2 \cdot 10^{12}\,\text{cm}^{-2}\,\text{s}^{-1}$ [Nuc]. Based on the set of differential equations which were presented in (1.19) and the ^{36}Ar properties specified in Table **1.3** an estimate of the ^{37}Ar activity can be derived. In order to simplify equation 2.) of (1.19) the second term which accounts for the ^{37}Ar decay was set to zero, since the exposure time T is much smaller than the half-life $\tau^{\text{Ar37}}_{1/2}$ of ^{37}Ar. Solving (1.19) then leads to

$$N_{\text{Ar37}}(t) = \frac{\sigma_{\text{Ar36}}}{\sigma_{\text{Ar37}} - \sigma_{\text{Ar36}}} N^0_{\text{Ar36}} \left(\exp^{-\sigma_{\text{Ar36}} F_{\text{n}} t} - \exp^{-\sigma_{\text{Ar37}} F_{\text{n}} t} \right) \tag{2.6}$$

and resulting the ^{37}Ar activity is given by

$$\begin{aligned} A_{\text{Ar37}}(t) &= \lambda \cdot N_{\text{Ar37}}(t) \\ A_{\text{Ar37}}(t) &= \ln(2) \frac{\sigma_{\text{Ar36}}}{\sigma_{\text{Ar37}} - \sigma_{\text{Ar36}}} \cdot \frac{N^0_{\text{Ar36}}}{\tau^{\text{Ar37}}_{1/2}} \left(\exp^{-\sigma_{\text{Ar36}} F_{\text{n}} t} - \exp^{-\sigma_{\text{Ar37}} F_{\text{n}} t} \right), \end{aligned} \tag{2.7}$$

where the initial number of ^{36}Ar atoms N^0_{Ar36} was estimated through the filled ^{36}Ar mass $m^{\text{amp}}_{\text{Ar36}}$ divided by its molar mass of 36 g/mol. This leads to an ^{37}Ar activity of (238 ± 62) kBq, wheerby the uncertainty of the activity was calculated through a Gaussian error propagation of Equation (2.7) in which only the parameters σ_{Ar36}, σ_{Ar37} and N^0_{Ar36} were used since the other uncertainties are neglectable. The relative uncertainty of N^0_{Ar36} is 14 % and was calculated based on a Gaussian error propagation of Equation (2.5) and the volume uncertainties stated in [Hil14]. The derived formula for the uncertainty of $A_{\text{Ar37}}(t)$ is given by Equation (5.1) and can be found in the Appendix A. on page 112. The Nuclear Chemistry department estimated independently an ^{37}Ar activity of 246 kBq which is in agreement with the derived value of this work. The quartz ampule which contained the ^{37}Ar test sample is shown in Figure **2.12**.

It should also be mentioned here, that the used ^{37}Ar sample was irradiated in total

[6] Including the ampule volume.

Figure 2.12 – *Quartz ampule which was used for the irradiation of the enriched ^{36}Ar isotope mixture. The picture on the left hand side shows the quartz ampule after its irradiation. Due to safety reasons the ampule was put into a sealed plastic envelope before it irradiation. The paper in the background is a normal plotting paper as a size reference. The photography on the right shows the remnants of the quartz ampule after its usage in the MainzTPC. The tail of the ampule is clear-cut while the body is still mounted to the ampule holder of the guillotine.*

four times with the same exposure configuration between its production and its final use in this thesis. However this does not have a large effect on the ^{37}Ar concentration since the number of ^{37}Cl atoms coming from the ^{37}Ar decay is still in the ppm level which was estimated by assuming a fixed activity of 250 kBq for a total time of $4 \cdot 5 \cdot \tau_{1/2}^{Ar37}$.

^{37}Ar has a long decay time with 35.01(2) d compared to other calibration gases like ^{83m}Kr or ^{220}Rn and therefore has to be actively removed from the LXe after the calibration measurement. Like ^{83m}Kr, ^{37}Ar can be separated from xenon by a cryogenic distillation due to their different boiling temperatures of 165.05 K for xenon and 87.3 K for argon [Air]. However this cannot be tested in the set-up of the MainzTPC since such a facility does not exist in the Mainz laboratory.

2.3 DATA ACQUISITION (DAQ) SYSTEM AND READOUT ELECTRONICS

During the measurements for this thesis the same readout electronics as in [Bes17, Sisd] were used. The Data Acquisition system of the MainzTPC uses a variation of different modules based on the Versa Module Eurocard (VME) bus and Nuclear Instrumentation Module (NIM) standard. Therefore a NIM and VME crate are located next to the detector. Also most of the sensors and meshes are powered through modules in those two crates.

In Section 2.3.1 the used sensor amplifiers for the PMTs and APDs are introduced. Subsequent in Section 2.3.2 the DAQ system of the MainzTPC which was developed in [Sisd] is discussed. Section 2.3.3 deals with the used high voltage power supplies for the different sensors and meshes. The Section 2.3.4 describes briefly the used data format of the MainzTPC DAQ system and the working principle of the raw data analysis framework. The last Section 2.3.5 deals shortly with the high level analysis framework

which was written in Python and set-up for this thesis.

2.3.1 *Amplifiers*

Three different types of amplifiers were used for the measurements in this thesis. Their properties and application are summarized below.

The **Detector Lab Amplifier** was developed in cooperation with the PRISMA Detector Laboratory of the Johannes Gutenberg-Universität Mainz. It was originally designed for applications with Silicon Photomultiplier (SiPM) and modified for the use as PMT amplifier. The amplifier is based on a high speed current feedback amplifier of the type AD8009 from the manufacturer Analog Devices, Inc [Ana]. It is a single channel amplifier whose PCB was adapted to provide a passive split output with a gain of 10.5 each. The amplifer is powered by a commercial +12 V NIM power module in addition to an on board DC-DC-converter which converts the +12 V into ±5 V [Bes17].

The **KPH Amplifier** was developed by the institute for nuclear physics of the JGU. Like the Detector Lab Amplifier the KPH Amplifier uses a high speed current feed back amplifier of the model THS3201 from Texas Instruments [Tex]. The amplification is done in two steps resulting in a two channel output with a gain factor of 5 each. The amplifier is powered with ±7.5 V coming from a 230V(AC)-to-7.5V(DC) converter [Bes17].

The last amplifier used, is a charge sensitive pre-amplifier model A1422 in the 4-channel-box version with the 200 pF and 400 mV/MeV specification, from the manufacturer CAEN [CAEa]. Two of them are used to convert the APD charge signal into a voltage signal which is read out by the MainzTPC DAQ system.

2.3.2 *Data Acquisition System*

The heart of the DAQ system are the two flash analog-to-digital converter (FADC) **SIS3305** and **SIS3316** from the manufacturer Struck Innovation Systems [SISb, SISc].

The **SIS3316** is a 16-channel digitizer with 16 bit resolution, 125 MS/s sampling rate per channel and an analog bandwidth of 62.5 MHz. Its input impedance is programmable and the dynamic voltage range can be set either to ±1 V or ±2.5 V. In order to match the signal properties of the connected sensor a baseline offset over the full dynamic range and the signal polarity can be set too. The sampled signals are stored in a ring buffer which allows to avoid any dead-times while recording and to assign a pretrigger window to each sampled waveform. The maximal allowed waveform length is 32 MSamples (256 ms) with a maximum pretrigger of 16378 samples (131.024 μs).

Since one design goal of the MainzTPC is, to improve the understanding of the LXe scintillation shape (fast decay component $\tau \approx 4$ ns) a second FADC with a faster sampling rate is required. Therefore the **SIS3305** with a maximum sampling rate of 5 GS/s is used. The SIS3305 is a 8-channel digitizer with a sampling rate of 1.25 GS/s per channel and a 10 bit resolution. An on-board multiplexer allows to double the sampling rate when the number of recorded channels is halved. For the MainzTPC

the SIS3305 is operated in the two channel 5 GS/s mode. The dynamic range of the board is 0 V to -1 V and has an analog bandwidth of 2 GHz. Also the SIS3305 uses a ring buffer which allows a maximal waveform length of 12288 samples (2457.6 ns) and a pretrigger of 24552 samples (4910.4 ns) according to the manual.

Both boards are controlled by a VME-bus standard from a nearby computer via a SIS1100 Peripheral Component Interconnect (PCI) board and a optical cable link towards the SIS3100 VME board [SISa]. They are initialized and configured by the MainzTPC DAQ program written by Pierre Sissol in [Sisd]. The board settings are specified with two Extensible Markup Language (XML) files, the hardware.xml and settings.xml file. The hardware.xml, as its name suggests, configures hardware settings like: which board and which channel is enabled or which dynamic range and offset should be used. While the settings.xml file controls all values relevant for the measurement like sample length of the waveform and pretrigger as well as trigger thresholds and the setting of a so-called Moving Window Integrator (MWI) which is explained in the following. For a more detailed description of the MainzTPC DAQ program the reader is refered to [Sisd].

The SIS3316 can be either triggered externally through a NIM-signal or internally using a MWI filter together with a constant fraction discriminator. The working principle of a MWI is illustrated in Figure 2.13. While the MWI is rolling over the data it weighs all bin entries which are inside the MWI window with the corresponding value of 0 or ± 1 depending in which part of the MWI they are. Afterwards the weighted values are summed up to a single new entry. E.g. consider the case in which the MWI of Figure 2.13 covers the whole red signal: the entries of the sample 7 and 8 are weighted with -1 while the entries of sample 10 and 11 are weighted with $+1$; the central sample is weighted with zero. Hence the value of sample 11 in the filtered signal adds up to -1 like it is shown. Furthermore it should be noted that the double-sided threshold (high and low) of the constant threshold discriminator is applied to the filtered waveform. The peak- and gap-time of the MWI as well as the trigger thresholds are specified in the settings.xml. Moreover the SIS3316 firmware provides the possibility to set-up different coincidence modes if required. Depending on the MWI setting the DAQ can be triggered either by a S_1 or S_2 signal.

The overall trigger of the DAQ is generated by the SIS3316 board. It allows to record both S_1 and S_2 in a single waveform while the maximal waveform length of the SIS3305 is too short for this. Hence the SIS3305 is triggered by the SIS3316 and measures only a small excerpt around the S_1-signal. For the regular measurements with the TPC the DAQ was triggered by the SIS3316 internally, while for the sensor calibration with an external light source a NIM pulse was used as trigger signal. A schematic which shows the whole electronic read-out chain used during this work is shown in Figure 2.14.

The signals of the eight APDs were amplified by the CAEN A1422 charge-sensitive preamplifier and recorded by the channels 4 to 12 of the FADC SIS3316. Each PMT of the MainzTPC is amplified with one Detector Lab Amplifier. However since the amplitude of the PMT S_1 and S_2 signal can cover a range beyond the maximal output voltage of the Detector Lab Amplifier, their signals are first split passively with a simple voltage divider. This allows to record the unamplified signal when the Detector

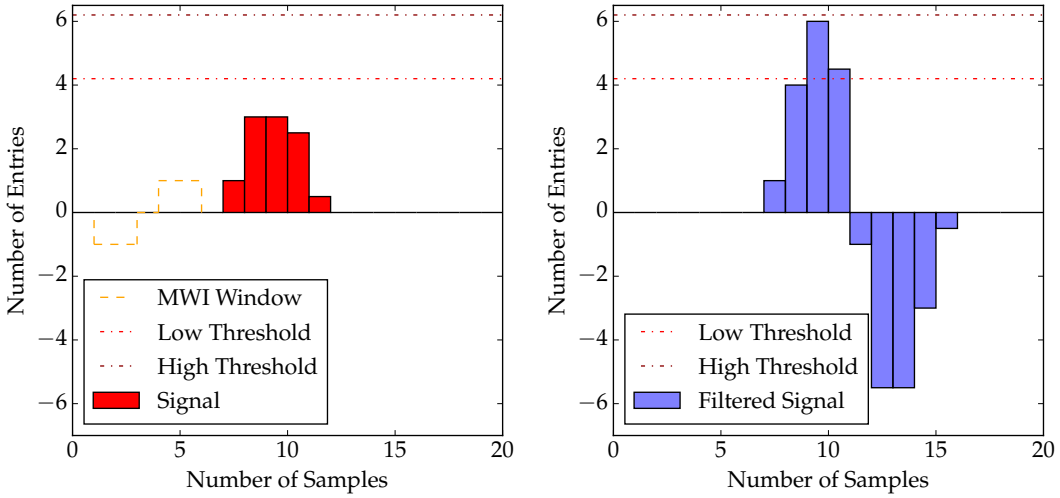

Figure 2.13 – *Schematic of the MWI. The plot on the left shows a pseudo signal with a MWI filter. The filter has a peak time of two samples and a gap time of one sample. All sample entries which lie within the peak-time are multiplied by the corresponding value of the MWI window* $(0, \pm 1)$ *and summed up to the new sample entries. The picture on the right hand side shows the filtered signal. The two red dashed-dotted lines represent the low and high threshold of the constant fraction discriminator.*

Lab amplifier saturates. The fast ditigtizer SIS3305 also records the amplified PMTs signals from the Detector Lab amplifier. This is the standard set-up of the MainzTPC DAQ. If the electronic read-out chain deviates from this setting for a particular measurement it is stated later in the description of the measurement.

For the activity measurement of the dosimetry branch the signal of the 1 inch PMT is first amplified with the KPH amplifier before its rate is recorded with the aid of a discriminator model 705 from Phillips Scientific [Phia] and a quad scalar model N1145 from the company CAEN [CAE06b].

2.3.3 *High voltage*

In order to power all eight APDs, the two PMTs of the TPC, its cathode and gate mesh as well as the dosimetry PMT four different power modules are used. They are listed below:

- The eight APDs and two PMTs of the TPC are powered with two 6-channel VME power supply modules, type V6533P from the manufacturer CEAN. This board has a output range of 4 kV and 3 mA with a maximum power consumption of 9 W. The output polarity is preset by CAEN and can be a mixture of positive and negative outputs [CAEb].

- The negative high voltage of the cathode mesh is supplied with a Bertan 225 model 30R from the manufacturer Spellman. It can provide voltages up to 30 kV and currents up to 0.5 mA and [Spe].

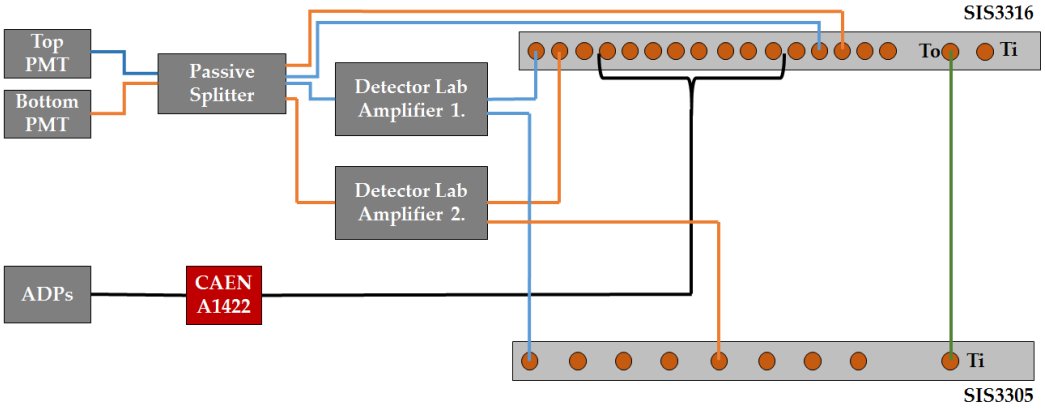

Figure 2.14 – *Schematic of the MainzTPC DAQ as used during this work. The passive splitter is a simple voltage divider made out of three 16.3 Ω resistors. The signal lines of the bottom and top PMT are colored in orange and blue correspondingly while the signal line of the APDs is colored in black. Since the SIS3316 generates the overall trigger of the DAQ its trigger output (To) has to be connected to the trigger input (Ti) of the SIS3305 board which is indicated here by the dark green line.*

- The gate mesh is powered with a NIM module of the type NHQ 206L from the company iseg Spezialelektronik GmbH. It has two channels each with a selectable polarity and a maximum voltage of 6 kV and a maximum current of 1 mA [ise01]. Also the anode mesh can be powered through this module with slightly positive voltages if required.

- The dosimetry PMT is powered also with a NIM module of the company iseg. The module of the type NHQ 234M provides voltages up to 3 kV and currents up to 4 mA [ise01].

While the V6533P VME boards and the Bertan 225 model 30R are controlled with a program similar to the MainzTPC DAQ program, the voltages of the gate mesh and of the dosimetry PMT are ramped up manually. For a further reading about the high voltage program the reader is referred to [Sisd].

2.3.4 *MainzTPC Raw Data Format and Analysis Framework*

In order to read-out and store the data of the MainzTPC DAQ a suitable data format was developed by Pierre Sissol in [Sisd]. The data format is organized in a three level hierarchical order providing a redundanc-free and extendable storage structure. The files are classified with different file header which provide the file identity, the stored data and its position in the hierarchical order. The highest hierarchy, the level 0 file header contains information which do not change during a single measurement, such as information about the used sensors (PMT, APD), or used boards (SIS3305, SIS3316). Just like each long-term run of the MainzTPC is subdivided into several separate measurements, each measurement is further subdivided into smaller acquisition periods. These periods are automatically organized by the MainzTPC DAQ program which

starts and stops a new acquisition cycle when certain criteria are fulfilled. This can be for example the maximum allowed file size of each acquisition period in order to store the measured data in regular time intervals and to keep the data size for FADC boards memory friendly. The information about each acquisition period like its start and end time as well as the number of acquired waveforms are stored in the lower hierarchical level 1 header files. The lowest level in the hierarchical order are represented through the level 2 header files. They contain the information about the actually recorded waveforms like their event-ID, channel-ID, triggerTime and the wavefrom data of the SIS3316 and SIS3305. All headers as well as the data itself are stored as binary files. For a more detailed description of the MainzTPC data format the reader is refereed to [Sisd].

Based on the MainzTPC DAQ data format a raw data analysis framework, which was written by Basitan Beskers in [Bes17], analysis each waveform of all recorded channels and translates its raw information into physical properties. The analysis framework is based on C++ and ROOT [CER]. It consists out of different analyzers which can be configured via XML files. Depending on the sensor type (PMT or APD) it applies two different analyzer types to the sampled waveforms which identify the recorded signals and peaks.

In order to analysis the waveforms measured with the bottom or top PMT the so-called XeRawPeakFinder is used. It filters each waveform by two so-called Moving Average Window (MAW) which work in principle like a MWI, but additionally it averages the return value of the filter by dividing the value with the length of the filter window. The weights and shape of the two MAWs are given by a raised cosine filter. The first MAW filter is applied to the entire waveform enhancing S_2 and suppressing S_1 signals. Afterwards the S_2-peaks are identified and tagged according to the criteria specified in the configuration XML file such as a minimum S_2 amplitude and width. Further are the S_2-peak properties like their positions, widths or sizes estimated and stored. Subsequent the algorithm filters all regions which were not tagged as a S_2-peak with a second MAW which highlights short signals, tags them as S_1-peaks according to the specified boundaries and also estimates and stores their properties. Three example raised cosine MAWs are shown in Figure **2.15**. The entire peak-finding antilogarithm is based on an algorithm of XeRawDP which is the analysis framework of XENON100.

Since the APDs are amplified with a charge sensitive preamplifier the information about the signal charge is stored in the recorded signal amplitude. The amplified APD signals are featured by a fast and steep rising edge followed by an exponential decay of the signal amplitude with a large decay time constant. Hence a second type of analyzer is used. It filters the recorded APD signals with another MAW. Hence the step-shaped APD signals are transformed into peaks which amplitude and position can be estimated easily. Beside storing the amplitude of the filtered waveform a fit function consisting out of a piece-wise defined linear function for the rising edge and a exponential decay for the falling edge is fitted to the data. The derived parameters of the fit function are stored also by the analyzer.

The last analyzer which was used during this work was a so-called fixed window integrater, which as its name suggest, integrates the samples within a fixed window of a wavefrom. This analyzer is required for the PMT calibration.

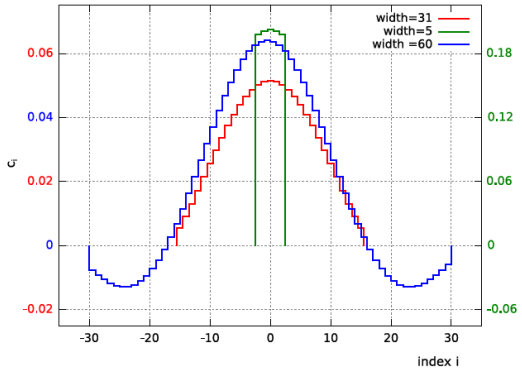

Figure **2.15** – *Raised cosine MAWs like used by the peak-finding algorithm of the MainzTPC raw data analyzers. The weights versus the samples of the MAW are plotted. The filter in green and red represents the S_1 and S_2 filter of the SIS3316 correspondingly and the blue MAW represents the S_1 filter of the SIS3305. The plot was taken from [Bes17].*

The data of all analyzers are stored in ROOT files using so-called TTrees. Each recorded and analyzed channel is represented through its own tree. The trees are then subdivided into several leaves which represent the different properties of the analyzed signals. In the case of the PMT data which are analyzed with XeRawPeakFinder the stored leaves are separated in S_1 and S_2 signals. Each leave contains an $(n \times m)$-dimensional array where n is the number of recorded waveform and m the number of S_1 or S_2 peaks within one waveform. Furthermore contains every TTree an n-dimensional array with unique event-IDs, one for each wavefrom [Bes17].

2.3.5 *Python Analysis Frame*

Due to its increasing usage in the XENON collaboration, one long-time goal for the MainzTPC is to change its analysis framework from ROOT and C++ into a Python based system featuring the Processor for Analyzing XENON (PAX) [XEN] which was developed for the XENON1T experiment. Joining this effort, also the analysis made during this work were done in Python using the standard package environment which PAX requires. However since the raw data analysis framework of the MainzTPC as discussed in Section 2.3.4 uses C++ and ROOT some adaptations had to be done in order to make the processed data easier to handle in Python.

In reference to PAX the Python package *pandas* [pan17] from which the so-called *DataFrames* were used to organize the data of the MainzTPC. DataFrames are a two dimensional array-like structure which allows to organize and manipulate hierarchically labeled data-sets. Moreover many tools of the pandas package are written in Cython[7] which enables a fast response and high performance. In order to read and write ROOT files with Python and pandas an additional package called root_pandas was used.

[7] Cython is a C-Extension for Python which allows to make use of the high performance of C and its libraries within Python.

Based on these two packages a function was written which is especially designed to read ROOT files produced by the MainzTPC raw data analyzer. This so-called RootReader returns a pandas DataFrame of all specified tree-leaves and event-IDs of a single ROOT tree. In a second step the read-in data is restructured in order to make use of the hierarchical structure of the DataFrames and the high performance of pandas. While the raw data analyzer of the MainzTPC stores the information of all peaks found in one waveform in a chronological ordered m-dimensional vector, the restructured DataFrame is sorted by the peak sizes. Furthermore an additional peak-ID allows to store the values as simple 32 bit floats in a hierarchically ordered multi-index DataFrame. This restructuring process is shown in Figure **2.16**. One drawback of the multi-index representation can be also seen in Figure **2.16**. Since the number of S_1 and S_2-peaks within one waveform is not necessarily the same empty slots are filled with the placeholder: not a number (NaN).

Figure **2.16** shows that this new structure allows a straight forward use of cuts. The column-wise representation of the different parameters makes it easy to apply certain threshold and selection cuts which masks the data with a bool-based array. Further, allows the peak-size sorted hierarchically structure of the new DataFrames a fast rejection of multi-scatter events by comparing only the S_2 area of the peak-Id 0 and 1 within the same event-Id.

Beside an more straight forward handling and better performance, the multi-index DataFrame also strongly reduces the amount of memory which is occupied by the data. A data-set of 850000 waveforms from a ^{133}Ba calibration measurement in the vector representation occupies 1.2 GB of memory while the multi-index representation requires only 107 MB which yields a compression of more than 90 %. This huge reduction comes from the fact, that the vectors of the ROOT files are stored as type "object" in Python which requires more memory than a simple 32 bit float. Also the multi-index pandas DataFrames can be stored as ROOT TTree files and further analyzed with ROOT if required.

Since so far the high level analysis of the MainzTPC data was done in ROOT and C++, also other small helper functions had to be written in order to get access to the data. One function for example is able to extract the bit-wise stored information from the header files of the MainzTPC data format. Another Python function reads the stored raw waveform data of an acquisition cycle which afterwards can be written into a XML file. This XML file is then used together with the Desktop Digital Detector Emulator from the manufacturer CAEN [CAE06a] to emulated recorded events and to adjust the MWI trigger from the SIS3316.

	nPeaksS1	miPositionS1	mfIntegralS1	nPeaksS2	miPositionS2	mfIntegralS2
evtId						
1024	1	[751]	[0.411489]	2	[1071, 3301]	[47.4113, 9.47812]
1025	2	[752, 1879]	[0.213392, 0.00145273]	1	[2079]	[53.9189]
1026	1	[752]	[0.465312]	1	[2360]	[62.6283]

		nPeaksS1	miPositionS1	mfIntegralS1	nPeaksS2	miPositionS2	mfIntegralS2
evtId	**peakId**						
1024	**0**	1.0	751.0	0.411489	2.0	1071.0	47.411316
	1	1.0	NaN	NaN	2.0	3301.0	9.478115
1025	**0**	2.0	752.0	0.213392	1.0	2079.0	53.918892
	1	2.0	1879.0	0.001453	1.0	NaN	NaN
1026	**0**	1.0	752.0	0.465312	1.0	2360.0	62.628342

Figure 2.16 – *Excerpts of two pandas DataFrames. The upper DataFrame shows the chronological vector representation of the MainzTPC data and the lower DataFrame the restructured multi-index representation which is sorted by the signal size. The excerpts were taken from a* ^{133}*Ba calibration measurement.*

CHAPTER 3

MEASUREMENTS

In the following the different measurement runs which were performed during this thesis are listed. The three main runs are building on each other and certain measures needed to be taken to account for different problems and issues. Hence in order to place everything into context and give the reader the necessary information to follow these decisions, the measurement runs are discussed in a chronological order.

In Section 3.1 the first measurement run is explained. It discusses the main goals of this run as well as the used tools, settings and measurements to achieve those. Section 3.2 deals with the October measurement which was designated to be the first ^{37}Ar run. However due to a new background contribution of small S_1 like events the ^{37}Ar measurement was postponed. Furthermore this section and its subsections deal with the origin of this background and the measures taken to correct this problem. The last section of this Chapter, Section 3.3, discusses the ^{37}Ar measurements and how the dosimetry of the ^{37}Ar sample was performed. The results of all measurements are presented afterwards in Chapter **4.**.

3.1 JULY RUN 2017

For a NR measurement induced by neutrons the entire MainzTPC experiment was shipped to the neutron time-of-flight facility nELBE of the Helmholtz-Zentrum in Dresden-Rossendorf. The measurement took place from November 2015 till Mai 2016. After this measurement campaign the experiment was again build up in the Mainz laboratory at the start of this thesis in Mai 2017. Therefore the July 2017 run was primarily a first test and a didactic-run in order to get the MainzTPC back to work. Further the run was used to achieve the following three main goals:

- The set-up of an high level analysis framework using Python which is described in Section 2.3.5.
- Setting up an energy calibration in the combined S_1 and S_2 space.
- Identify and set-up possible cuts for the ^{37}Ar run.

In addition to the measurements for this work also Compton scatter measurements were carried for the course of [Sisd].

In order to achieve the three mentioned goals two different calibration sources were used. One collimated ^{137}Cs source which decays with an half-life of 30.05(8) years and a probability of 94.36(28) % by the emission of β-particle with an endpoint energy of 513.97(17) keV into an excited state of ^{137}Ba. ^{137}Ba itself deexcites by the emission of a 661.659(3) keV γ-ray into its ground state. In the over 5.64(28) %, ^{137}Cs decays directly into the ground state of ^{137}Ba releasing its total Q-value of 1175, 63(17) keV by the emission of a β-particle [B$^+$11].

The used ^{137}Cs has an activity of 37 MBq and is mounted into a lead collimator. The collimator has a is fixed azimuthal position with respect to the center of MainzTPC and its height is adjustable. The collimator was designed in [Sch13].

The second source which was used is an uncollimated ^{133}Ba source with an activity of 6.78 kBq which was mounted to the outer dewar wall of the MainzTPC. It decays with a half-life of 10.539(6) a via EC into one of the many excited levels of ^{133}Cs. The decay has a total Q-value of 517.3(10) keV and its two main branches are decaying into the 437 keV level (85.4 %) and the 383 keV level (14.5 %) of ^{133}Cs. The two excited ^{133}Cs states deexcite via the emission of a chain of γ-rays or either directly into the ground state of ^{133}Cs. The for this work most important transitions of ^{133}Cs are the 276.3992(21) keV, 302.8512(16) keV, 356.0134(17) kev and 383.8491(12) keV transitions with a branching ratio of 7.53(6) %, 19.10(12) %, 63.63(20) % and 9.12(6) % correspondingly which includes already the EC branching ratio [B$^+$11]. The decay scheme of ^{133}Ba as well as the decay scheme of ^{137}Cs are shown together in Figure **3.1** on the right hand and left hand side respectively.

The calibration measurements of the July run were performed like in Figure **2.14** on page 49 sketched, except for the fact that the bottom PMT was amplified with the KPH amplifier instead. The trigger was generated by the SIS3316 using a coincidence between the unamplified signals of the bottom and top PMT. The MWI was configured with a peak-time of 8 samples, a gap-time of 4 samples and a trigger threshold of 250 FADC channels which corresponds in the 5 V dynamic range mode to 19.073 mV. This trigger setting was designated to trigger on the S_1 signals of a interactions. The ^{133}Ba and ^{137}Cs source were measured with a drift field of 200 V/cm and 800 V/cm respectively. Furthermore a pulsed blue light-emitting diode (LED) light for the PMT calibration was used.

3.2 OCTOBER RUN 2017 AND MAINZTPC MAINTENANCE NOVEMBER 2017

The October 2017 run was designated to be the first test run with an ^{37}Ar-sample. The main purpose of this run was it to learn how the ^{37}Ar dosing works. Further, it was not clear how long it takes to diffuse the ^{37}Ar into the LXe or if it diffuses into the LXe at all. This is also one of the main concerns about a usage of ^{37}Ar in the XENON1T experiment. Unfortunately this run was affected by a new kind of background which origin was unknown. This background is featured by small S_1 alike pulses which occur in various distributions. Some example waveforms containing

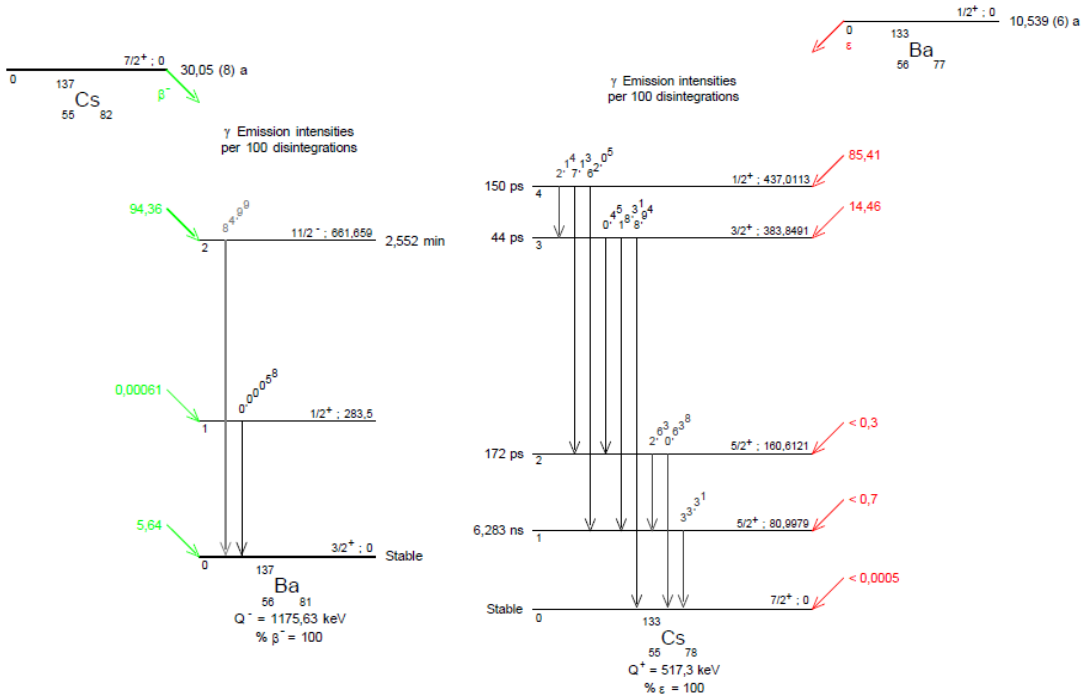

Figure 3.1 – *Decay schemes of the ^{137}Cs and ^{133}Ba decay. The schemes were taken from [B+11].*

these background events are shown in Figure 3.2.

As one can see in the first two rows of Figure 3.2 are the waveforms varyingly strong populated with these background events. While the first row shows a very clustered time distribution of the background events the waveform in the second row is completely covered. Furthermore it is shown that those events are not caused by the amplifier electronics since they occur in both the amplified and unamplified channel. The clusters of the background events are in the order of 1 µs which corresponds to the typical width of a S_2 signal in the MainzTPC. This leads to the conclusion, that the background events, or atleast a fraction of it, might be caused by single or a handful of electrons which are extracted by the extraction field. This hypothesis is further supported by the fact, that these background events only occurred in measurements in which the MainzTPC was operated with a drift and an extraction field. Hence it was assumed that the electrons might come from one of the two following sources:

1. Field emission from one of the meshes due to a broken mesh wire.

2. Impurities which emit electrons after the absorption of the VUV photon coming from the LXe scintillation.

In order to partially rule out the first hypothesis the background trigger rate of the MainzTPC was measured for a variety of different field settings. It was observed that a reversion of the drift field direction suppresses the occurrence of background events, even though that the relative voltage difference between the different meshes was the same. Hence one could at least conclude, that if field emissions are the origin

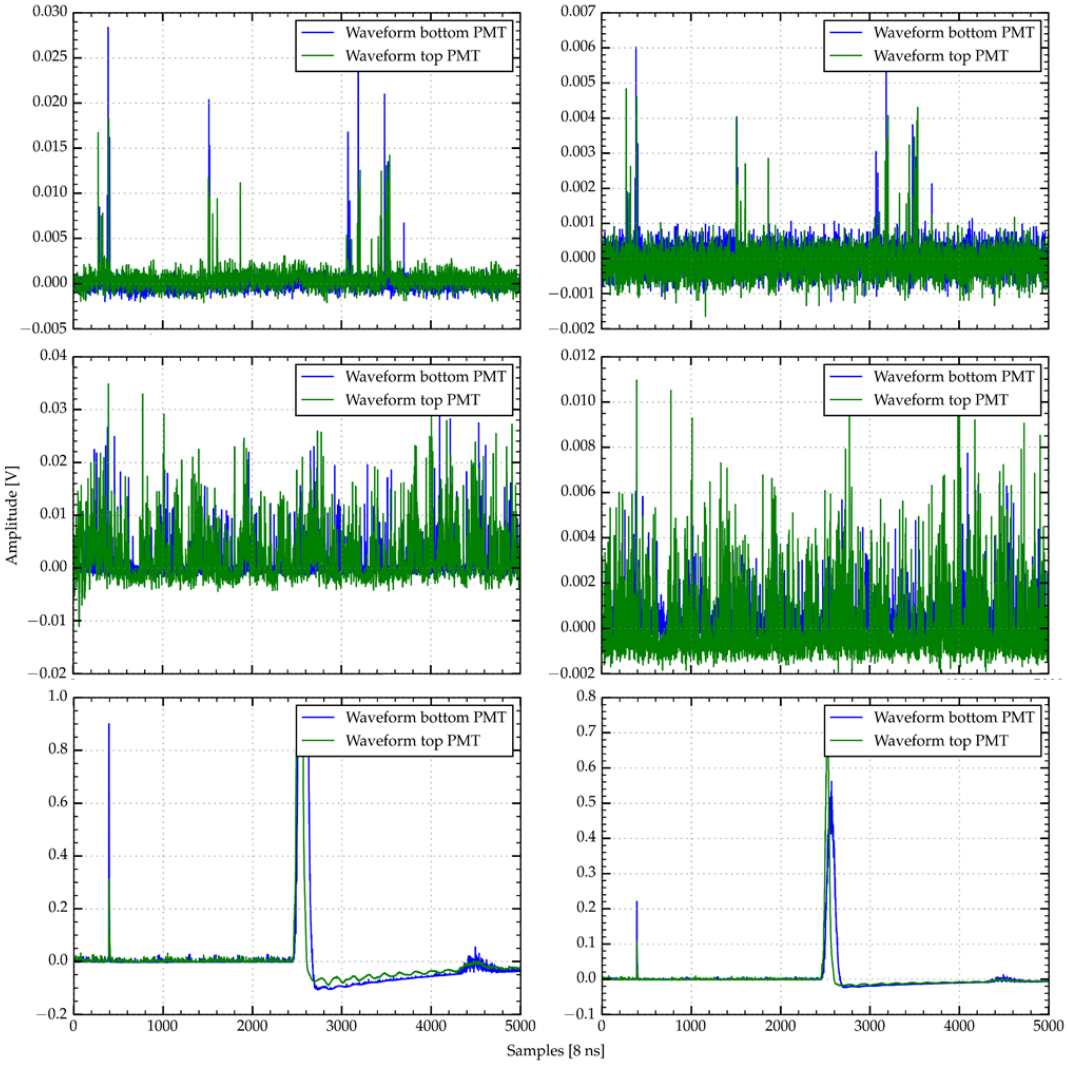

Figure 3.2 – *Background signals of the October 2017 run. The plots are representing three different waveforms of a ^{137}Cs calibration measured with the top and bottom PMT and a drift field of* 200 *V/cm. All plots are showing the signal amplitude versus the wavefrom sample. The plots on the left hand side are presenting the signals measured with the amplified channels while the right column shows the same wavefroms unamplified.*

of the electrons they did neither come from the gate nor the anode mesh. Furthermore was observed that these background events were not contributing to all wavefroms. During this run also many wavefroms were recorded which did not contain any of these background S_1 like pulses. All these observations make it more likely that a small amount of impurities caused these signals.

The last row of Figure 3.2 shows that the amplitudes of these background events are small compared to S_1 and S_2 pulses of a regular calibration source like ^{137}Cs. However their amplitudes are in the expected range ($\sim$ tens of mV) for the S_1 signals of ^{37}Ar. Hence any S_1 trigger would not work properly in this case. Since also many of the

recorded wavefroms did not contain any of the background events, different trigger settings were tried in order to suppress events which contain them.

In the first method it was tried to set-up a veto for the background signals. In order to do so the trigger of the DAQ was generated externally with the Phillips Scientific discriminator (Sec. 2.3.2) using its lowest possible threshold of 10 mV. The background event veto was generated with a shaping amplifier of the model 570 from the manufacturer Ortec [ORT] and the same discriminator. The shaping amplifier had the purpose to integrate the signal within a certain time window. Once the integrated signal exceeds the adjustable discriminator threshold, a veto signal is generated. The veto was tried for different shaping times of the amplifier and discriminator thresholds, but this approach did not lead to any satisfying result.

In the second approach it was tried to trigger on S_2 instead of S_1 signals. This would at least allow to trigger only on events which contain an S_2 signal and suppresses background only events. This was necessary since the background coincidence trigger rate of the top and bottom PMT for a S_1 signal based trigger was already around 4.5 kHz for measurements with a drift field. As comparison without drift field and the same trigger setting only rates about 45 Hz were measured. Triggering on S_2 signals can be achieved with the MWI and the internal trigger generation of the SIS3316. It is an interplay between the peak and gap time of the MWI as well as its low and high threshold. Nevertheless after some first trials it was decided not to measure the ^{37}Ar sample during this run since it was unclear if one could distinguish the S_1 signals of the ^{37}Ar from the background.

In the end the October run was used to measure additional ^{137}Cs spectra for a drift field of 200 V/cm and without any drift field for the case these background events would remain. The measurements were triggered externally with the phillips discriminator using a trigger threshold of 30 mV for both PMTs and a quad fold logic unit of the model 755 of the manufacturer Phillips Scientific [Phib] to generate the PMT coincidence. This threshold was well above of most of the background signals and was higher as during the July run. The rest of the read-out chain was like in Figure **2.14** sketched. In addition to the measurements the PMTs were again calibrated with pulsed blue LED.

3.2.1 *MainzTPC maintenance November 2017*

Since the hypothesis that the field emission could have caused the background events, was not ruled out for the cathode mesh, one consequence of the October run was the maintenance of the MainzTPC in November 2017. A maintenance of a dual-phase LXe detector cannot be performed in the normal laboratory environment, because of impurities like dust and other particles would harm the detector performance like its charge and scintillation yield. Therefore the whole MainzTPC was transported into a flow box of the PRISMA Detector Laboratory. For the inspection of the meshes the MainzTPC was partially dismounted. During this disassembly some small metallic dust-like particles were found on the glass window of the bottom PMT as well as on the cathode and gate mesh. These particles could have caused the field emissions inside the MainzTPC. In addition also some white PTFE-like particles were found.

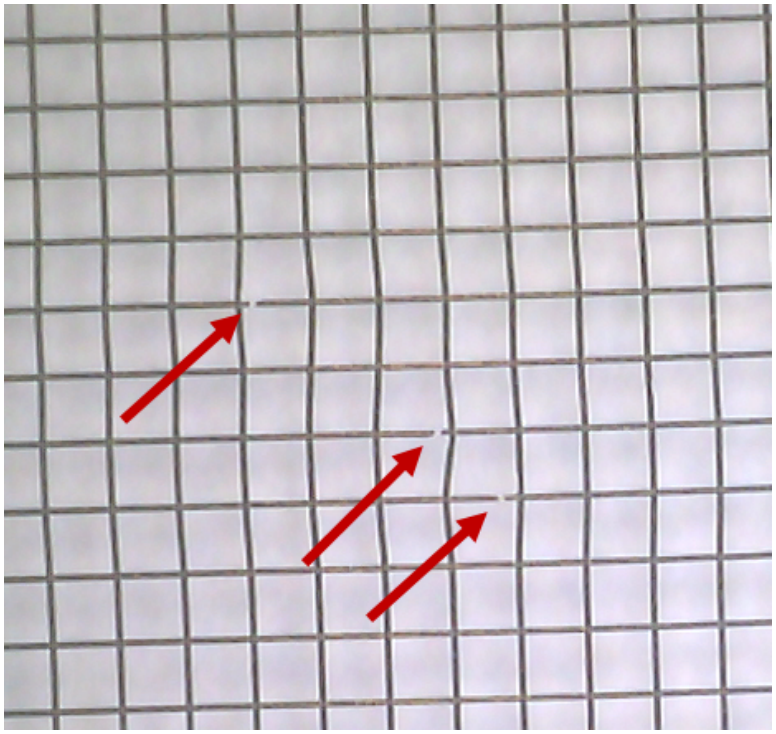

Figure 3.3 – *Picture of the magnified cathode mesh. Presented is the cathode mesh magnified with the USB magnifier of the PRISMA Detector Lab. The red arrows point towards some broken mesh wires. The shown mesh was replaced with with the spare one. As reminder the pitch of the meshes is 268 µm and the wire diameter 14 µm.*

The origin of the metallic as well as the PTFE particles is unclear. Most likely they are remnants of the construction phase of the MainzTPC. All meshes were cleaned with dry nitrogen and a ultra-sonic bath which was filed with pure water and isopropyl. Afterwards they were inspected through a USB magnifier from the PRISMA Detector Lab. During this inspections it was found, that all meshes had atleast a single broken wire. A picture of the magnified cathode mesh is shown in Figure 3.3. It shows three broken wires and the resulting deformation of the mesh structure. The cathode mesh was replaced with a spare one.

Beside the inspection of the meshes also other smaller task which were accumulated in the time before the October run were fixed during the maintenance. The broken glass fibers were successfully replaced and the spillway for the liquid level adjustment was exchanged by the new one presented in Figure 2.6 on page 37 in order to improve the stability of the liquid level. A comparison between the old and new spillway is quantitatively given in Section 4.7. Due to the time constraints of this work, the functionality of the glass fibers were just tested qualitatively. It was possible to illuminated all eight APDs properly, but no further gain calibration of the sensors were performed.

3.2.2 *Gas-system January 2018*

The second attempt to measure the ^{37}Ar sample was in January 2018. Initially it was planned to repeat the calibration measurements of the July and October run due to some discrepancies between those two runs (see Section 4.1 and Section 4.3). However during the preparation for the January run a large contamination through impurities inside the gas-system was found.

Since the different mechanical parts as well as the cables of the detector are constantly out gassing the whole experiment has to be pumped before each run. Afterwards the set-up is flushed with about 2 bar of gaseous xenon which is recirculated through the hot zirconium getter of the gas-system. This approach pre-cleans the detector from electronegative impurities and ensures a better performance. However during the xenon recirculation in January 2018 it was noticed, that the inlet pressure of the getter measured at A-P2[1] increased by 180 mbar within 14 h. This indicated a degeneracy of the zirconium cartridge of the getter. Since these zirconium cartidges are not cheap and the time was short, it was luckily decided to replace the whole getter with a second one from a different gas-system. During the exchange of the getter it was noticed by chance, that the pressure rise was caused by a clogging of the prefliter of the getter which is mounted in front of its zirconium cartridge. This clogging was caused by a black particle dust coming from the diaphragm of the KNF double-diaphragm pump (A-MP). It covered the inner walls of all pipes of the gas-system which were in front of the getter. This black dust is shown in the upper photographs of Figure **3.4**. The diaphragm of the KNF pump started to brittle as a result of its attrition. After this incident the gas-system was completely dismounted, cleaned, reassembled and backed. Further the two diaphragms of the KNF-pump as well as its sealings were replaced with new ones. Beside the black dust, it was noticed that the old and brittle diaphragm had also a small hole in it. This hole might finally explain the background events of the October 2017 run. Small fraction of oxygen and nitrogen might have diffused through this little hole into the detector and caused the background events. As a comparison both, the old and new diaphragm are shown in the lower picture of Figure **3.4** as well. The clogging of the getter pre-filter was fixed b blowing natural argon gas in the reverse direction through it.

The direct consequence of this incident was the assembly of an additional particle filter (A-F1) directly after the pump. After consulting the group of Professor Weinheimer of the University of Münster which had also a similar problem in the past, they suggested a particle filter with a pore size of 2 µm. For the MainzTPC gas-system a sintered filter of the manufacturer Swagelok [Swa] with a pore size of 2 µm and a nominal flow rate of 65 slpm for an inlet pressure of 1 bar was used.

[1] See the schematic of the gas-system Figure **2.9** on page 41.

Figure 3.4 – *Photographs of the black dust which was seceded from the inner diaphragm of the KNF double-diaphragm recirculation pump The upper two pictures are showing the black dust which was found everywhere in the gas-system. The lower picture is a comparison of a new diaphragm with the old worn one. The red circle indicates the position where the worn diaphragm broke.*

3.3 MARCH RUN 2018

The March 2018 run led finally to the opening of the ^{37}Ar sample. This run had the goal to answer the following three main questions.

1. Can we estimated the activity of the ^{37}Ar sample properly ?
2. How fast and well diffuses ^{37}Ar inside liquid xenon?
3. Furthermore does it distribute homogeneously?

These questions are of importance for a planned use of ^{37}Ar as a calibration source for XENON1T. In order to answer these questions different measurements with the MainzTPC and the dosimetry branch were performed. In Section 3.3.1 the dosimetry measurement of the ^{37}Ar sample is described. Furthermore this section describes different calibration measurements which were performed in order to be able to estimate the activity of the ^{37}Ar sample. Subsequent Section 3.3.2 deals with a description of

the measurement procedure during and after the injection of the ^{37}Ar into the recirculation system and the MainzTPC.

3.3.1 *Preparation of the dosimetry branch and the ^{37}Ar dosing*

In order to prepare the dosimetry procedure for the ^{37}Ar sample, the different volumes of the dosimetry branch had to be measured and the 1 inch PMT for the activity measurement had to be calibrated. For the calibration purpose the T-volume (D-PMT[2]) was dismounted and one of the CF-40 to 1/4 inch adapter was replaced with a glass fiber feed-through. The other end of the T-volume was sealed with VCR face seal fitting. A small fiber was mounted to the inner side of the feed-through which was guided into the PTFE measurement chamber shown in Figure **2.11** on page 43. Through this glass fiber the PMT was illuminated with a blue LED light which was driven by a pulse generator. This approach allowed to illuminate the PMT only indirectly since the shape of the PTFE measurement chamber did not allow a safe bending of the glass fiber. The PMT signals were amplified by one of the Detector Lab amplifiers and recorded with the SIS3316. The second output of the amplifier was feed into the Phillips Scientific discriminator whose logic output was recorded by the SIS3316 as well. The single photo-electron calibration measurement was performed for different discriminator threshold settings in order to find a suitable threshold for the ^{37}Ar dosimetry during the run.

After the PMT calibration the T-volume was mounted back to the gas-system in order to perform the volume measurement. Due to the complex shape of the individual dosimetry branch components, their volume were measured through the mass integration of gaseous nitrogen which was filled into the dosimetry branch. Therefore a liquid nitrogen dewar was mounted to the free port next to the valve B-V7[3]. The gaseous nitrogen was filled through the flowcontroller A-FC until all parts were filled with 2.4 bar of nitrogen. The same approach was also chosen to determine the total volume of the MainzTPC and its infrastructure.

The ^{37}Ar dosimetry itself was performed during the March 2018 run. Since the measurement was originally scheduled for January 2018 the quartz ampule containing the ^{37}Ar sample had been irradiated already on the 19th December 2017. The irradiation was performed as described in Section 2.2.2, leading to an estimated initial activity of (238 ± 62) kBq. The ampule itself was opened on the 8th March 2018 with an remaining activity of (49 ± 12) kBq calculated by the decay law and Gaussian error propagation. The error of the decay time as well as the error of the past time between the 19.12.2017 and the 08.03.2018 were neglected in this calculation. For the actual activity measurement the dosimetry PMT was powered with its maximal allowed bias voltage of 900 V and read-out with the KPH amplifier. The amplified signal was fed into the Phillips Scientific discriminator which threshold was set to 20 mV. Afterwards the pulses of the logic output of the discriminator were counted with the CAEN quad scalar. The scalar was used manually and set to 5 min counting periods. The results of

[2] See Figure **2.10** on page 42
[3] See Figure **2.9** on page 41

the PMT calibration, the volume estimation and the ^{37}Ar dosimetry are discussed in Section 4.6.1.

3.3.2 *^{37}Ar measurement*

One goal of the ^{37}Ar measurements was, to find out how well the ^{37}Ar mixes and distributes in the liquid xenon of the MainzTPC. Therefore ^{37}Ar was injected from the dosimetry branch into the recirculation circuit of the TPC and the gas-system two times. However during the March 2018 run the connection of the drift field cage of the MainzTPC broke and led to a distorted and unusable drift field. As a consequence all measurements were carried out without drift field, i.e. only the S_1 signals of the ^{37}Ar decays were measured. Since they were expected to be in the order of 5.6 pe (see very end of Section 4.3), it was decided not to use a coincidence between the top and bottom PMT. This would cause an artificial trigger threshold, because an interaction in gaseous xenon has a higher light collection efficiency for the top PMT, while interactions in liquid xenon are more prominent on the bottom PMT in a dual-phase TPC. This effect is also reflected by the so-called "area fraction top"-parameter which is explained in more detail in Section 4.4.

The measurements for each ^{37}Ar injection was divided into two phases. In the first phase the DAQ was triggered by the top PMT since due to the piping and the xenon recirculation it was expected that the ^{37}Ar distributes first in the gas-phase of the TPC. It was also expected that the distribution process will happen on a short time scale once the the calibration gas is injected and the recirculation is restarted. In the second phase the trigger of the DAQ is switched to the bottom PMT in order to increase the trigger efficiency for small events which occur in the liquid xenon. Before any ^{37}Ar was injected into the MainzTPC two background measurements were taken for each trigger setting.

In both cases the trigger was generated with the MWI of the SIS3316. Compared to the July measurement a slightly different trigger setting had to be used. This was necessary because the DAQ was triggered very often by a bipolar noise coming from the PTR when using the trigger setting of the July run. This bipolar noise is presented in Figure **3.5**. As a consequence the peak time of the MWI was increased to 20 samples (160 ns) and the gap time reduced to 2 samples (16 ns). With this setting the resulting amplitude of the bipolar noise got suppressed since the size of the integration window is in the same order as its period. The trigger threshold had to be increase to 550 FADC channels which represents a threshold of 41.96 mV in the 5 V range setting.

Since it was unclear how long the diffusion of the ^{37}Ar into the liquid xenon would need, each top PMT triggered measurement was taken for 1.5 h before the trigger setting was changed. Furthermore each top PMT triggered measurement started before the ^{37}Ar injection was performed. The results of the ^{37}Ar measurement is presented in Section 4.6.2.

Figure 3.5 – *Oscilloscope screenshot of the bipolar PTR noise. The green channels presents the signal output of the amplified top PMT.*

CHAPTER 4

RESULTS

In the following chapter the results of the different measurements are discussed. The first Section 4.1 deals with the calibration of the bottom and top PMT of the MainzTPC as well as the read-out electronics. Section 4.2 introduces and discusses possible data quality cuts for the ^{37}Ar measurement. The subsequent section deals with the energy calibration of the MainzTPC based on the measurements with the ^{137}Cs and ^{133}Ba calibration source. Further a first prediction for the position of the 2.8 keV transition of ^{37}Ar is given. Afterwards Section 4.4 deals with the z-position reconstruction. It discusses the drift times and velocities for a given field. Furthermore a calibration of the drift field for the so-called area fraction top parameter is given which allows to measure the z-distribution during the ^{37}Ar measurement in the absence of a drift field during this measurement. Section 4.5 deals with the xy-position reconstruction based on a weighted average method with the eight APDs. It discusses qualitatively the xy-position reconstruction and xy-distribution of the measurements with the ^{137}Cs and ^{133}Ba source. The following Section 4.6 is subdivided into two subsections and both dealing with the ^{37}Ar measurements of the March 2018 run. The Subsection 4.6.1 discusses the calibration of the dosimetry PMT as well as the volume measurement of the dosimetry branch and the MainzTPC experiment based on the dry nitrogen mass integration method. Moreover it discusses the measured activity of the ^{37}Ar sample and how the dosing procedure worked. Subsection 4.6.2 addresses the important questions of an usage of the ^{37}Ar as a calibration source in the XENON1T experiment. It presents the corresponding S_1 total spectrum and deals with the z-distribution of the ^{37}Ar inside the MainzTPC. Additionally the time evolution of the ^{37}Ar concentration inside the MainzTPC and the question about how fast ^{37}Ar diffuses into liquid xenon are discussed. Section 4.7 deals with a quantitative study of the liquid level fluctuation experienced with the MainzTPC. It introduces two simple fit models for the fluctuations and gives a comparison between the new and old spillway based on one of these models.

4.1 PMT CALIBRATION

Since the energy deposit of a particle interaction is proportional to the initially produced number scintillation photons and ionizations, it is necessary to convert the measured PMT charge into the corresponding number of photo-electrons. This allows to compare different measurements with the same detector independently of the used read-out electronics of each measurement. In order to estimate the amount of charge which corresponds to a single photo-electron the top and bottom PMT of the MainzTPC were calibrated after each run. Therefore the PMTs were illuminated by a blue LED light which was driven by a pulse generator. The used voltage-pulse had a small width of about 10 ns and its amplitude was adjusted such that only in 5 % of all cases a PMT signal was measured. This is motivated by the fact that the measured number of photo-electrons is following Poisson statistics and hence the probability of having more than a single photo-electron electron signal is given by

$$P(\lambda = 0.05, n > 1) = 1 - (P(\lambda = 0.05, n = 0) - P(\lambda = 0.05, n = 1)) \approx 0.121\,\% \quad (4.1)$$

where $P(\lambda, n)$ represents the Poisson distribution for a given mean value λ evaluated at the number n. Hence this approach ensures that the contribution of multiple photo-electron signals is negligible.

In each calibration measurement 500000 voltage pulses were measured. This ensures a statistically significant population of the single photo-electron peak. Afterwards every waveform was integrated in a fixed window around the expected PMT signal position, whether a PMT signal is present or not. Subsequently the resulting charge spectrum was fitted by the following model

$$\begin{aligned} f(x) =& N'(A_{\mathrm{pe}}, \mu_{\mathrm{pe}}, \sigma^2_{\mathrm{pe}}) + \\ &+ \left(N'(A_{\mathrm{spe}}, \mu_{\mathrm{spe}}, \sigma^2_{\mathrm{spe}}) + N'(A_{\mathrm{dpe}}, 2 \cdot \mu_{\mathrm{spe}}, 2 \cdot \sigma^2_{\mathrm{spe}}) \right) \cdot \Theta(n = 0)\,, \end{aligned} \quad (4.2)$$

where $\Theta(n = 0)$ represents the Heaviside step function and

$$N'(A, \mu, \sigma^2) = A \cdot \exp\left(- \frac{(x - \mu)^2}{2 \cdot \sigma^2} \right) \quad (4.3)$$

a not normalized variation of standard normal distribution $N(\mu, \sigma^2)$, with A_{i} as the amplitude of the pedestal ($i = \mathrm{pe}$), the single photo-electron ($i = \mathrm{spe}$) and double photo-electron ($i = \mathrm{dpe}$) peak; μ_{i} and σ_{i} the mean value and standard deviation of the pedestal and single photo-electron peak respectively. Further the fit model in equation (4.2) uses the prior knowledge of $X(\mu_1, \sigma_1^2) + Y(\mu_2, \sigma_2^2) = Z(\mu_1 + \mu_2, \sigma_1^2 + \sigma_2^2)$ in order to express the mean value and standard deviation of the double photo-electron in terms of the single photo-electron peak. An example fit is presented in Figure 4.1 for the calibration of the bottom PMT after the October run. The other fits can be found in the Appendix C. in the Figures 5.5, 5.6 and 5.7 on page 117 and following.

The estimated values for the mean and standard deviation of the single photo-

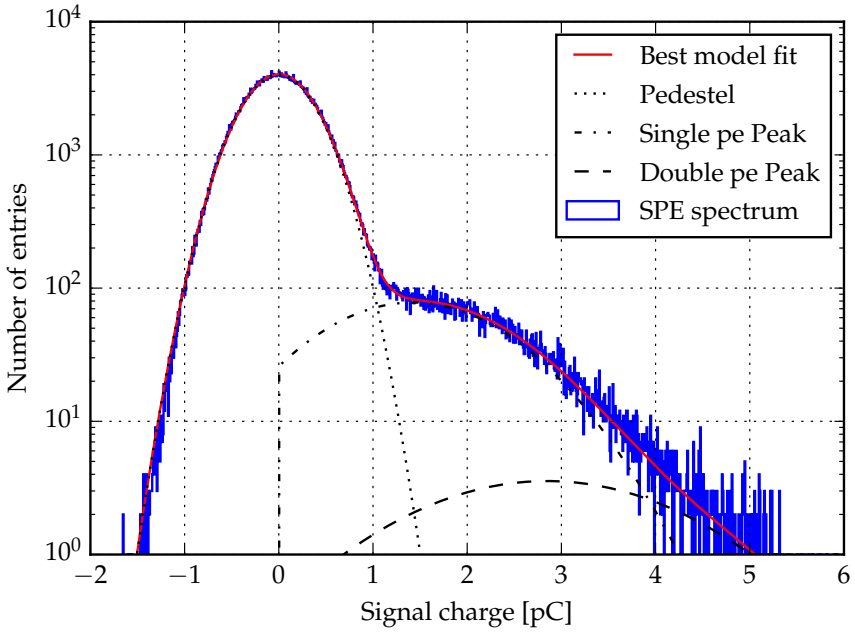

Figure 4.1 – *Single photo-electron spectrum with the corresponding fit model. The number of entries versus the integrated signal charge for the amplified bottom are plotted for PMT calibration of the October 2017 run. The spectrum was fitted according to equation (4.2). The individual contribution of the pedestal as well as the single and double photo-electron peak are also shown.*

electron charge as well as the gain of the amplifier which were used during the corresponding runs are reported in Table 4.1. Since the single photo-electron spectrum of the top PMT in the July run is affected by an additional noise contribution the fit model in equation (4.2) was extended with another normal distribution $N'(A_{\text{noise}}, \mu_{\text{noise}}, \sigma_{\text{noise}})$ in order to model it. However this fit model did not represent the measured spectrum properly as it can be seen in Figure 5.5. Hence the mean value and standard deviation of the single photo-electron measured in [Bes17] was used instead. Also the calibration spectrum of the bottom PMT from the March 2018 run is affected by an additional noise component. This noise was modeled through an additional exponential function $A \cdot \exp(-m \cdot x)$ in the second term of equation (4.2). A more detailed table about the different fits can be found in the Appendix C. on page 116.

The amplifier gains were calculated by a linear fit model without offset which was applied to the amplitudes of amplified and unamplified S_1 signals of one measurement in each run. The gain difference of the Detector Lab amplifiers in the October 2017 and March 2018 run comes from a different output termination. While the amplifier gain of the October run corresponds to the correct $50\,\Omega$ termination, it was changed back for the March 2018 run in order to have the higher gain at the cost of possible signal reflections.

The unamplified values the single photo-electron did charge vary between the different measurement runs. This also has an affect of the measured energy spectra like one can see in the following section.

Table 4.1 – *Table of the single photo-electron charges and amplifier gains for the three measurement runs. The voltage number in the brackets behind the PMT labels represents the used bias voltage during the measurement. All values except for the mean value and standard deviation of the top PMT of the July run are estimated as explained in the text. The values for the top PMT of the July run were take from [Bes17]. The upper block represents the values for the amplified signals, the lower block the values without amplification. The uncertainties of the unamplified values were calculated according to the Gaussian error propagation.*

Run	PMT	μ_{spe} [pC]	σ_{spe} [pC]	amplifier gain
July	Top (1000 V)	2.735 ± 0.032	2.52 ± 0.02	10.3493 ± 0.0005
	Bottom (950 V)	0.991 ± 0.020	0.76 ± 0.014	4.4351 ± 0.0001
October	Top (1000 V)	1.86 ± 0.014	0.900 ± 0.013	3.4061 ± 0.0001
	Bottom (1000 V)	1.423 ± 0.032	0.900 ± 0.013	4.9727 ± 0.0002
March	Top (1000 V)	4.149 ± 0.036	3.037 ± 0.039	10.8393 ± 0.0003
	Bottom (1000 V)	3.195 ± 0.158	2.177 ± 0.079	10.6053 ± 0.0023
July	Top (1000 V)	0.2642 ± 0.0031	0.2435 ± 0.0019	–
	Bottom (950 V)	0.2234 ± 0.0045	0.1713 ± 0.0032	–
October	Top (1000 V)	0.5455 ± 0.0040	0.2642 ± 0.0038	–
	Bottom (1000 V)	0.2861 ± 0.0064	0.1809 ± 0.0026	–
March	Top (1000 V)	0.3828 ± 0.0032	0.2802 ± 0.0049	–
	Bottom (1000 V)	0.3013 ± 0.0149	0.3013 ± 0.0109	–

4.2 QUALITY CUTS FOR THE MAINZTPC

Before a new and unknown calibration sample like ^{37}Ar can be studied, one needs to understand and study more common calibration sources in order to compare their results and to conclude expectations for the new and unknown sample. Therefore the MainzTPC was calibrated with a collimated ^{137}Cs and an uncollimated ^{133}Ba source during the July and October run. The features and parameters of their S_1 and S_2 signals were studied in order to apply quality cuts to the data. In the end four different cuts were used:

- A **coincidence cut** for S_1 and S_2 signals in order to discard random noise events.
- A **single S_2** (per waveform) cut which suppresses multi-scatter events
- A **S_1 width** cut which removes accidentally wrong labeled peaks.
- A **drift time cut** to discard events coming from unfeasible regions.

The highest level cut is the **coincidence cut**. It requires that every waveform contains atleast one S_1 signal and one S_2 signal. Further it requires that the left edges[1] of the S_1 signals measured by the bottom and top PMT lies within a coincidence window of 96 ns. The same holds for the S_2 signals. The long coincidence window was chosen

[1] The left edge is defined as the left position were the signal amplitude drops to 10 % of the amplitude maximum.

Table 4.2 – *Table of the lower (LB) and upper boundary (UB) for the S_1 width estimated based on the highest density region method. The values were derived from the S_1 width spectra presented in Figure 4.2. The numbers in the round brackets are the drift fields of the individual measurements. The first two measurements were performed during the October run, while the last two measurements were taken during the July run.*

Measurement	PMT	LB [ns]	UB [ns]	Coverage α
^{137}Cs (0 V/cm)	Top	200	464	0.832
	Bottom	240	520	0.846
^{137}Cs (200 V/cm)	Top	104	184	0.815
	Bottom	112	184	0.848
^{137}Cs (800 V/cm)	Top	80	168	0.824
	Bottom	176	248	0.848
^{133}Ba (200 V/cm)	Top	88	160	0.811
	Bottom	184	240	0.784

since the decay time of the LXe scintillation is in the order of 20 ns and hence for small signals such as expected for ^{37}Ar may only occur in a delayed coincidence. If multiple S_1 or S_2 coincidences were found within a single waveform (due to after pulses for example) only the coincidence with the highest signal charge were selected.

After this coincidence cut the number of S_2 signal per waveform were restricted to be exact one. This **single S_2** cut ensures that all multi-scatter events are discarded. First of all S_1 signals of a multi-scatter event are overlapping which worsens for example the efficiency of the S_1 width cut. Further, since the scintillation yield of liquid xenon does not scale linearly with energy multi-scatter events would worsen the overall energy resolution of the detector.

The third cut which was applied to the data is a **S_1 width cut**. The approach of this cut is presented in Figure 4.2. The upper plot shows that the recorded S_1 low width[2] is following an asymmetric distribution. Hence in order to determine a boundary interval for the S_1 width cut the method of the highest density region was chosen. This method yields for an asymmetric distribution also asymmetric boundaries for a given coverage α. For a discrete distribution whose bin entries are monotonically decreasing with distance from the highest bin entry, the highest density region can be calculated by simply going from the highest bin on both sides outwards until the desired coverage is reached. For the S_1 low width measured with the MainzTPC a coverage of $\alpha = 0.85$ was chosen. Since the binning of the low width is rather coarse due to the 8 ns sampling of the SIS3316 the chosen confidence intervals represent an upper boundary rather than an exact coverage. The lower and upper bounds for the S_1 width, as well as their real coverage based on the spectra shown in Figure 4.2 are presented in Table 4.2.

From the plots in Figure 4.2 and the values presented in Table 4.2 it becomes clear that the S_1 width depends only on the presence of a drift field not its field strength, at least for the measured field strengths. For the zero field measurement the broader S_1 width distribution comes from delayed recombination of the created electrons with

[2] Low width means signal width at an amplitude of 10 %.

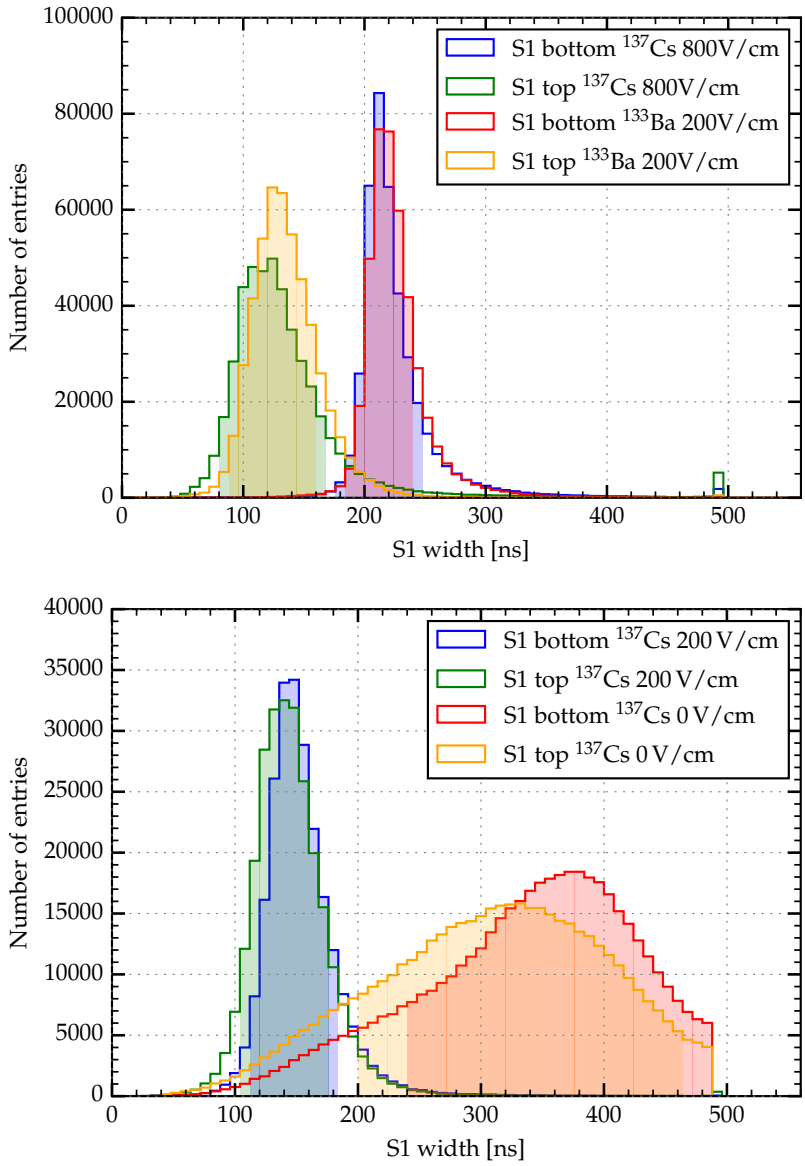

Figure 4.2 – *S_1 width distribution measured with the top and bottom PMT for different field settings. The number of entries versus the low width of the S_1 (width at 10 % of the S_1 amplitude) are plotted. The colored shaded areas are indicating a ∼85 % coverage of the distribution which represents the S_1 width cut. The spectra presented in the upper plot were measured during the July 2017 run while the lower picture shows two measurements of the October 2017 run. The presented data was selected according to the coincidence and single S_2 cut.*

xenon ions and the therefore delayed emission of scintillation photons. Further the S_1 width measured with the top and bottom PMT in the July run populates two well separated distributions while they overlap in the October measurement. This is due to the read-out electronics and the PMT bias voltage. In the July run the bottom PMT was operated with a bias voltage of 950 V and the KPH amplifier, whereas the top

PMT was biased with 1000 V and amplified with the Detector Lab amplifier. In the October run both PMTs were read out with a Detector Lab amplifier and biased with 1000 V. The S_1 width cut was applied to each measurement according to the upper and lower boundaries stated in Table **4.2**.

The last cut applied to the data (if a drift field was applied during the measurement) was a **drift time cut**. It simply cuts away all events which have a drift time exceeding the maximal expected drift time for a given field. The drift field cut as well as the z-position reconstruction is explained in more detail in Section 4.4. A to the z-position corresponding xy-position cut was not used since only a qualitatively analysis of the APD data was possible. A detailed explanation about this circumstance is given in Section 4.5.

Additional cuts based on features of the S_2 signals were not used. This was due to the fact that the S_2 signal were affected by a saturation for large signals. This saturation effect is shown in the two plots of Figure **4.3**. The upper plot shows that the area of the S_2 signal starts to saturate at an signal amplitude of 0.5 V. In the lower plot of Figure **4.3**, it is shown that the signal width starts to decrease in the same voltage range. Since on the other hand the S_2 signal amplitude is not affected by saturation this leads to the conclusion that the saturation is caused by the limited amount of charge carriers coming from the last dynode of the PMT and its base. Hence it is necessary to increase the number of available charge carriers if one want to measure larger S_2 signals with the MainzTPC. This can be achieved by substituting the capacities C5, C4 and C3 of the PMT base shown in Figure **2.3** on page 33 with higher once. A further study of the PMT base saturation was carried out by the bachelor research assistant David Maksimovic and an exchange student from Italy Mohamed Abdelbaset. Their analysis is still on going and hence for this work the information of large S_2 signal were not used. Hence the only S_2 information which were used during the analysis of the spectra are the position of the S_2 signals and therefore the drift time between S_1 and S_2 as well as the number of S_2 signals within a single waveform in order to discard multi-scatter events.

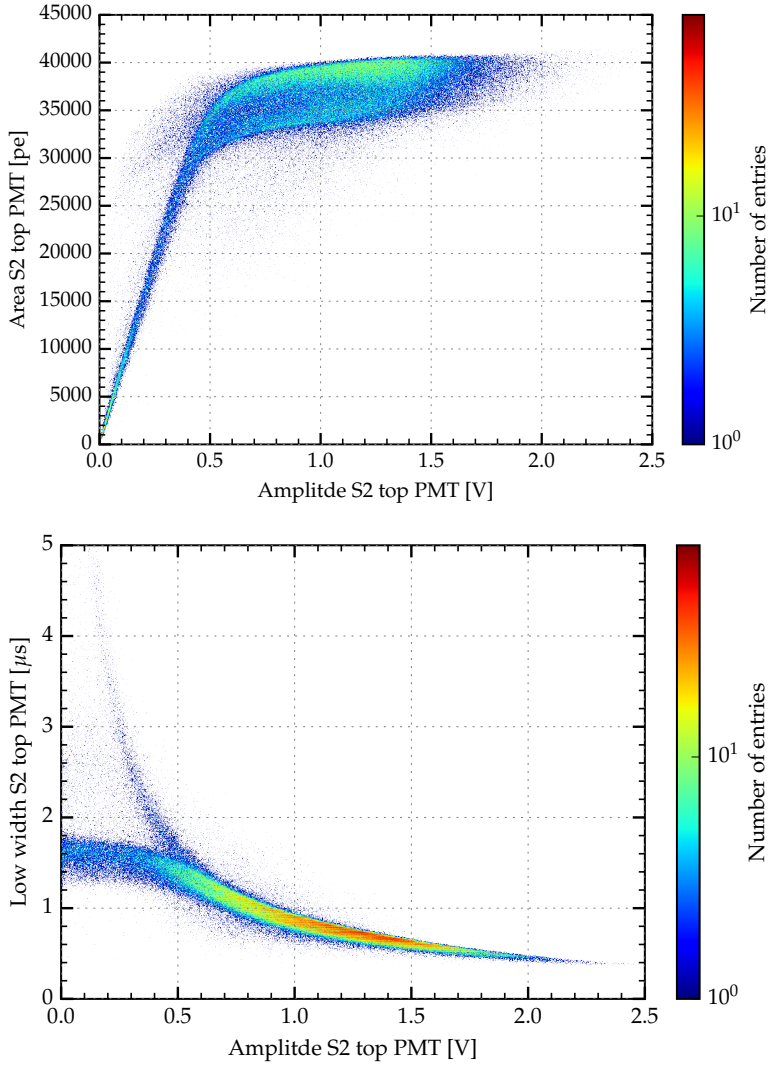

Figure 4.3 – *S_2 signal saturation measured with a ^{133}Ba source and a drift field of 200 V/cm from the July 2017 run. The signals were measured by the unamplified channel of the top PMT. The upper plot shows the area of the S_2 signals versus their amplitudes. The lower picture shows the S_2 low-width (at the 10 % level of the amplitude) versus the measured amplitude. The colorcode is in a logarithmic scale.*

4.3 S_1 SIGNAL ENERGY CALIBRATION

In order to calculate the S_1 energy spectra of the different sources the measured S_1 peak areas of the top and bottom PMT were first converted into a signal charge and subsequently, according to the data of the single photo-electron calibration stated in Table 4.1, into the number of photo-electrons. Further the total S_1 signal charge (the summed area of the bottom and top PMT) is used for the measurement of the energy spectra. The S_1 total energy spectra for the different sources are shown in Figure 4.4 and Figure 4.5 for measurements with and without drift fields respectively. The ^{137}Cs

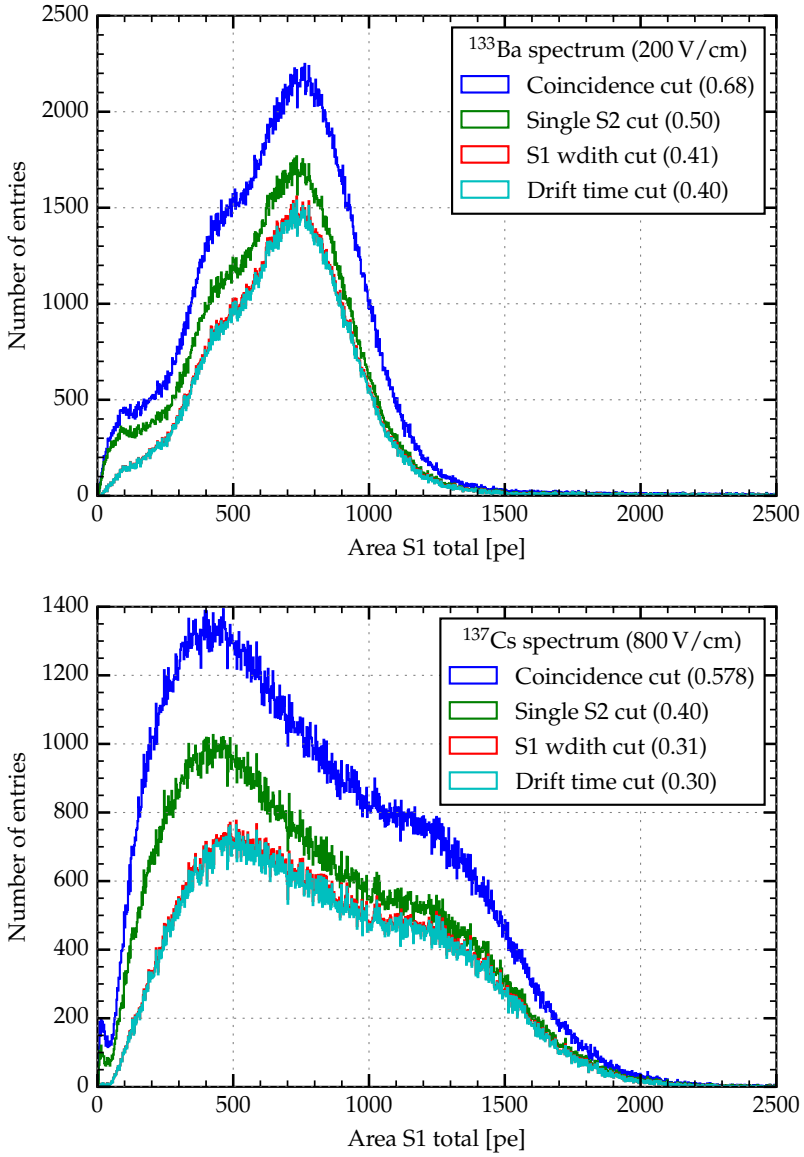

Figure 4.4 – *S_1-total energy spectrum for the uncollimated ^{133}Ba and the collimated ^{137}Cs source for a drift field of 200 V/cm and 800 V/cm correspondingly, measured during the July 2017 run. The number of entries versus the total S_1 charge in photo-electrons are plotted. The different colored spectra represent the same spectrum with an accumulated number of quality cuts like stated in the plot legends. The numbers in the round brackets corresponds to the fraction of the remaining number of events compared to the initially recorded number of events. For the ^{133}Ba spectrum a total number of 842890 and for the ^{137}Cs spectrum a total number of 998114 waveforms were recorded. The cuts itself are explained in Section 4.2.*

spectrum measured at a drift field of 200 V/cm can be found in Figure 5.8 in the Appendix C. on page 120.

The double peak structure of the ^{133}Ba spectrum in the upper plot of Figure 4.4 is

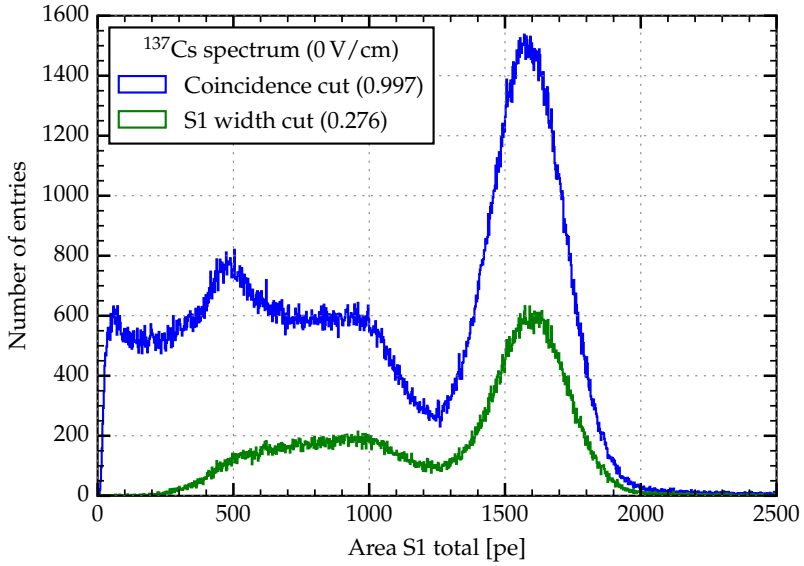

Figure 4.5 – *S_1-total energy spectrum for the collimated ^{137}Cs source without a drift field. The spectrum was measured during the October 2017 run. Initially a total number of 494016 events were recorded.*

caused by the superposition of the four transitions mentioned in Section 3.1. The S_1 energy resolution of the detector is not good enough to separate the four transitions. While the discussed cuts preserve the double peak structure, especially small signals of the lower end of the ^{133}Ba spectrum are suppressed. In particular the S_1 width cut reduces the number of entries in this region. For the ^{137}Cs spectrum in the lower plot of Figure 4.4 the same behavior can be observed. The full-energy-peak of ^{137}Cs is only indicated as a shoulder on the right side of the Compton regime. Comparing the relative height of the Compton region and the full-energy-peak for the coincidence and drift time cut spectrum shows that full-energy-peak gets enhanced by a factor of 1.2 due to the cuts. Hence the cuts seem to work properly. While the ^{137}Cs spectrum in Figure 4.4 shows the full-energy-peak only as a shoulder overlapping with the Compton regime, the spectrum is much more clear for the measurement without field. The spectrum in Figure 4.5 shows a well separated full-energy-peak and Compton edge. Further around 500 pe one can see most likely the back-scatter-peak of ^{137}Cs. In this case the S_1 width cut is not necessarily a benefit. The cut may preserve the Compton edge and the full-energy-peak of the spectrum, but however it suppresses the hypothetical back-scatter-peak.

In order to quantify if the alleged back-scatter-peak is actually the back-scatter-peak of the ^{137}Cs spectrum, the three feature of the spectrum were fitted. The back-scatter-peak and the full-energy-peak were fitted with a normal distribution in addition with a linear background:

$$f(x) = N'(A, \mu, \sigma^2) + m \cdot x + b \tag{4.4}$$

where $N'(A, \mu, \sigma^2)$ presents the normal distribution (see equ. (4.3)), m the slope of the linear background and b the offset of the linear background model. The Compton edge can be described as a sharp edge which gets smeared out due to doppler broadening.

Hence it can be modeled as a convolution of a normal distribution with a Heaviside step function which results in

$$\begin{aligned}(N'(A,\mu,\sigma) * \Theta'(n=0))(x) &= \int_{-\infty}^{+\infty} N'(\tau;A,\mu,\sigma)\cdot\Theta'(x-\tau;n=0)\,\mathrm{d}\tau \\ &= \frac{A}{2}\left(1-\mathrm{erf}\left(\frac{x-\mu}{\sqrt{2}\sigma}\right)\right) \end{aligned} \tag{4.5}$$

where $\Theta'(n=0) = 1-\Theta(n=0)$ and erf is the cumulative distribution function of a normal distribution, the so-called error function. Further an additional linear background was added. Hence the fit function of the Compton edge is described by

$$f(x) = \frac{A}{2}\left(1-\mathrm{erf}\left(\frac{x-\mu}{\sqrt{2}\sigma}\right)\right) + m\cdot x + b\,. \tag{4.6}$$

The corresponding energies of the Compton edge E_{CE} and back-scatter-peak E_{BSP} can be calculated according to

$$E_{\mathrm{CE}} = E_{\mathrm{FEP}} - E_{\gamma'}(\theta=\pi) \tag{4.7}$$

$$E_{\mathrm{BSP}} = E_{\gamma'}(\theta=\pi) \tag{4.8}$$

with the energy of the full-energy-peak E_{FEP} and Compton's formula

$$E_{\gamma'} = \frac{E_\gamma}{1+\left(\frac{E_\gamma}{m_\mathrm{e}}\right)\cdot\left(1-\cos(\theta)\right)} \tag{4.9}$$

in the energy representation, where E_γ is the energy of the impinging γ-ray, $E_{\gamma'}$ the energy of the scattered γ-ray, m_e the electron mass and θ the scatter angle. The full-energy-peaks of the ^{137}Cs spectra which were measured with a drift field were also fitted according to equation (4.4). Due to the superpositioned double peak structure of ^{133}Ba the spectrum was fitted with two normal distributions in addition to a linear background. For the spectra with drift field the fits were applied to the full-energy-peaks of the drift time cut spectra. In the case of the ^{137}Cs spectrum without any drift field the back-scatter-peak, Compton edge and full-energy-peak fits were applied to the coincidence cut spectrum. The fits for the ^{133}Ba spectrum and zero drift field ^{137}Cs spectrum can be found in Figure **4.6**. The other fits for the ^{137}Cs spectra with drift field can be found in the Appendix C. in Figure **5.9** on page 121.

The derived mean values and standard deviations of the different fits can be found in Table **4.3** together with the corresponding energy values, together with the χ^2/ndof-values of the individual fits. They show that the different features of the spectra are described well by the used fit models. Since the ^{133}Ba spectrum is a superposition of four peaks it is hard to judge which energies the two resulting peaks correspond to. For this analysis it was assumed that the second peak (P2) belongs to the energy of the 356.0134(17) keV transition, while the smaller peak (P1) is a composition of the 276.3992(21) keV and 302.8512(16) keV transitions. Hence a weighted average with

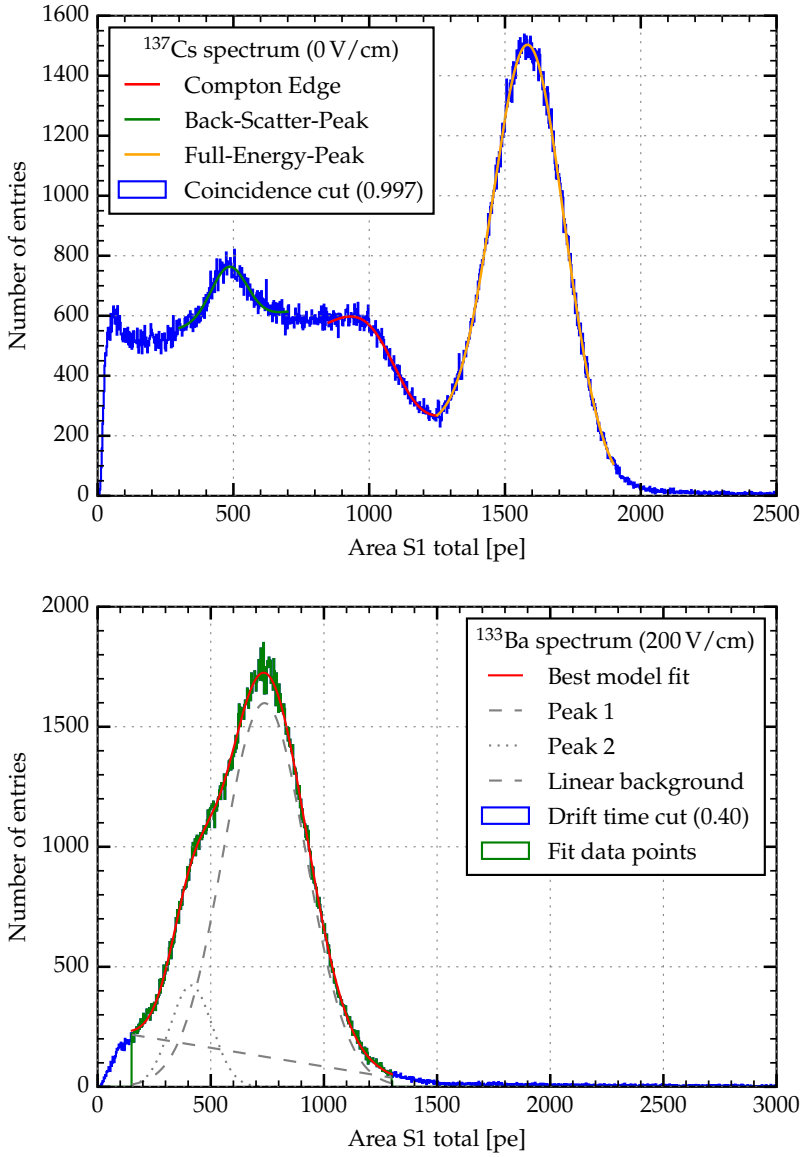

Figure 4.6 – *Example fits of the back-scatter-peak, the Compton edge and full-energy-peak for the ^{137}Cs S_1-total spectrum measured without a drift field and the double peak of the ^{133}Ba spectrum measured at a drift field of 200 V/cm. For the ^{133}Ba double peak also the individual fit components are plotted.*

their branching ratios as weight was used in order to determine the energy of the lower peak. In order to compare the derived values with each other one can assume a linear relation between scintillation yield and energy as a first order approximation, since the energy difference between the two peaks is small. However comparing the ratio of the mean values of the two peaks $413.35/737.39 = 0.561$ and their energies $295.37/356.01 = 0.830$ shows a mismatch.

Figure 4.5 shows a good agreement of the derived positions of the full-energy-peak, back-scatter-peak and the Compton edge with the expected positions. Assuming a

Table **4.3** – *Table of the mean values and standard deviations for the different fits of the S_1-total energy spectra. The used abbreviations stand for full-energy-peak (FEP), back-scatter-peak (BSP), Compton edge (CE), Peak 1 (P1) and Peak 2 (P2). The energies of the Compton edge and back-scatter-peak were calculated according to equations (4.8) and (4.7). The energies of the ^{133}Ba peaks were estimated as explained in the text.*

Source	Drift field	μ [pe]	σ [pe]	χ^2/ndof	Energy [keV]
^{137}Cs-FEP	0 V/cm	1586.19 ± 5.20	131.42 ± 0.75	262/255	661.659(3)
^{137}Cs-BSP	0 V/cm	483.43 ± 2.47	66.04 ± 3.24	175/155	184.272
^{137}Cs-CE	0 V/cm	1092.53 ± 2.83	91.27 ± 12.79	131.93/155	476.728
^{137}Cs-FEP	200 V/cm	962.17 ± 15.31	200.89 ± 17.13	267/235	661.659(3)
^{137}Cs-FEP	800 V/cm	1141.79 ± 5.25	329.46 ± 5.56	578.77/395	661.659(3)
^{133}Ba-P1	200 V/cm	413.35 ± 2.17	91.94 ± 2.20	443/376	295.37
^{133}Ba-P2	200 V/cm	737.39 ± 1.35	183.52 ± 1.10	"	356.0134(17)

linear relation between energy and scintillation yield one would assume that the position of the back-scatter-peak has its mean at 442.30 pe which is 9 % off of the measured value. However one has to take into account that the absolute scintillation yield is not the same for those two energies as presented in Figure **1.5** on page 13. The actual scintillation yield of LXe at the energy of the back-scatter-peak is actually 5 % higher than for the full-energy-peak of ^{137}Cs. Taking further the derived standard deviation into account, it shows that the alleged back-scatter-peak is indeed the back-scatter-peak of ^{137}Cs. The same holds true for the Compton edge.

However although this comparison works properly, comparing the position of the full-energy-peaks for the ^{137}Cs measurements at the different drift fields show a discrepancy. While from theory a decrease of the scintillation yield for an increasing drift field is expected, the opposite is observed in the data. Calculating the relative scintillation yields according to the full-energy-peak positions of ^{137}Cs for the two drift fields yields $962.17/1586.19 = 0.60$ and $1141.79/1586.19 = 0.72$ for the 200 V/cm and 800 V/cm drift field respectively. Both values are in contradiction with the expectations according to Figure **1.6** on page 14. This conflict in the data can be explained either through a wrong PMT calibration since the three spectra were taken in two different runs, or that the drift field is not working properly. Latter can be ruled out by the Z-position reconstruction presented in the following Section 4.4. Furthermore the first hypothesis is in agreement with the observations of the unamplified single photo-electron charges stated in Table **4.1** on page 68. The estimated single photo-electron charge of the top PMT in the October measurement is nearly doubled compared to the values derived for the July and March run. However this would only explain the deviation of 800 V/cm drift field measurement, since the other two measurements with the 200 V/cm drift field and the measurement without drift field were taken during the October run. One last explanation could be given by the impurities which also most likely caused the background events in the October run. Impurities would degenerate the scintillation yield of the LXe which would lead to a decreased number of photo-electrons. However it is hard to judge if the concentration of impurities was high enough to degenerate the LXe scintillation. To study this one requires the knowl-

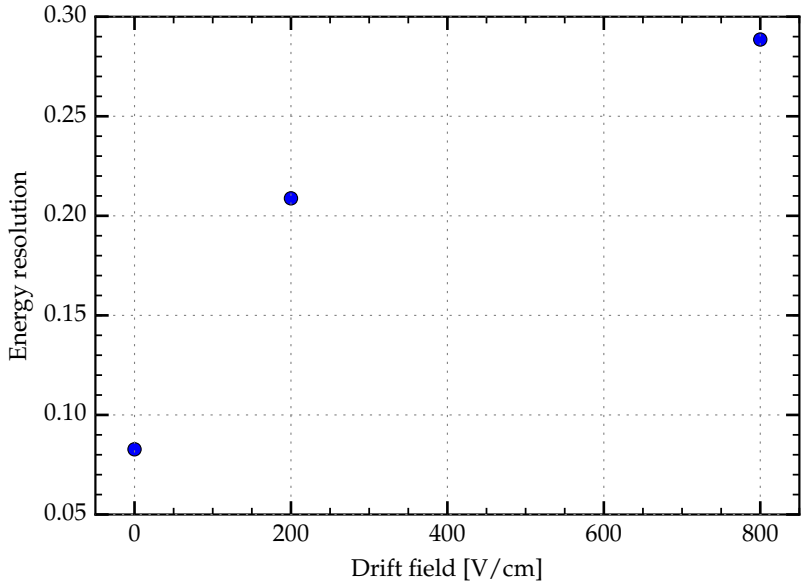

Figure 4.7 – *Energy resolution of the ^{137}Cs full-energy-peaks, measured at various drift fields. Plotted is the energy resolution given by σ/μ of the estimated fit values presented in Table 4.3.*

edge of the full-energy-peak position in the S_2 space, since impurities are affecting the charge yield more than the scintillation yield. Due to the signal saturation for large S_2 signals this study was not possible.

One last thing which can be studied with the S_1 calibration data is the energy resolution of the detector in the S_1 space. The energy resolution was calculated by σ/μ for the full-energy-peaks of ^{137}Cs measured with the three different drift fields. The result is shown in Figure 4.7. It reflects quantitatively the observations of the S_1-total spectra presented in Figure 4.4 and Figure 4.5; as well as in Figure 5.8 on page 120. The highest resolution and most detailed spectrum is achieved for the measurement without fields. The resolution becomes worse for higher drift fields, which reflects the fact that the Compton continue and full-energy-peak of S_1 total spectrum for the 800 V/cm measurement presented in Figure 4.4 overlap, while for the measurement at 200 V/cm as shown in Figure 5.8 that the two features are still separated. Additionally the back-scatter-peak of the 0 V/cm ^{137}Cs measurement yields an energy resolution of $\sigma_{\mathrm{BSP}}/\mu_{\mathrm{BSP}} = (0.14 \pm 0.01)$.

Since the ^{37}Ar measurements were carried out without drift field due to the broken field cage, one can set-up a first rough estimate for the expected photo-electron range for the 2.8 keV shell transition based on the full-energy-peak of the ^{137}Cs spectrum. Taking also the lowered absolute scintillation yield for the 2.8 keV transition into account (see Figure 1.5 on page 13) in addition to the fact that most of the energy is emitted by Auger electrons one can calculated the expected signal to be in the range of

$$\frac{\mu_{\mathrm{FEP}}}{E_{\mathrm{FEP}}} \cdot 2.8\,\mathrm{keV} \cdot \frac{47\,\mathrm{pe/keV}}{60\,\mathrm{pe/keV}} = 5.1\,\mathrm{pe}\,,$$

which is in agreement with the observed signal presented in Section 4.6.2.

4.4 Z-POSITION RECONSTRUCTION

In order to determine the z-coordinate of an interaction each liquid noble gas dual-phase TPC uses a homogeneous drift field which allows to reconstruct the depth of the interaction by the drift time between a S_1 and S_2 signal. For measurements with any gaseous calibration source this allows to estimate how well a gas mixes with the LXe and how fast it diffuses into it. Further the drift time can be used to apply additional quality cuts to the data.

Since the ^{37}Ar measurement was carried out without drift field due to the broken field cage, the measurement with the uncollimated ^{133}Ba source was used to calibrate the drift time with respect to the so-called area fraction top. The "area fraction top" parameter is calculated in general through the ratio of the signal area measured with the top PMT divided by the total signal area

$$\text{"Area fraction top"} = \frac{S_x^{top}}{S_x^{top} + S_x^{bot}}, \tag{4.10}$$

where S_x stands either for S_1 or S_2. Since in most of the cases multiple S_1 and S_2 signals are found within one waveform the peaks were selected according to the coincidence cut which is discussed in Section 4.2. The drift time was calculated by subtracting the left edge position of a S_1 signal by the left edge position of a S_2 signal, leading to negative drift times. The drift time versus the area fraction top of the ^{133}Ba and ^{137}Cs measurement from the July run are shown together in Figure **4.8**.

In both plots of Figure **4.8** one can clearly see a upper and lower bound of the drift time, which comes from the position of the cathode and gate mesh. These bounds were also taken for the drift time cut mentioned in Section 4.2. For the uncollimated ^{133}Ba source which was measured at a drift field of 200 V/cm a maximum drift time of $(32.5 \pm 0.2)\,\mu s$ was measured. For the ^{137}Cs measurement with a drift field of 800 V/cm a drift time of $(27.0 \pm 0.2)\,\mu s$ was found. These drift times correspond to a drift velocity of $50.5\,mm/32.5\,\mu s = (1.56 \pm 0.02) \cdot 10^5\,cm/s$ and $50.5\,mm/27.0\,\mu s = (1.87 \pm 0.02) \cdot 10^5\,cm/s$ respectively, which is in agreement with the plot shown in Figure **1.7** on page 15. The uncertainties of the drift velocity were calculated according to Gaussian error propagation and a distance uncertainty estimated to 0.5 mm which corespondents to the thickness of a single mesh holding frame.

The fact that the area fraction top is below 0.5 even for very small drift times can be explained by total reflection of the scintillation light at the xenon liquid-gas interface. According to Snell's law total reflection already occurs for an incident angle of 36 °, for a refraction index for gaseous of 1.0007 [ABMJ81] and liquid xenon of 1.69 [S+03].

The lower plot of Figure **4.8** also shows that the collimated ^{137}Cs source was positioned slightly to deep, since its z-distribution got cut off at the lower end. This circumstance was corrected for the October measurement, like one can see in Figure **5.10** of the Appendix C on page 122. In addition to this height adjustment Figure **5.10** shows that the area fraction top is shifted towards a higher fractions for the October

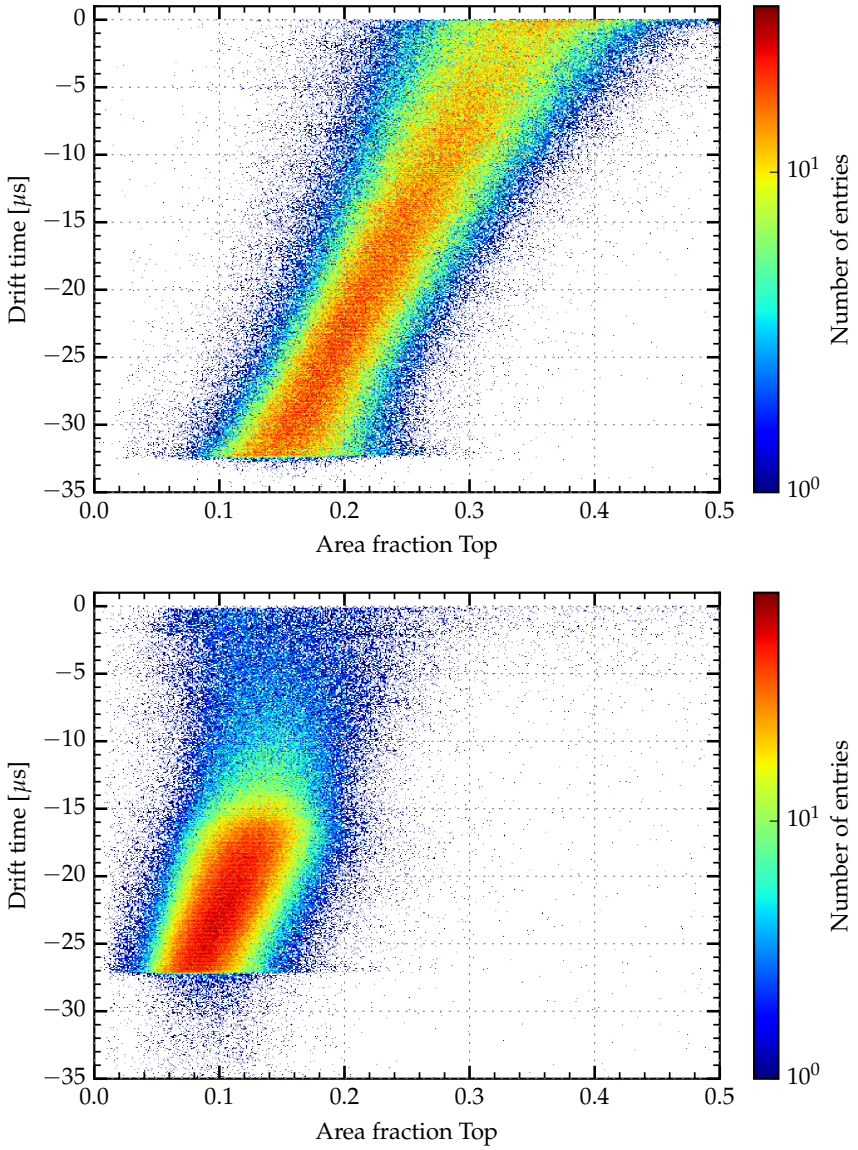

Figure 4.8 – *Area fraction top versus the drift time of the uncollimated ^{133}Ba (upper plot) and collimated ^{137}Cs (lower plot) measurements. The measurements were taken during the July run with a drift field of 200 V/cm and 800 V/cm respectively. The colorscale is logarithmic.*

measurements. This is another hint that the discrepancies between the S_1-total spectra in Section 4.3 of the October and July run might be caused by a wrong single photo-electron calibration of the PMTs.

Nevertheless in order to perform the drift time calibration for the area fraction top parameter the ^{133}Ba drift time versus area fraction top scatter plot presented in the upper picture of Figure 4.8 was vertically sliced into 1.5 µs slices starting at 1 µs. From the corresponding drift time slices the mean values and the error of the mean were calculated. The drift time slices can be found in the Appendix C. in Figure 5.11 on

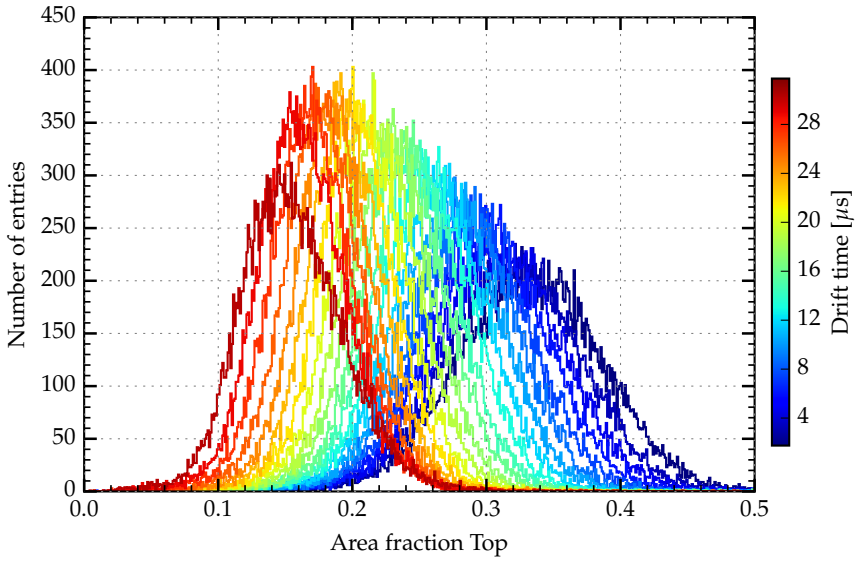

Figure **4.9** – *Area fraction top spectra for the different drift time slices. The area fraction top spectra of all 1.5 µs drift time slices are plotted. The colorcode represents the corresponding drift time.*

page 122. The related area fraction top slices are presented in Figure **4.9**. Each slice was fitted with a normal distribution $N'(A, \mu, \sigma^2)$ which is described in equation (4.3). The mean values of the drift time slices are plotted versus the corresponding mean values of the area fraction top slice fits in Figure **4.10**. The derived values were fitted with a linear function which yield a slope of $m = (219.57 \pm 2.26)$ µs, an offset of $b = (-54.00 \pm 0.39)$ µs and a χ^2/ndof of 15.9/19.

Beside an alternative representation of the drift time the drift time versus area fraction top parameter space can also be used for an additional quality cut. But, due to the missing drift field during the ^{37}Ar measurement this was not investigated any further.

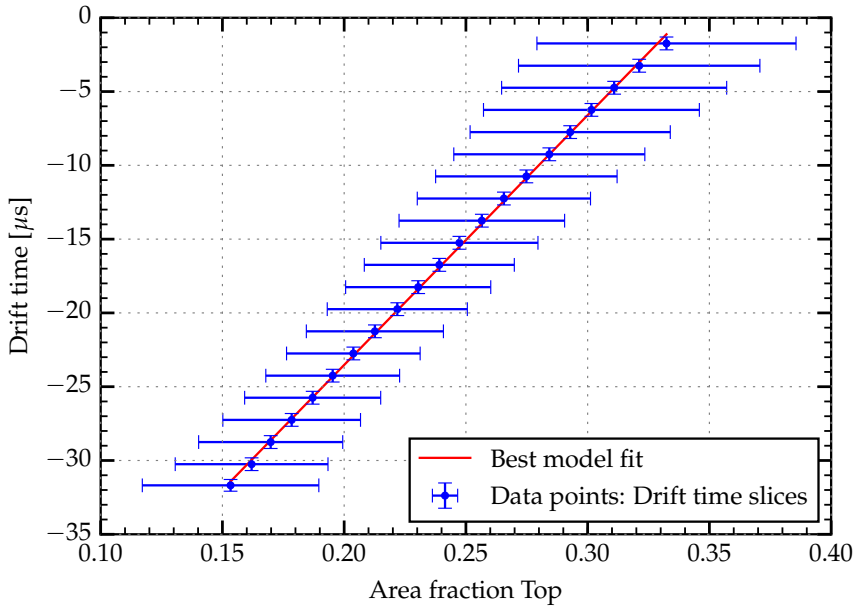

Figure 4.10 – *Drift time versus area fraction top calibration curve according to the 1.5 µs slices presented in Figure 4.9 and Figure 5.11. The errorbars of the drift time represents the error of the mean of each drift time slice, while the area fraction top errorbars represents the standard deviations of the area fraction top slice fits.*

4.5 APD XY-POSITION RECONSTRUCTION

Beside the drift time between S_1 and S_2 for the z-position the MainzTPC uses eight APDs to obtain the xy-position and thus to achieve a full three dimensional position reconstruction of an event in the TPC. Two different methods are currently under study for the xy-position reconstruction. The first method uses Geant4 to generate a so-called light-map for the eight APDs which is later used to reconstruct the xy-position for a given S_2 via a χ^2 minimization. This method is still under study and not fully working yet. Hence a second and more easier approach is used in the meanwhile. This second method uses a weighted average as approach which is also sometimes referred as center-of-gravity method. The xy-position of any S_2 signal $(\tilde{x}, \tilde{y})^\top$ is then given by

$$(\tilde{x}, \tilde{y})^\top = \frac{\sum_{i=1}^{8} w_i \, A_i \cdot (x_i, y_i)^\top}{\sum_{i=1}^{8} w_i} \quad \text{with} \quad w_i = \frac{qe_i}{g_i} \tag{4.11}$$

where A_i is the measured signal charge of the ith-APD, $(x_i, y_i)^\top$ the position of the ith-APD and w_i its applied weight. The weights itself are given by the relative or absolute Q.E. qe_i and the gain of the ith-APD. One drawback of this method is that it returns already by construction only a distorted picture of the reality, which becomes worse as the distance from the TPC center increases. Hence this method only represents a alternative solution until the first mentioned method is working.

Since the gain of APD 8 could not be estimated in the past, the initial position re-

Table 4.4 – *Table of the APD bias voltages, the corresponding relative gains and the applied weights for the Q.E.. The relative gains were measured in [Sisd], except for APD 8 which was arbitrary set to 150. The Q.E. weight 1 and 2 are representing the relative weights which were applied for the position reconstruction like for example shown in Figure 4.14. The Q.E. weight 2 values were set arbitrarily, like explained in the text.*

APD	bias voltage [V]	relative gain g_i	Q.E. weight 1	Q.E. weight 2
1	1500	122.34	1	1.00
2	1500	145.35	1	1.50
3	1500	93.33	1	1.91
4	1500	112.34	0	0.84
5	1500	268.909	1	2.1
6	1500	148.904	1	1.62
7	1500	101.645	1	0.75
8	1540	150	0	1.62

construction was done without APD 8 and APD 4 which represents its counter weight. The gain of APD 8 was not determined since two of the four glass fibers which are used for the sensor calibration were broken. Further information about the APD calibration can be found in [Sisd]. Beside the exception of APD 4 and 8, also the Q.E. values of all eight APDs are unknown and hence were assumed to be equal. The bias voltages and the corresponding relative APD gains as well as the used values for the Q.E. are shown together in Table 4.4. The result of this approach is shown in Figure 4.11.

Although, this approach is only returning a even more distorted image due to the taken out APDs and the missing Q.E. weights, one can already see that the majority of the collimated ^{137}Cs decay-reaction beam is interacting within the first half of the MainzTPC. This is also the reason why one cannot use the full-energy-peak of ^{137}Cs in order to determine the relative Q.E. value of all eight APDs. This can be only achieved with a homogeneous distributed *in situ* calibration source like ^{37}Ar. The corresponding ^{137}Cs energy-spectra measured with the APDs 3,4,6 and 7 are shown in Figure 4.12. As one can see, a determination of the relative Q.E. value with a localized source is not possible. While the signals of APDs 6 and 7, which are closest to the interaction side of the collimated ^{137}Cs source, exceed the dynamic range of the SIS3316 and do not show any full-energy peak; the signals of APDs 3 and 4 are less enhanced. Their measured energy-spectra are showing both a small peak around 0.01 V (APD 4) and 0.004 V (APD 3) which is most likely the full-energy peak of ^{137}Cs. This hypothesis is justified through their enhancement after an event selection based on the full-energy peak shown in the lower plot of Figure 4.4 of Section 4.3 was performed. All four recorded energy-spectra have a peak at the very right edge of their spectrum in common. This peak is artificially caused by the dynamic range of the SIS3316 (max 5 V).

Whereas the weighted average method without the corresponding weights for the Q.E. and the excepted APDs 4 and 8 works at least qualitatively for the collimated ^{137}Cs source, it fails for the measurement with the uncollimated ^{133}Ba source. The xy-position reconstruction of the uncollimated ^{133}Ba for a drift-field of 200 V/cm is shown in Figure 4.13. The corresponding energy spectra measured with the APDs 3,4,6 and 7 can be found in the Appendix in Figure 5.13 on page 124. Like the energy spectra

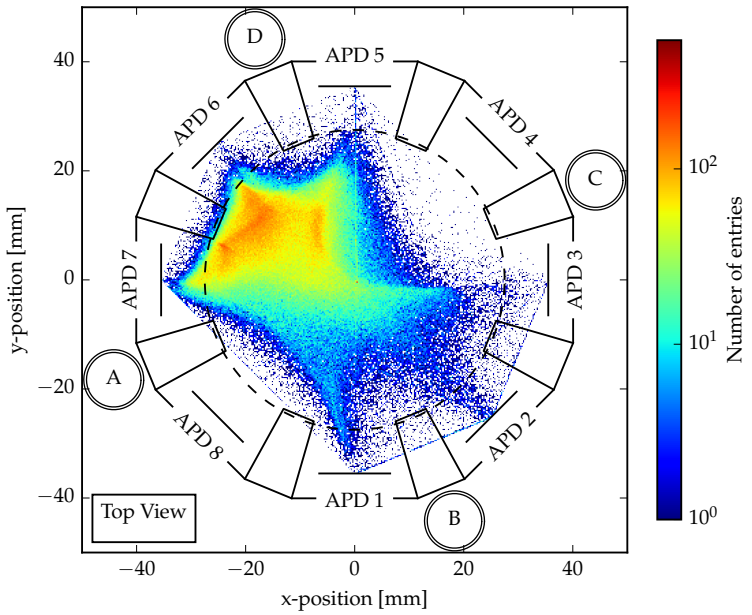

Figure 4.11 – *APD position reconstruction of the MainzTPC for a collimated ^{137}Cs beam according to the weighted average method without any weights for the Q.E.. The plot shows the position reconstruction for a weighting only with the relative APD gains. Further are APD 8 and its contrary APD 4 not included in the position reconstruction since the relative gain of APD 8 is not known. The collimated ^{137}Cs beam is coming from the upper left corner and is entering the MainzTPC between levelmeter A and D. The scatter plot uses a binning of a quarter millimeter.*

of ^{137}Cs it shows an artificial peak on the very right tail of the spectrum. Further one can see in Figure 5.13 that the three most dominant peaks of ^{133}Ba are overlapping and hence a estimation of the relative APD Q.E. cannot be performed with this calibration source either.

The distorted image of the ^{133}Ba xy-position reconstruction suggest that the majority of the interactions are taking place in the center of the TPC, which is very unlikely since the γ-energy of the ^{133}Ba decay is roughly half of the decay energy as for ^{137}Cs. Hence in order to improve the xy-position reconstruction and to make use of the data measured with APD 4 and 8 one can try to exploit the fact that the weighted average method is returning only a distorted mapping of the reality. The weighted average tends to return a symmetrically shaped pattern which can be used to introduce a "pseudo" Q.E. value for all eight APDs in order to "correct" the distorted mapping patterns. For example if the xy-position reconstruction based on only four opposing APDs is plotted, the weighted average with the correct weights should return by construction a symmetrically shaped cross-like pattern. As it can be seen in the upper plot of Figure 4.14 this is not the case for the calculations without any Q.E. values. Therefore arbitrary chosen pseudo values for a relative Q.E. had been multiplied to the eight APD weights until a more symmetrically distributed mapping was returned. The pseudo Q.E. had been estimated by eye only and hence are highly human biased. The result of this approach is exemplary presented for the odd numbered APDs in the

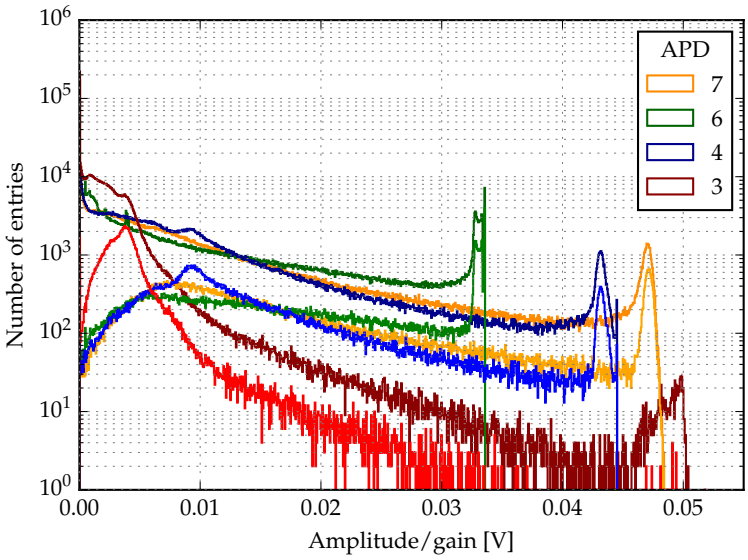

Figure 4.12 – *Energy spectra of the collimated ^{137}Cs source measured with the APDs 3,4,6 and 7. The number of entries versus the measured signal amplitude (charge) divided by the relative gain of the APD are plotted. The darker colored spectra represents the ^{137}Cs energy spectrum without any further cuts applied. The normal colored energy spectra show all events which were also used for the fitting of the full-energy peaks which is described in Section 4.3.*

lower plot of Figure 4.14. A plot for the even numbered APDs can be found in the Appendix in Figure 5.12 on page 123. The eight pseudo Q.E. values were calculated with the ^{137}Cs data-set. In order to make also use of APD 8 it gain was arbitrarily set to 150. The resulting xy-position reconstruction using all eight APDs together with the estimated pseudo Q.E. for the measured ^{137}Cs and ^{133}Ba source are shown together in Figure 4.15. The corresponding arbitrarily chosen values for the relative Q.E. can be found in Table 4.4.

Although this approach is only a work around for the missing gain of APD 8 and the missing Q.E. values it could have been used for a qualitatively study of the interaction positions of the ^{37}Ar later on. Especially the new xy-position map of the ^{133}Ba shown in the lower plot of Figure 4.15 seems to be more reasonable than the old one. However it is so far not understood why the xy-position reconstruction for the ^{137}Cs source lead to a broader and more frayed pattern than for the ^{133}Ba source. This has to be further investigated once the APDs are calibrated properly and their relative Q.E. values are known. Further this qualitative analysis of the APD position reconstruction unveils the limits of this method. Since no spatial boundaries are included some of the xy-positions of the S_2 signals are reconstructed to places where they cannot occur. This can be seen for example in the upper plot of Figure 4.15, where the position of some signals are reconstructed into the PTFE mesh holders. The second issues arise from the fact that the APD signals are exceeding the dynamic range of the SIS3316 when they occur close to one of the APDs. This problem affects both the weighted average and the light-map position reconstruction approach. Even though one can account for this problem by reducing the applied bias voltage of the APDs, this will lead to an

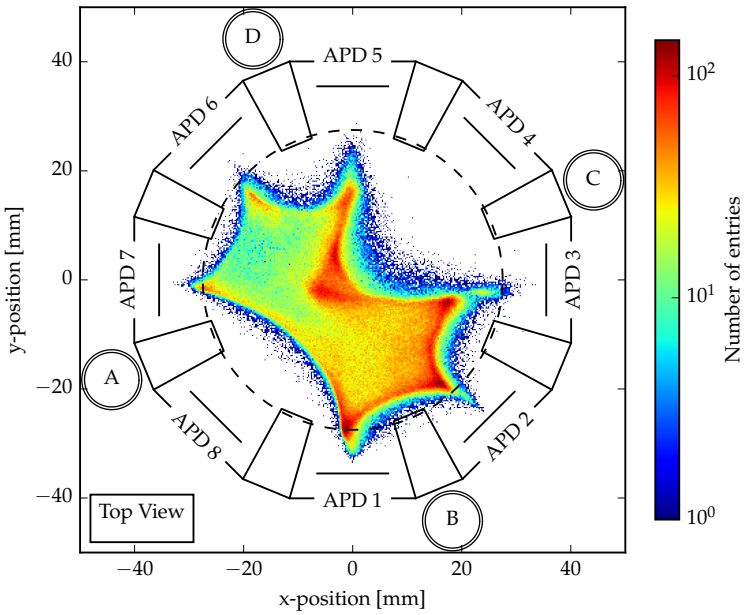

Figure 4.13 – *APD position reconstruction of the MainzTPC for an uncollimated ^{133}Ba source according to the weighted average method without any weight for the Q.E.. As for the collimated ^{137}Cs source the weights are only calculated with the APD gains and the APD 4 and 8 had been excluded from the position reconstruction. The ^{133}Ba source was mounted on the outer cryostat of the MaizTPC irradiating the detector from the lower left corner between APD 2 and 3.*

unwanted loss of sensitivity for small signals.

Since the pseudo Q.E. values are only guessed the xy-position reconstruction cannot be used for any further cuts until the relative Q.E. values were determined properly. Also the gain calibration of the APDs have to be redone once the glass fibers are replaced.

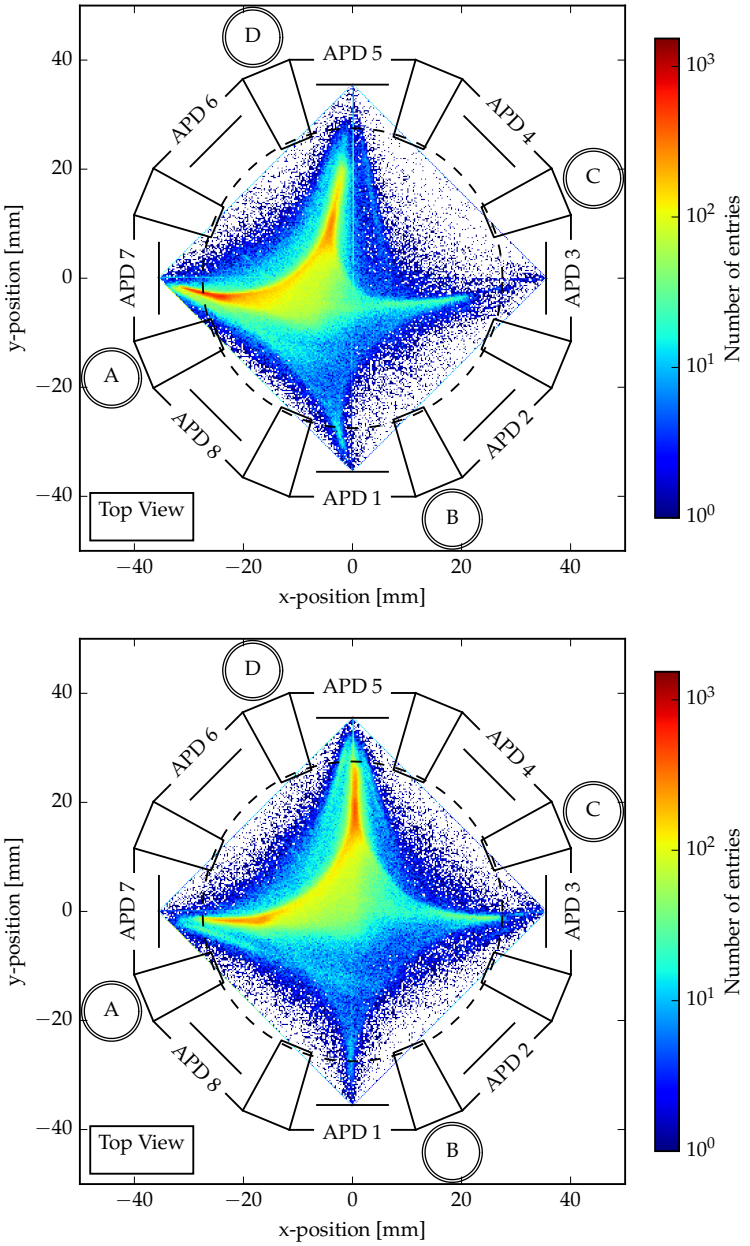

Figure 4.14 – *Illustration of the xy-position reconstruction for the MainzTPC using the weighted average method with and without the pseudo Q.E.. Both plots are showing the xy-position reconstruction when only the odd numbered APDs of the MainzTPC are used. The upper picture uses only the relative gains as a weight while the lower picture shows the mapping of the reconstruction if also the pseudo Q.E. values are applied. The data-set is the same like the one of Figure 4.11.*

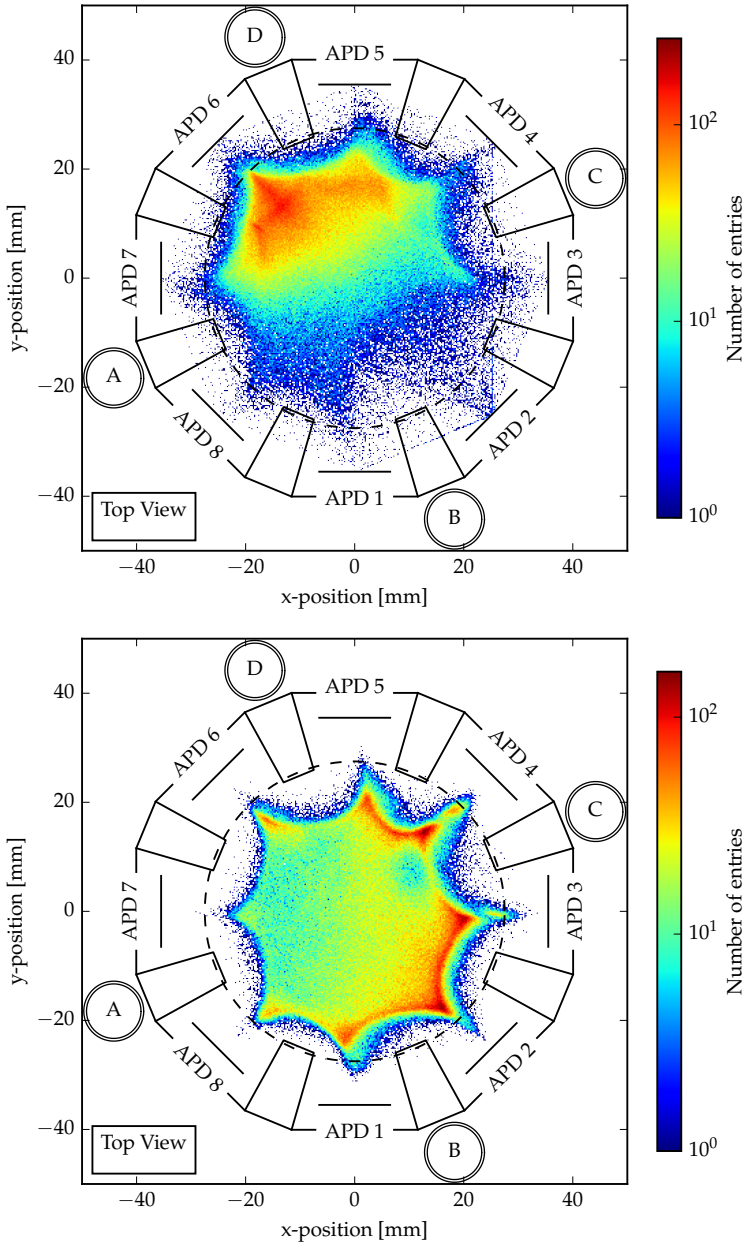

Figure 4.15 – *XY-position reconstruction for the ^{137}Cs and ^{133}Ba measurement using all eight APDs and the estimated pseudo Q.E. values. The upper picture shows the ^{137}Cs spectrum which was also presented in Figure 4.11, whereas the lower plot shows the ^{133}Ba data-set of Figure 4.13.*

4.6 ^{37}AR MEASUREMENT

In the following the results of the March 2018 run are presented. Section 4.6.1 deals with the calibration of the dosimetry branch as well as the dosimetry of the ^{37}Ar sample. Section 4.6.2 discusses the MainzTPC measurements of the ^{37}Ar sample and addresses questions about the sample activity, S_1 total energy spectrum and its z-distribution inside the MainzTPC as well as the time evolution of this distribution.

4.6.1 *Calibration of the Dosimetry branch and ^{37}Ar dosimetry*

The calibration of the dosimetry PMT was done in the same way like the MainzTPC's PMTs discussed in Section 4.1. The single photo-electron spectrum was fitted according to equation (4.2) with an additional exponential function $(A \cdot \exp(-m \cdot x))$ added to its second term. The fit and its result are shown together with data points in Figure **5.14** in the Appendix C. on page 125. The calibration was carried out with a amplification of 10.35 with the top PMT amplifier of the July run.

In addition to the amplified PMT signal the logic signal from the discriminator was recorded and used as well. It allowed to plot the resulting single photo-electron spectra for a given threshold by simply masking during the high level analysis the recorded events with the logic output of the discriminator. The resulting single photo-electron spectra for the different thresholds are presented in the lower plot of Figure **4.16**. The upper plot of Figure **4.16** represents the amplitude spectrum of the single photo-electron spectrum.

Before opening the ampule the background rate of the PMT was measured for different discriminator thresholds. Since the calibration measurement presented in Figure **4.16** was performed with the PRISMA Detector Lab amplifier while the dosimetry measurement was performed with the KPH amplifier, the discriminator thresholds set during the calibration must be converted to an effective discriminator threshold accordingly. This allows to compare the measured background rates with the single photo-electron spectra presented in Figure **4.16**. The conversion factor f_{con} is given by

$$f_{\text{con}} = \frac{g_{\text{detlab}}}{g_{\text{KPH}}} = \frac{10.3493}{4.4351} = 2.3335\,,$$

where g_{detlab} represents the gain of the top PMT amplifier and g_{KPH} the gain of the bottom PMT during the July run. The different measured background rates are stated in Table **4.5**. As a result of this background measurement and the single photo-electron spectra a discriminator threshold of 20 mV was chosen for the dosimetry of the ^{37}Ar sample. Hence the effective threshold is well above the single photo-electron mean value.

Beside the dosimetry PMT calibration the second important parameter which needed to be determined for the activity measurement is the volume of the dosimetry branch. Therefore the branch was flushed with nitrogen whose mass was integrated by the flow meter. Since the flow meter is calibrated for xenon gas an additional conver-

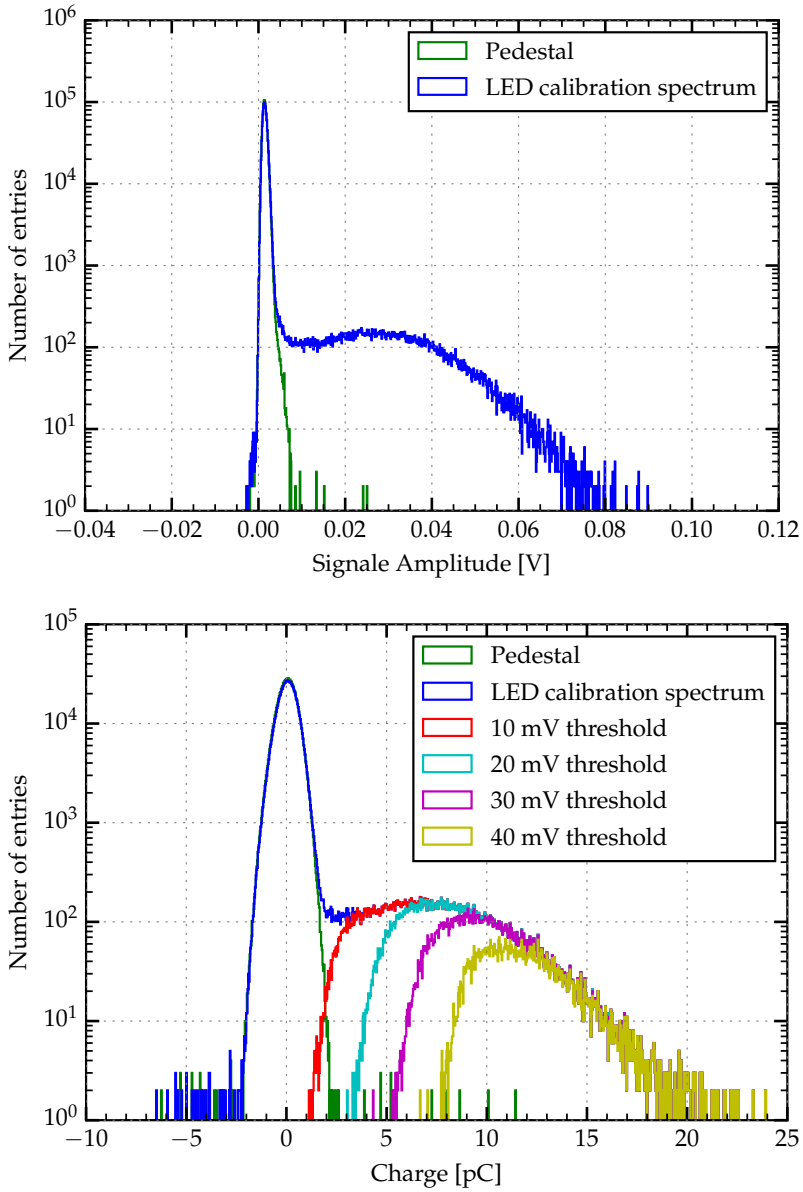

Figure 4.16 – *Amplitude and single photo-electron spectrum of the dosimetry PMT. The single photo-electron spectrum was measured for different discriminator thresholds which are presented in the lower plot.*

sion factor f_{flow} had to be applied which was given by the manufacturer [Tel]. The integrated nitrogen mass m_{N2} is then given by

$$m_{\text{N2}} = m_{\text{Xe}} \cdot f_{\text{flow}} \cdot \frac{\rho_{\text{N2}}}{\rho_{\text{Xe}}} \quad \text{with} \quad f_{\text{flow}} = \frac{1}{1.32}\,, \tag{4.12}$$

in which ρ_{i} is the gas density of xenon 13.108 kg/m^3 (i = Xe) and gaseous nitrogen

Table 4.5 – *Background rate of the dosimetry PMT for different discriminator threshold settings. Stated are the set discriminator threshold, the corresponding effective threshold like explained in the text, the number of counts measured by the scalar, the used time interval of the scalar and the corresponding background rate of the PMT. The error of the rate was calculated according the Gaussian error propagation. The error of the time interval was neglected.*

Threshold [mV]	Effective Threshold [mV]	Counts	Time [s]	Rate [Hz]
10	23.33	43978	300	(146.59 ± 0.70)
15	35.00	18460	300	(61.53 ± 0.45)
20	46.67	9053	300	(30.18 ± 0.32)
30	70.00	3996	300	(13.32 ± 0.21)
35	82.67	3477	300	(11.59 ± 0.20)

$2.7614\,\mathrm{kg/m^3}$ (i = N2) at a temperature of 293 K correspondingly [Nat]. One cycle of this volume measurement is presented in Figure 4.17. The separate volumes were filled successively until each volume contained a filling pressure p of 2.4 bar of dry nitrogen. The sharp left edges of the pressure drops represent the opening of a new volume. The last pressure drop which can be seen in this cycle belongs to a volume which was opened in order to pump the dosimetry branch for the next filling cycle. Afterwards the volume V was calculated by using the ideal gas law

$$V = \frac{m_{\mathrm{N2}} \cdot R \cdot T}{p \cdot M_{\mathrm{N2}}}, \tag{4.13}$$

where R represents the universal gas-constant, $M_{\mathrm{N2}} = 28.0134\,\mathrm{g/mol}$ [Nat] the molar weight of gaseous nitrogen and T the laboratory temperature which was determined to be 293 K. This procedure was repeated five times and the mean volume was calculated. The volumes were estimated to be $(8.91 \pm 0.27)\mathrm{cm^3}$ $(318.33 \pm 0.36)\mathrm{cm^3}$, $(3.53 \pm 0.78)\mathrm{cm^3}$ and $(177.82 \pm 1.75)\mathrm{cm^3}$ for the VCR union cross, the volume D-PMT, the intermediate volume and the volume D-PH respectively. The error of the volumes were calculated by the error of the mean. As a comparison, the manufacturer Swagelok [Swa] states a volume of $\sim 3.2\,\mathrm{cm^3}$ for the intermediate volume, which is in agreement with the measured value. The same procedure was used to determine the total volume of the MainzTPC and the xenon liquefaction vessel which yielded a volume of $(7091 \pm 71)\,\mathrm{cm^3}$. Since this volume measurement was performed just a single time the stated error was estimated to be 10 % which is comparable to the errors of the larger volumes of the dosimetry branch. The volume of the gas-system was neglected during this measurement. In order to confirm if this value is reasonable the volumes of the TPC and xenon liquefaction vessel were estimated based on their CAD models. It yielded a volume of $5273\,\mathrm{cm^3}$. Since the estimated value based on the dry nitrogen mass integration also includes the volume of the overall piping, the value seems to be reasonable. As comparison the total light sensitive volume of the MainzTPC is $159\,\mathrm{cm^3}$ while the liquid volume[3] is $111\,\mathrm{cm^3}$.

After opening the quartz ampule the dosimetry of the ^{37}Ar was performed in several trials. Since no rise of the trigger rate was observed after performing the rough

[3]The volumes of the MainzTPC were calculated according to the sizes of the CAD model.

dosing process two times, it was decided to leave the valves D-V1 and D-V2 of the intermediate volume between D-PH and D-PMT open for one entire night (14 h). This led to a rise of the trigger rate of the dosimetry PMT above its background rate, like presented in Figure 4.18. The average of the background corrected trigger rate was (35.42 ± 0.14)Hz which corresponds to a total ^{37}Ar activity of

$$A_0 = \frac{V_{\mathrm{DPH}} + V_{\mathrm{r}} + V_{\mathrm{DPMT}}}{V_{\mathrm{mes}}} \cdot A_{\mathrm{mes}} = (5.006 \pm 0.030)\,\mathrm{kBq}$$

assuming a counting sensitivity of 100 % for the dosimetry PMT and a homogeneous ^{37}Ar distribution. The stated error was calculated according Gaussian error propagation. This measured value is roughly a factor ten lower than the expected activity of (49 ± 12) kBq. Since it was unclear if this large discrepancy was caused by an insensitivity of the dosimetry PMT for the small signals of ^{37}Ar or a wrong estimate of the ^{36}Ar content in the quartz ampule before its irradiation, it was decided to inject only half of the xenon ^{37}Ar mixture from the D-PMT volume into VCR union cross. This ensured that the activity deposit into the TPC would neither be to high nor to low. The recirculation was then redirected through the filling unit of the dosimetry branch for 10 min before standard recirculation conditions were reestablished. This was necessary to safely refill the D-PMT volume back to a pressure of 2.3 bar. Directly after this refilling a rate of only (4.30 ± 0.50) Hz was measured which is only a $1/7$ of the initially measured rate. Although the valves D-V1 and D-V2 remained closed until 13:18 the trigger rate rose to a value of (13.65 ± 0.50) Hz. This observation might be explained by a redistribution of the ^{37}Ar inside the D-PMT volume due to the refilling of the xenon gas. Furthermore this value seems to be more reasonable, since the particle density of ^{37}Ar should only be halved.

This first filling did not lead to a rise of the trigger rate of the MainzTPC. Hence around 18:10 o'clock it was decided to fill also the entire rest of the ^{37}Ar inside the dosimetry unit into the recirculation system and the MainzTPC. The fact that the first filling did not lead to a rise of the trigger rate inside the MainzTPC is another indication, that the real activity of the ^{37}Ar sample was lower than the expected (49 ± 12) kBq.

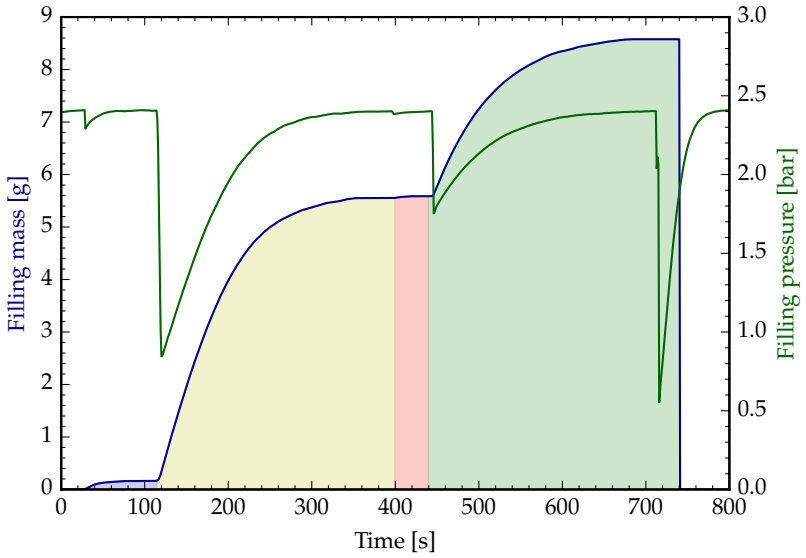

Figure 4.17 – *Volume measurement of the dosimetry branch. The blue line represents the filled integrated mass of nitrogen, while the green line represents the filling pressure measured at D-P1. The different colored shaded areas indicate the different parts of the dosimetry branch. The blue area represents the VCR union cross between the valves D-V3, D-V4 and D-FDV1, the yellow part the dosimetry PMT T-volume (D-PMT). In red the intermediate volume between valve D-V1 and D-V2 and in green the volume of the guillotine mechanism (D-PH) are indicated.*

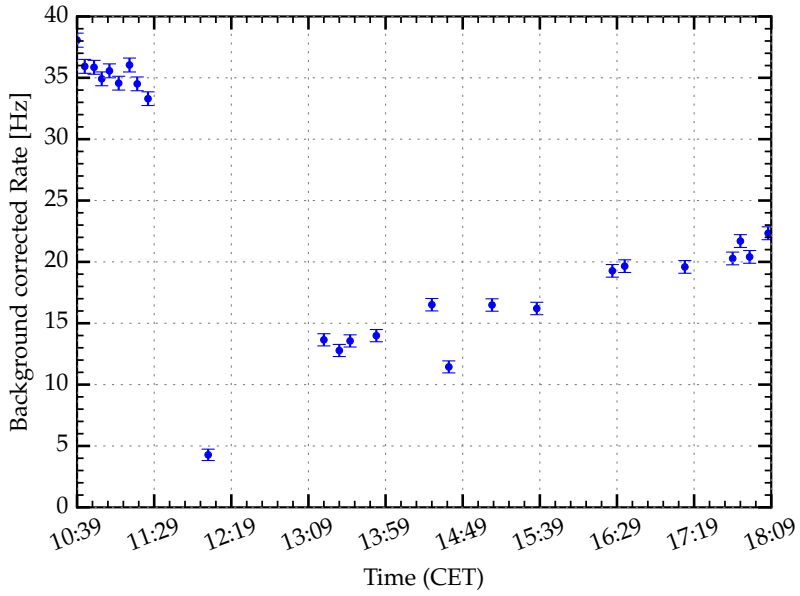

Figure 4.18 – *Trigger rate of the dosimetry PMT after opening the quartz ampule of the ^{37}Ar sample. Plotted is the background corrected trigger rate (-30.18 Hz) versus time. The presented values were measured on the 09.03.18. The trigger rate which is measured between 10:39 and 11:29 was taken after the valves D-V1 and D-V2 were left open for 14 h. The drop of the activity after 11:29 is caused by the first injection of the ^{37}Ar into the xenon recirculation circuit. After this injection the valves D-V1 and D-V2 were opened again at 13:18, leading to anew rise of the trigger rate until 18:09 and the second ^{37}Ar injection.*

4.6.2 *Study of the ^{37}Ar sample with the MainzTPC*

The second injection of the remaining ^{37}Ar sample brought clear evidences that the MainzTPC is capable to measure the 2.8 keV transition of ^{37}Ar. Figure 4.19 shows the average trigger rate of each data acquisition cycle. This rate is calculated by the number of waveforms within one cycle divided by the period of the cycle. It is not affected by any dead time since the ring buffer of the SIS3316 allows a dead time free recording within one of those acquisition cycles. The trigger rate of the top PMT starts to rise around 18:30 and is peaking at 18:45 o'clock. The rise of the trigger rate starts at the same time when the recirculation flow of the xenon gas was redirected through the filling unit after the ^{37}Ar injection. The recirculation transported the calibration gas almost instantly into the MainzTPC. After the peak of the trigger rate the ^{37}Ar starts to spread over the entire volume of the experiment leading to a decrease of the ^{37}Ar density inside the MainzTPC and therefore to a decrease in trigger rate. The trigger rate is slightly increasing during the entire bottom PMT triggered measurement. This slight increase might either indicate that the ^{37}Ar was not homogeneously distributed over the whole volume at that time, or that some additional left over ^{37}Ar was slowly diffusing from the dosimetry branch into the recirculation circuit since the valves were left open.

The large spread of the trigger rate of the bottom PMT triggered ^{37}Ar measurement compared to its background measurement is caused by a periodic effect in the data

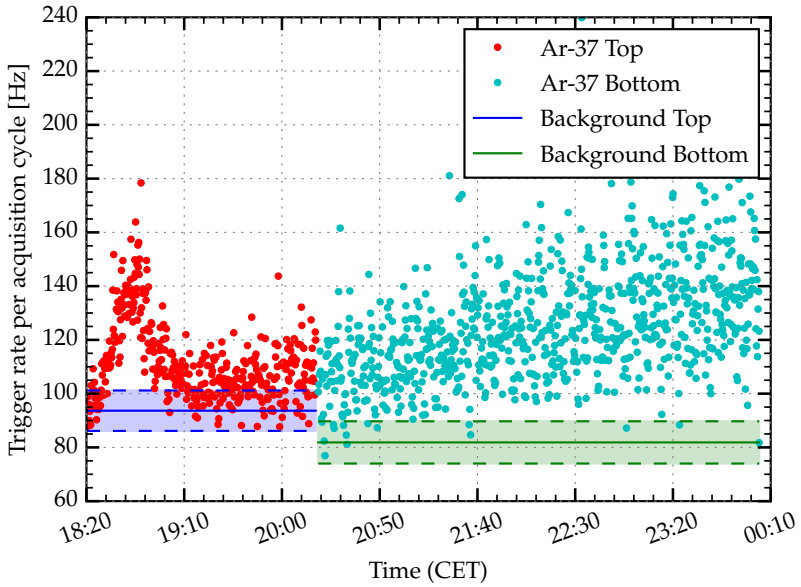

Figure 4.19 – *Average trigger rate per acquisition cycle of the MainzTPC after the second ^{37}Ar injection. The red colored data point represents the measurement triggered with the top PMT and the cyan colored data points the subsequent measurement triggered by the bottom PMT. The green and blue line represents the average background rate of the MainzTPC for the corresponding trigger setting. The respective colored bands represent a one sigma confidence belt.*

points. This effect can be seen if one plots only a small excerpt of the measurement and interpolate the data points linearly. The periodicity of this effect is in the order of 9 min to 10 min and is shown in Figure **5.15** in the Appendix C. on page 125. The origin of the effect is not clear at the moment. A periodicity change of the ^{37}Ar concentration inside the MainzTPC volume due to the recirculation seems to be unlikely. The diffusion of the ^{37}Ar through the buffer and liquid filled pipes should take longer than ten minutes. It seems to be more likely that this effect is caused by the periodic liquid level oscillations inside the MainzTPC. Their periodicity is in the same order of magnitude as can be seen in Figure **4.25** of Section 4.7. However due to the fact that the levelmeter read-out is causing a dominant noise on the PMT signal lines the levelmeter read-out is switched off during every measurement and hence it is difficult to judge if both effects are related with each other.

Assuming that an equilibrium of the ^{37}Ar distribution is reached in the last ten minutes of the bottom PMT triggered measurement one can estimate the activity of the ^{37}Ar sample. Taking the mean of the corresponding data points yields a trigger rate r_{trig} of 138 Hz with a standard deviation of 20 Hz. Using the ratio between the light sensitive volume of the MainzTPC V_{TPC} and the volume of the experiment V_{exp} this leads to an activity of

$$A_{\text{total}} = \frac{V_{\text{exp}}}{V_{\text{TPC}}} \cdot r_{\text{trig}} = \frac{7091}{159} \cdot 138\,\frac{1}{\text{s}} = (6.2 \pm 0.9)\,\text{kBq}$$

with the uncertainty calculated according to Gaussian error propagation. This value is higher compared to the result estimated with the dosimetry PMT, but still way below the expected activity of (49 ± 12) kBq. Also taking the branching ratio of 0.9 for the 2.8 keV transition into account does not change much on the derived activity. A further look into the S_1 total energy spectrum shows that the estimated activity of (6.2 ± 0.9) kBq can only be seen as a lower bound for the actual activity. Figure **4.20** presents two S_1 total spectra of the ^{37}Ar measurements after the coincidence cut. In both plots the recorded spectra after the second ^{37}Ar injection are showing an enhanced rate around 1 pe to 20 pe. This enhancement can be interpreted as the 2.8 keV transition from ^{37}Ar. Further the enhancement is more prominent for the upper plot since the ^{37}Ar concentration inside the MainzTPC was highest during this measurement. These plots are showing why the estimated activity is only giving a lower boundary for the actual activity: The trigger threshold of the detector cuts a part of the events. In order to get a better representation of the activity it was tried to fit the background corrected S_1 total ^{37}Ar peak of the top PMT triggered measurement with a model spectrum

$$f(x) = \frac{1}{1 + \exp(-k\,(x - x_0))} \cdot N'(A, \mu, \sigma^2) \tag{4.14}$$

where k is the steepness and x_0 the middle of the sigmoid shaped logistic function. The logistic function is a more generalized representation of the Fermi-Dirac distribution and was used in order to model the threshold effect of the detector. However this fit model did not catch the background corrected spectrum entirely. Hence it was not

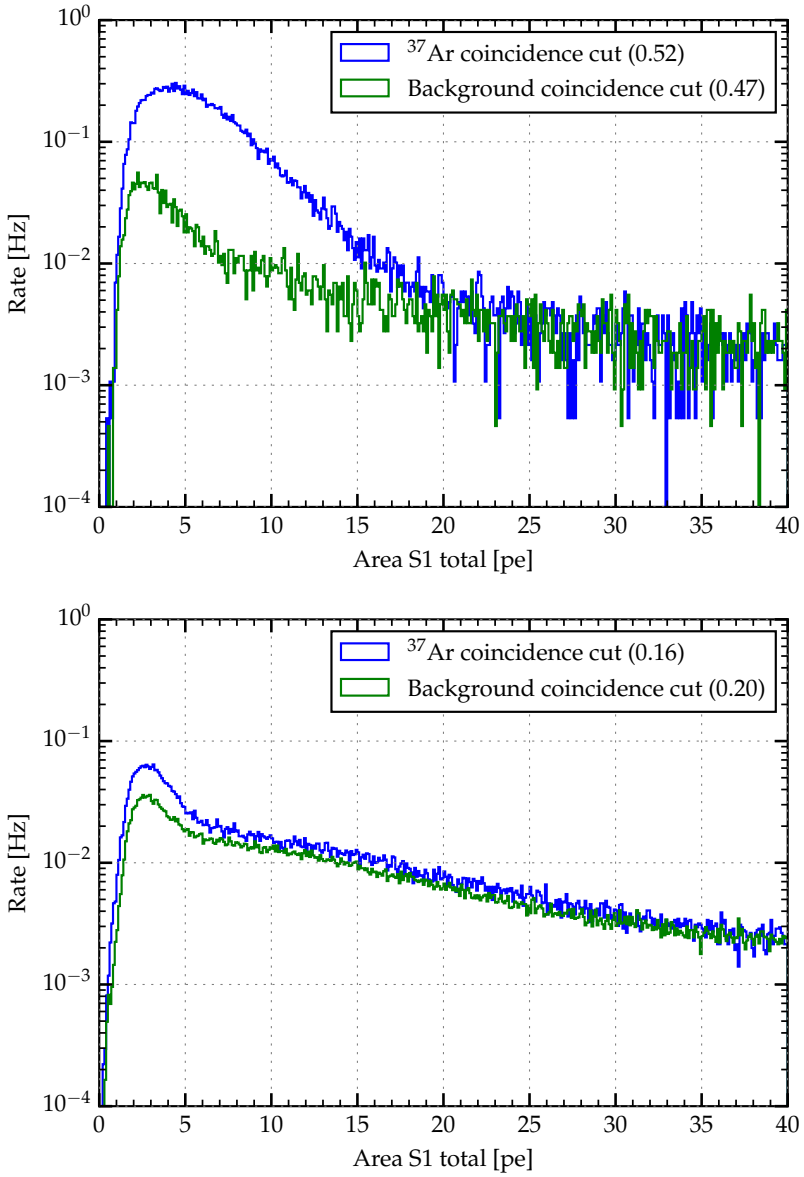

Figure 4.20 – *S_1 total energy spectra for the ^{37}Ar measurements and the correspondingly measured backgrounds. Both plots are showing the dead time free rate versus the total S_1 area. The upper plot presents an excerpt of the top PMT triggered measurement from 18:20 until 19:10 (see Figure 4.19), while the lower plot presents the spectrum of the entire bottom PMT triggered measurement. The coincidence cuts were used as explained in Section 4.2.*

possible to calculate a more accurate activity for the ^{37}Ar sample. One example fit is shown in Figure 5.16 in the Appendix C. on page 126.

One big question with respect to the ^{37}Ar calibration of the XENON1T and XENONnT detector is how well the ^{37}Ar diffuse into the LXe of the detector. Although the field cage failed during the March run this question can be still answered looking at the area fraction top parameter. The area fraction top for the spectra shown in Figure 4.20 are

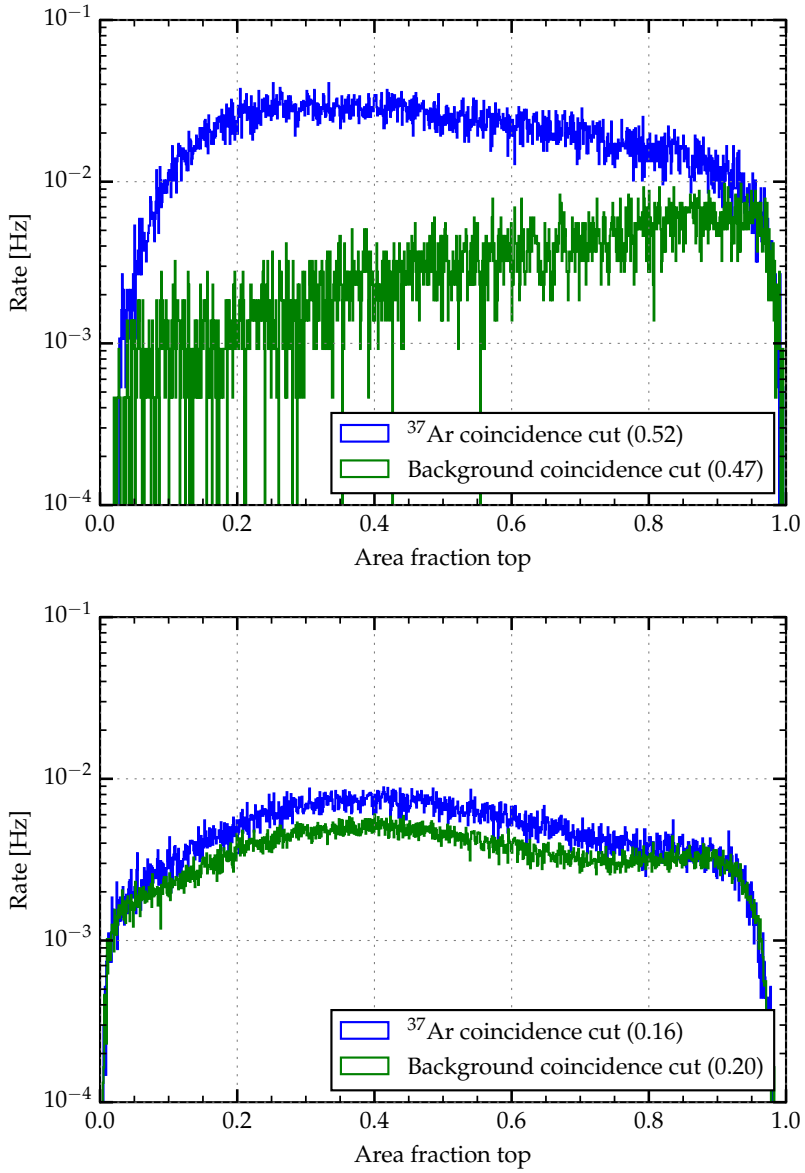

Figure 4.21 – *Z-distribution of the measured rate according to the area fraction top parameter for the spectra shown in Figure 4.20. The upper plot shows the measurement which was triggered with the top PMT, while the lower plot shows the bottom PMT triggered measurement.*

presented in Figure 4.21. They show that the ^{37}Ar was distributed over the entire liquid and gaseous phase of the MainzTPC. Comparing the measured area fraction top values of the two spectra with the calibration curves in Figure 4.8 and Figure 4.10 the measured rates show that the ^{37}Ar distributes spatially over the whole LXe phase of the TPC.

Since the ^{37}Ar calibration gas should arrive first in the gaseous phase of the detector, a time dependent development of the area fraction top parameter could give information about how fast the ^{37}Ar distributes over the MainzTPC volume. The time depen-

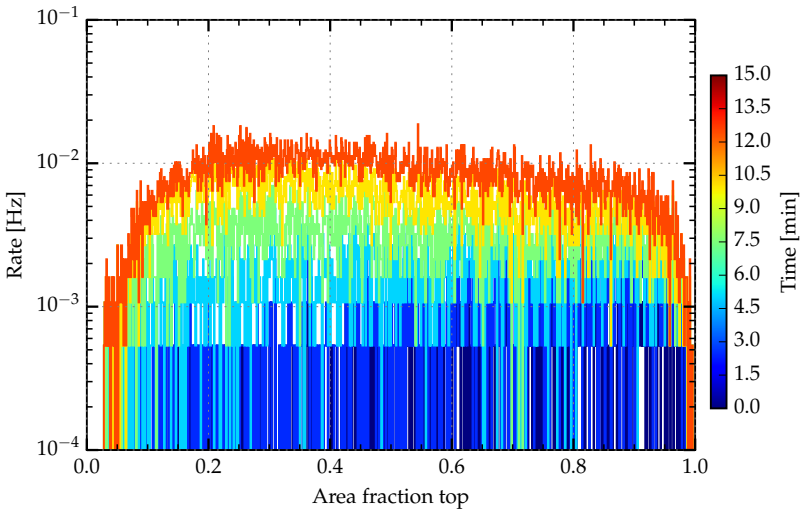

Figure 4.22 – *Time evolution of the measured rate of the top PMT triggered ^{37}Ar measurement versus the area fraction top parameter. The presented data was measured between 18:20 and 18:35 o'clock. The spectra represents the measured rate in 3 min intervals.*

dent evolution is shown in Figure 4.22. The plot shows the measured rate versus the area fraction top in 3 min intervals. The measured rate is increasing homogeneously over the whole volume. Smaller time intervals did not lead to any improvement, hence it is most likely that the resolution of the area fraction top parameter is not high enough to see any time development of the z-distribution.

A last point which is sticking out for the presented measurements is the fact that the cut efficiency of the bottom and top triggered background measurement is deviating by a factor of about 2.35. This can either be interpreted as a higher dark count rate of the bottom PMT, as a higher sensitivity of the bottom PMT for small signals, or a mixture of both.

4.7 STUDY OF THE MAINZTPC LIQUID LEVEL AND THE NEW SPILLWAY

The fluctuation of the liquid level inside the MainzTPC is a long known problem and was already qualitatively studied in [Bes17]. Even though the level concept of a spillway like the ones presented in Figure 2.4 in Section 2.1 and Figure 2.6 of Section 2.1.1 works, the liquid level experiences a periodic level drop inside the TPC chamber. They are featured by a fast falling edge and a slow recovery to the overall adjusted level. Examples of the fluctuations are represented in Figure 4.25 for measurements with the old and new spillway respectively. The upper plot of Figure 4.25 shows that a level drop in the TPC leads to a level rise in the buffer volume.

Based on these qualitative observations one possible explanation is that the fluctuation might be caused by surface tension effects and a pile-up of the liquid level before it is finally drained by the spillway. This initial idea was corroborated by studies with a spare spillway and normal water and were carried out by the Bachelor research as-

Figure 4.23 – *Pictures of the liquid level tests with water. The old and new spillway are shown on the left and right hand side correspondingly. The picture on the left shows at the edge of the old spillway a pile-up of the liquid, while the new spillway in the picture on the right hand side does not. Both photographs were taken by David Maksimovic.*

sistant David Maksimovic. Water has a viscosity of 1.08 mPa·s and a surface tension of 73.21 mN/m at a temperature of 290 K which is in the same order of magnitude as for liquid xenon. Xenon has a viscosity of 0.40 mPa·s and a surface tension of 15.66 N/m at temperature 180 K [Nat]. In order to test the surface tension hypothesis the old spillway was mounted into the plughole of a commercial available plastic funnel. Afterwards the funnel was slowly filled with water by using a syringe. Based on this observations a first prototype for a new spillway was also studied by David Maksimovic. The prototype is based on the old spillway design whose edges were rounded and an additional v-shaped cut was carved into the spillway. This minimizes the distance the liquid has to overcome in order to be drained by the spillway. A qualitative comparison between the old and new spillway is shown in Figure 4.23. The photography on the left hand side shows clearly a pile-up of the liquid level at the edge of the spillway which is due to the surface tension of water. In contrast the new spillway drains the liquid level through the v-shaped cut with a constant flow and therefore prevents any pile-up of the liquid level.

Since the first observations were promising a new and more appropriated design of the spillway was done using the CAD software *SolidWorks* [Sol]. The spillway had been produced by the in-house mechanics workshop of the institute for physics and was mounted into the MainzTPC vessel during the maintenance in November 2017. The new spillway is shown in Figure 2.6 on page 37.

In order to study the level fluctuations more quantitatively a piece-wise defined exponential function was fitted to the data. The function is described by two exponential decays each with a separate decay time in order to model the the liquid level drop and its recovery. The exponential functions were simply motivated by the fact that the level fluctuation in Figure 4.25 show atleast by eye an exponential shaped behavior. Therefore the liquid level $L(t)$ at a given time t is described by

$$L(t) = \begin{cases} h_0 - A \cdot \exp\left\{ -\left(\frac{t_{\text{dip}} - t}{\tau_{\text{fall}}} \right) \right\} & \text{when} \quad t \leq t_{\text{dip}} \\ h_0 - A \cdot \exp\left\{ -\left(\frac{t - t_{\text{dip}}}{\tau_{\text{rise}}} \right) \right\} & \text{when} \quad t > t_{\text{dip}} \end{cases} \tag{4.15}$$

where h_0 is the liquid level before and after the drop, A the depth of the drop, t_0 the position of the liquid level minimum, τ_{fall} the time-constant of the falling edge and τ_{rise} the time-constant of the liquid level recovery. One example fit is shown in the upper plot of Figure 4.24. For this example the fit yields the values: $A = (0.49 \pm 0.02)\,\text{mm}$, $t_0 = (13.25 \pm 0.32)\,\text{min}$[4], $h_0 = (3.17 \pm 0.01)\,\text{mm}$, $\tau_{\text{fall}} = (0.48 \pm 0.65)\,\text{s}$ and $\tau_{\text{rise}} = (133.13 \pm 13.67)\,\text{s}$ as well as a χ^2/ndof of 1.85/394. The poor χ^2/ndof-ratio comes from the fact that the fit was performed without any weights of the data points (using a $\sigma_i = 1$) since their uncertainties are unknown. However a χ^2/ndof-ratio less then one is only an indication for overestimated errors but does not provide in general an evidence against the hypothesis or fit function [Cow98]. The residuals versus fit function in the upper plot of Figure 4.24 shows a equal distribution of the residuals around zero. It also shows a clustering of fit values right below 3.17 mm. However, the uniform spread of the residuals shows that equation (4.17) can describe the rough behavior of the fluctuations. But the clustering also indicates that transition between the exponential functions and the constant liquid height h_0 is not smooth enough and must be improved further.

In addition to the piece-wise defined exponential fit model a second model was fitted to the data. It uses three linear functions which are also piece-wise defined. This model can be motivated by the fact that a constant xenon recirculation flow should lead to a linear rise of the liquid level after a drop occurred. The rise-time T_{r} is then simply given by

$$T_{\text{r}}(A, F_{\text{Xe}}) = V \cdot \left(\frac{A}{5\,\text{mm}}\right) \cdot \frac{\rho_{\text{LXe}}}{F_{\text{Xe}}} \tag{4.16}$$

where V represents the volume between the height of the gate and anode mesh which is occupied by the LXe, ρ_{LXe} the density of liquid xenon and F_{Xe} the xenon recirculation flow in xenon mass per unit time. The fit function for the level fluctuations is given by

$$L(t) = \begin{cases} f(t) & \text{when} \quad t < t_{\text{fall}} \\ \frac{f(t_{\text{fall}}) - h_{\text{low}}}{t_{\text{fall}} - t_0} \cdot (t - t_{\text{dip}}) + h_{\text{low}} & \text{when} \quad t_{\text{fall}} \leq t \leq t_{\text{dip}} \\ \frac{f(t_{\text{thigh}}) - h_{\text{low}}}{t_{\text{high}} - t_0} \cdot (t - t_{\text{dip}}) + h_{\text{low}} & \text{when} \quad t > t_{\text{dip}} \end{cases} \tag{4.17}$$

together with

$$f(t) = m_0 \cdot (t - t_{\text{dip}}) + h_0\,, \tag{4.18}$$

where m_0 represents the slope of the liquid level baseline, h_{low} the liquid level after the the level drop, t_{fall} the start point of the level drop and t_{high} the time point when the liquid level reaches again the height of the original liquid level. This fit model was also fitted to a variety of liquid level drops, but yielded only poor results. The lower plot of Figure 4.24 shows the linear fit model fitted to the same data as the exponential fit model. It returned the following values for its parameter: $h_{\text{low}} = (2.81 \pm 48446.88)\,mm$, $h_0 = (3.19 \pm 4372.7)\,mm$, $t_0 = (13.24 \pm 635701.87)\,\text{min}$, $t_{\text{high}} = (18.65 \pm 3.40)\,\text{min}$, $t_{\text{fall}} = (13.25 \pm 0.12)\,\text{min}$ and $m_0 = (0.11 \pm 0.65)\,\mu\text{m/s}$ as well as a χ^2/ndof of 1.92/394. The huge uncertainties of the fit parameters making the

[4] The position in time corresponds to the plot in Figure 4.25 not to Figure 4.24.

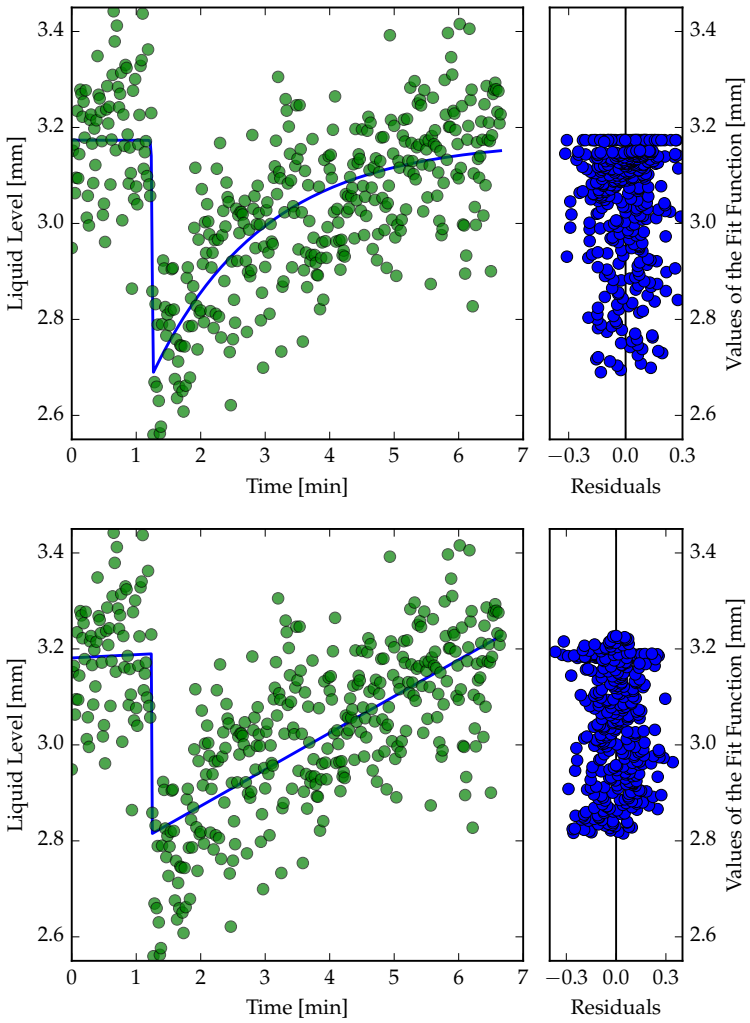

Figure 4.24 – *Fit of the LXe level fluctuations. Presented are the best fits (blue lines) of the two fit models discussed in the text. The upper picture shows the double exponential fit, while the lower plot shows the piece-wise defined linear fit. The green data points correspond to the third level sink of levelmeter B shown in the lower plot of Figure 4.25. The plots on the right hand side represents the values of the corresponding fit function versus its residuals.*

results unusable. Further shows the residuals plot of the fit a slight curvature, which indicates that the used model is not appropriated. Thus the exponential fit model was used for a further analysis.

In order to quantify if the new funnel improved the stability of the liquid level the fit function was applied to several level fluctuations during the July 2017 and March 2018 measurement. Unfortunately the levelmeter cannot be operated while measuring with the MainzTPC since the read-out cycle of the UTI evaluation boards causes a dominant noise on all sensors of the TPC. Hence the levelmeter are only operated while filling and recuperating the Xenon as well as in between of two measurement. The two time periods of the July 2017 and March 2018 run which were analyzed are shown in

Figure 4.25. This periods were selected since their thermodynamic conditions were comparable like shown in Figure 4.26.

Already from the different used time scales in Figure 4.25 one can see that the behavior of the level fluctuations changed with the new spillway. While with the old spillway the liquid level was stable for a short time period after each level drop, this condition was never reached with the new one. The exponential fit model was applied to all level dips in Figure 4.25, but only the level drops which are indicated by the gray dashed lines were used for the analysis. In the other cases the level fluctuation were distorted and the applied fit functions did not converge properly. An average of the received fit parameter values can be found in Table 4.6. Only the values of the levelmeter B,C and D were used during this analysis since UTI-2 failed during the March 2018 run. Table 4.6 makes also quantitatively clear that the new funnel did not improve the level fluctuations problem. The drops of the liquid level have become deeper with the new funnel and the recovery of the liquid level last longer than before. This is a little bit disappointing since the tests with normal water showed a clear improvement. Hence the problem of the level fluctuation might be either much more complex, the real origin of the fluctuation is not understood, or water is not suited well enough as a reference model. A better comparison might be achieved with methanol which has a viscosity of 0.5750 Pa·s at 293.15 K and a surface tension of 22.9 mN/m at 290 K [KVA67, Nat].

Comparing the derived time constants for the liquid level recovery τ_{rise} of Table 4.6 with the corresponding rise-times calculated according to (4.16) give also rise for questions. The LXe occupies a total volume of 73 cm^3 between the gate and anode mesh according to the *SolidWorks* model of the MainzTPC and its vessel. Hence a level dip of 0.32 mm in the July 2017 and 0.44 mm in the March 2018 run with a xenon recirculation speed of 5 slpm (0.489 g/s) should be fully recovered after 28 s and 39.5 s respectively. These times are in contradiction with the estimated time constants of the rising edges, which suggest according to $T_{\text{r}} \approx 4 \cdot \langle \tau_{\text{rise}} \rangle$ a rise time of atleast 67.56 s and 424.48 s correspondingly. The longer rise-time of the new funnel can be interpreted as a delay of the LXe level recovery due to the constant drain of LXe through the v-cut of the funnel. Unfortunately this cannot be justified with the buffer levelmeter due to the failure of UTI-2 during the March run. Nevertheless it seems to be likely that the new funnel is working as expected, but does not lead to an improvement in the level stability. Hence one can conclude that the level fluctuations are not caused by a liquid level pile-up effect.

Also a closer look into the buffer levelmeter data in the upper plot of Figure 4.25 and the plots of [Bes17] give rise to doubt the surface tension hypothesis. The slow rise of the buffer level just before the liquid level drops inside the MainzTPC cannot be explained by the liquid level fluctuation. Further it is odd that the buffer level falls instead to rise after the level drop inside the TPC occurred. The rise of the liquid level inside the buffer volume which starts even before the liquid level of the MainzTPC drops could be an indication that pressure balance between the chamber of the MainzTPC, and the pressure before and after the recirculation pump changes. However such an effect was not observed in the recorded data.

Beside the study of the liquid level fluctuations one can see in the upper plot of

Table 4.6 – *Averaged fit parameters according to the function (4.17) for the levelmeter B,C and D of the in Figure 4.25 emphasized level fluctuations. The uncertainties are given by the error of the mean.*

Measurement	A [mm]	h_0 [mm]	τ_{fall} [s]	τ_{rise} [s]
July 2017:				
Levelmeter B	0.31 ± 0.04	4.82 ± 0.01	0.72 ± 0.44	17.56 ± 2.38
Levelmeter C	0.34 ± 0.03	4.67 ± 0.01	0.48 ± 0.22	14.19 ± 1.79
Levelmeter D	0.30 ± 0.03	4.83 ± 0.01	0.49 ± 0.24	18.92 ± 2.31
March 2018:				
Levelmeter B	0.45 ± 0.01	3.19 ± 0.10	2.98 ± 1.14	93.37 ± 9.06
Levelmeter C	0.44 ± 0.01	2.55 ± 0.01	1.98 ± 0.73	115.36 ± 8.20
Levelmeter D	0.43 ± 0.01	2.29 ± 0.01	3.18 ± 1.14	109.63 ± 9.23

Figure 4.25 that levelmeter A has a slight offset compared to levelmeter B,C and D. This is caused by a small tilt of the MainzTPC during this run and is further discussed in [Sisd]. Levelmeter B in the March 2018 run is also showing an offset of the liquid level with respect to levelmeter C and D. This indicates that the TPC was not leveled proper enough after the TPC maintenance.

The last point concerning the levelmeters which was studied during this work is the long time variation of the levelmeter calibration. The multi-pin feed through which connects the two UTI evaluation boards with the TPC levelmeter is a little bit unsteady and can cause a shift of the overall levelmeter capacitance even though that the UTI boards account for any parasitic capacitance of the used cables. The calibration data for the different levelmeter can be found in Table 4.7. While levelmeter B,C and D which are read-out by UTI-1 are showing only a little variation in the calibration data, the values for the Buffer levelmeter and levelmeter A which both are measured by UTI-2 changed completely after the TPC maintenance in November 2017. Since tests with different fixed capacitance in the range of 5 pF to 20 pF did not show any problems, the issue seems to come from the levelmeter cables inside of the MainzTPC cryostat. Moreover the measured value of the reference capacitance of UTI-2 started to oscillate during the March 2018 run and hence a a conversion into a real capacitance value was not possible. The maximal change of the levelmeter B,C and D is given by levelmeter B which shows a 1 % difference between the measured empty value on the 11.07.17 and 19.02.18.

Table 4.7 – *Table of the levelmeter calibrations of all runs. Presented are the measured values of the empty and full levelmeter. On the 05.01.18 only the empty levelmeter were measured for a first test after the TPC maintenance.*

Level [pF]	11.07.17	16.10.17	05.01.18	19.02.18	10.03.18
Empty:					
Level A	9,055	9.09	20.10	20.07	–
	±0.029	±0.01	±0.02	±0.03	–
Level B	8.643	8.65	8.699	8.723	8.668
	±0.002	±0.01	±0.001	±0.001	±0.001
Level C	9.369	9.40	9.407	9.392	9.377
	±0.001	±0.01	±0.001	±0.001	±0.001
Level D	10.100	10.12	10.120	10.100	10.100
	±0.001	±0.01	±0.001	±0.001	±0.001
Buffer	11.330		9.45	9.311	–
	±0.037		±0.02	±0.028	–
Full:					
Level A	14.79	14.73	–	22.53	–
	±0.03	±0.3	–	±0.17	–
Level B	14.11	14.06	–	14.14	14.16
	±0.04	±0.03	–	±0.03	±0.03
Level C	14.83	14.80	–	14.87	14.84
	±0.03	±0.03	–	±0.05	±0.04
Level D	15.62	15.52	–	15.57	15.61
	±0.05	±0.05	–	±0.06	±0.05
Buffer	17.420		–	16.56	–
	±0.005		–	±0.01	–

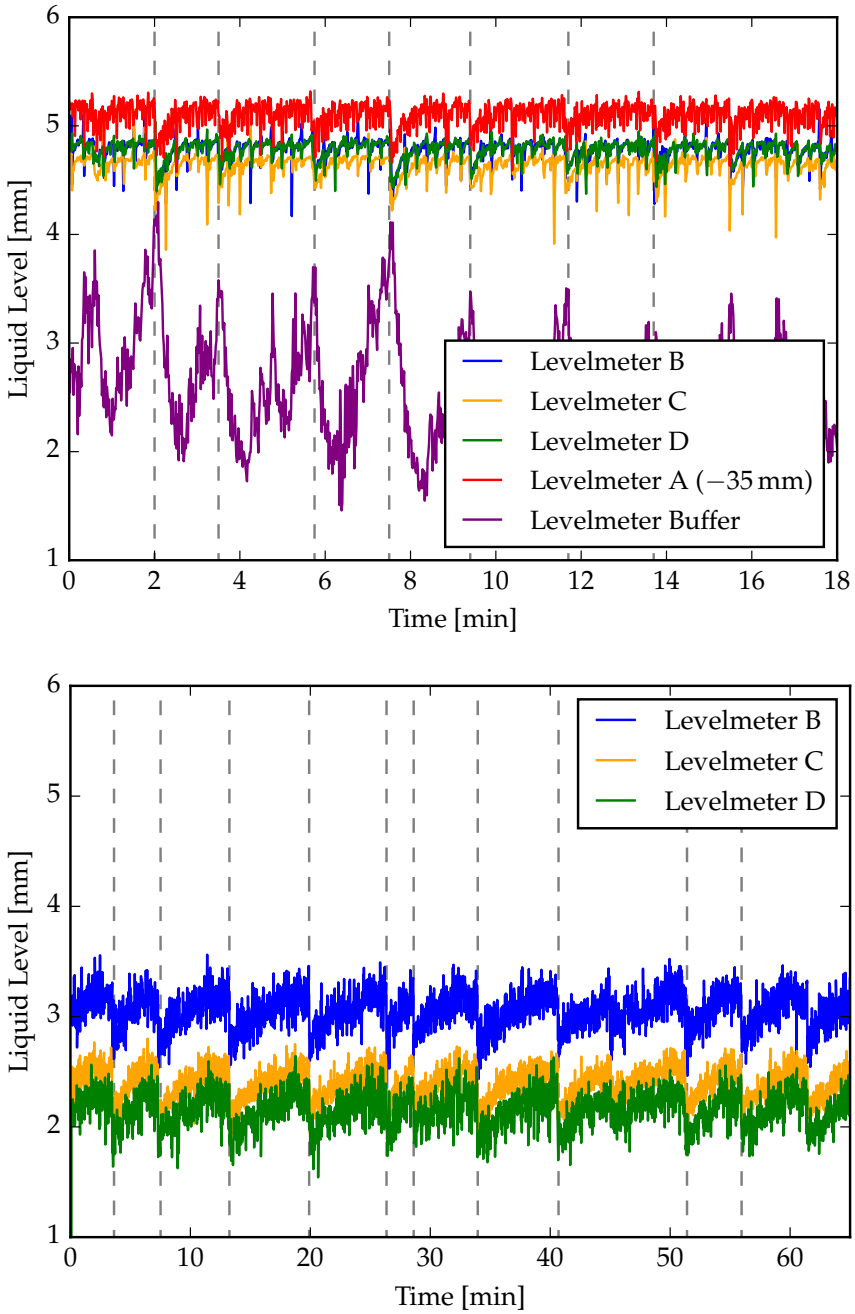

Figure 4.25 – *Comparison of the level fluctuations during the test run in July 2017 (12.7.17, 15:25 till 15:43) with the old spillway and the ^{37}Ar run in March 2018 (06.03.18, 9:10 till 10:15) with the new v-cut spillway. Both plots are showing the measured liquid level, calculated according to equation (2.2) on page 38 versus time (Please note the different timescales). The scale of the liquid level represents the 5 mm gap between anode and gate mesh. The colored graphs show the different levelmeter like stated in the plot legends. The liquid level of the buffer levelmeter was shifted by an offset of −35 mm in order to fit into the plot. The gray dashed lines indicate which level fluctuations were selected for the analysis. The "spiky" appearance of levelmeter B,C,D in the July 2017 run is caused by a defect of UTI-1 which was fixed later. In the lower plot the levelmeter A and the buffer levelmeter are missing because UTI-2 failed during the March 2018 run. The thermodynamic conditions during these measurements are shown in Figure 4.26.*

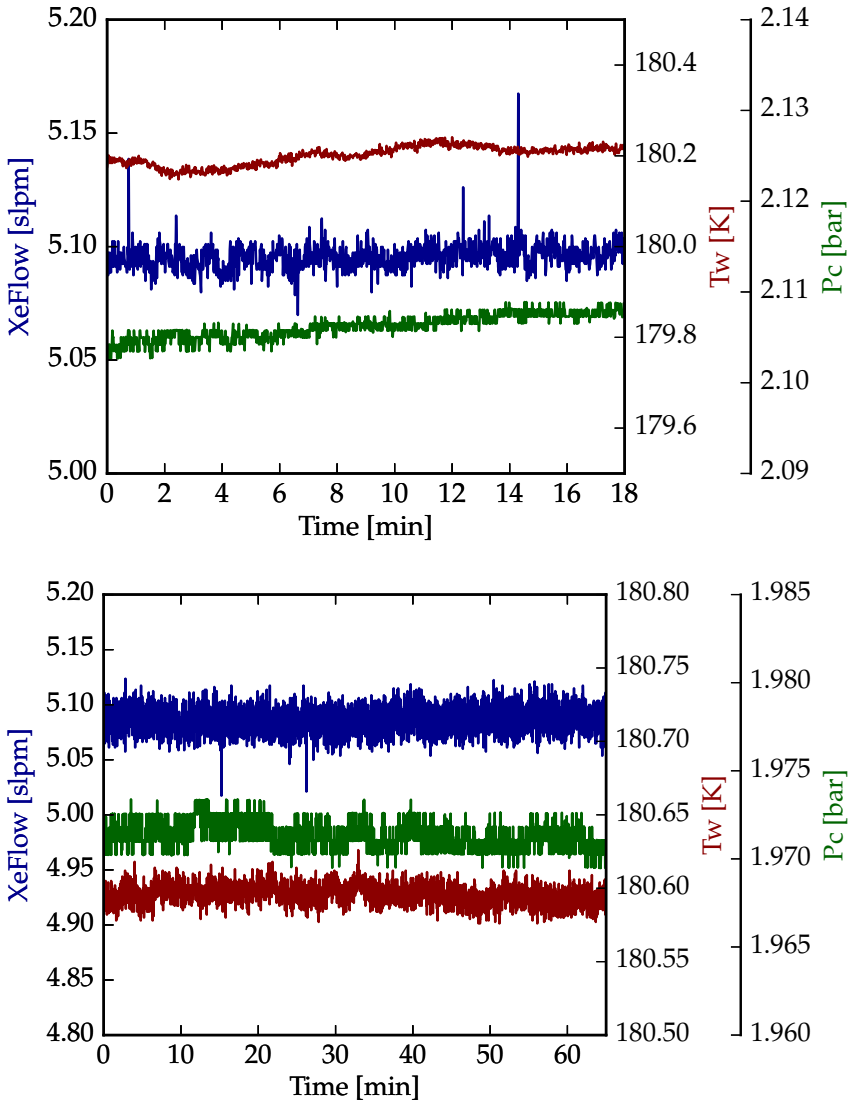

Figure 4.26 – *Thermodynamic conditions during the level measurements July 2017 and March 2018 presented in Figure 4.25. In blue the Xenon recirculation flow (XeFlow), in green the pressure (Pc) and the temperature of the TPC chamber (Tw) in red measured at TPCwidefloor (see Figure 2.5 on page 36) versus time are plotted (Please note the different scales of the two plots).*

CHAPTER 5

CONCLUSIONS AND OUTLOOK

The results of this thesis demonstrated that it is feasible to perform a spatial uniform, ultra-low energy calibration of LXe TPCs using the isotope ^{37}Ar. The measurements of this thesis were carried out with the MainzTPC and the isotope ^{37}Ar was produced in cooperation with the Nuclear Chemistry of the Johannes Gutenberg-Universität Mainz.

In order to achieve these results the MainzTPC was rebuild after a NR measurement at the neutron time-of-flight facility nELBE and the capability of the detector to measure the low energetic signals of ^{37}Ar was studied. In this context an occurrence of a new background contribution caused by impurities led to an extensive maintenance of the MainzTPC and its gas-system.

During this maintenance several hardware issues were fixed. Among others the old spillway for the liquid xenon level adjustment was replaced. With the new spillway an attempt was made to suppress liquid level fluctuations in side the TPC which worsens the overall S_2 resolution of the detector. Unfortunately the analysis showed that the overall stability of the detector's liquid level did not improve.

Further, a procedure for a defined injection of ^{37}Ar was developed, using a subsection of the MainzTPC gas-system. This so-called dosimetry branch is equipped with a PMT for an estimate of the ^{37}Ar activity and several by intermediate valves separated volumes allowing a precise and well controlled dosing of the calibration gas activity. Moreover it was demonstrated that the basic dosing and filling procedure works.

In order to define the analysis strategy as well as some data quality cuts for the ^{37}Ar measurement, initial calibration measurements with the MainzTPC were performed and several aspects of the detector were studied. A method for the xy-position reconstruction was analyzed qualitatively and a calibration of the drift time according to the "area fraction top" parameter was calculated. Moreover, based on these measurements a first S_1 signal charge prediction for the 2.8 keV transition of ^{37}Ar was given.

The ^{37}Ar measurement was performed during the March run. Unfortunately an issue on the field cage did not allow to perform the measurement with drift field. Nevertheless the measurements were performed without field using only the primary scintillation signal of LXe. The results of these measurements were enough to demonstrated that after the injection of the ^{37}Ar the trigger rate of the MainzTPC increased

and that the 2.8 keV transition can be observed. Furthermore the spatial distribution of the ^{37}Ar along the z-axis of the MainzTPC was studied using the calibration of the area fraction top parameter. A broad spatial distribution over the entire MainzTPC volume was observed, proofing a diffusion of the ^{37}Ar into the liquid xenon. This result is especially important for a usage of ^{37}Ar in ton scale detectors and opens the way for having it as a calibration source in the XENON1T experiment.

Also the just recently published paper [B+17] about a ^{37}Ar calibration of the dual-phase LXe TPC *PIXeY* demonstrates the interest of the WIMP DM community and the relevance of this thesis.

Due to the low transition energies of ^{37}Ar this thesis also demonstrates the current limits of the MainzTPC. In the following some suggestions which might be beneficial for future studies are given.

Since the main design goal of the MainzTPC is to improve the knowledge about the low energy scintillation properties of liquid xenon, the most important part which needs to be improved is the **signal read-out** and data processing. The MainzTPC is lacking of well suited read-out and amplification chain. Already during the end phase of this work first ideas were discussed in cooperation with the PRISMA Detector Laboratory and a first possible solution was sketched. Due to the diverse properties of the two DAQ boards, also two different types of amplifier are required. A high bandwidth amplifier for the SIS3305 and a high gain amplifier for the SIS3316 seem to be the most appropriated solution. Furthermore the passive splitter of the MainzTPC has to be replaced. In order to enhance small signal without loosing the ability to record large signals it might be worth to study passive splitters with an asymmetric signal split of 0.1/0.9 or 0.2/0.8. This new passive splitter should then be followed by a high bandwidth active splitter in order to make use of the two different amplifiers for the fast and slow DAQ board. Once set-up this would also allow to improve the peak finding of the MainzTPC by simply rolling the peak finding algorithm over the summed waveform instead of the individual ones.

The **liquid level fluctuations** of the MainzTPC remain an unsolved problem. While the presented observations and analysis of this thesis lead to the conclusion that the fluctuation are most likely not caused by a surface tension effect, no further evidences about their true origin were found. It is hard to propose any improvements for the future. Maybe a change of the level system of the MainzTPC to a diving bell system, or setting the liquid level via a LXe volume displacement system will lead to a more stable level.

In an improved version of the MainzTPC one should change the concept of the **levelmeter** readout. UTI-2 caused problems very often in the past. These problems most likely are coming from the fact that the common return is split and fed through two distinct feed-throughs, whereof one goes to the buffer levelmeter and one goes to levelmeter A. Since every UTI evaluation board can read-out up to 4 different capacities one could propose to measure all TPC levelmeter with a single board. This would mean that a conversion of the measured UTI value into a real capacitance is not possible any longer. However this is not required for measuring the height of the liquid level since a linear reference factor is canceled out as can be see in equation (2.2) on page 38. Further would this allow to place the two UTI evaluation boards into two

separate steel boxes which might improve the stability of the measurement.

Beside these aspects one last thing worth to investigate is if the isomeric states ^{129m}Xe, ^{131m}Xe and ^{83m}Kr can be produced by the irradiation of natural xenon and krypton (or other elements) with thermal neutrons of the TRIGA Mark-II. This would allow to diffuse higher energetic calibration gases into the MainzTPC and therefore offers the opportunity to set-up energy calibration curves in the combined energy scale and to estimate the relative Q.E. value of the eight APDs properly. Once these measurements have become more routine and well established, this could also be offered as a students project for the F-Praktikum. It would give the students some insight into a complex experiment and would therefore improve the academic education of the Johannes Gutenberg-Universität Mainz.

ACKNOWLEDGMENTS

Writing a master thesis is accompanied with fun, excitement, curiosity and happiness; but also with throwbacks, anger and sadness. Therefore it is important to work with people who support and back each other. In this context I would like to thank Professor Uwe Oberlack for supporting my with thought-provoking discussions and his valuable help during throwbacks. Further I would like to thank him for his trust in me before and during my Master Thesis.

Moreover, I have to thank the entire Mainz XENON group for being not just simply colloquies but also friends who supported me a lot during different phases of my thesis. I would like to especially thank Christopher Hils for his help during the maintenance of the MainzTPC and the gas-system as well as his helpfulness regarding the different measurement runs. Additionally I would like to thank Pierre Sissol for teaching me the operation of the MainzTPC, its DAQ and data format during his final phd-phase.

In addition, I have to thank Dr. Geppert and his team of the Nuclear Chemistry of the Johannes Gutenberg-Unversität Mainz for the consulting and irradiation of the ^{36}Ar sample; and I would also like to thank the PRISMA Detector Laboratory for their help with the next generation of the Detector Lab amplifiers and their support of the MainzTPC maintenance through the usage of their cleanroom.

Finally I want to thank Dr. Arnd Junghans and Dr. Roland Beyer of the Helmholtz Forschungszentrum Dresden-Rossendorf for offering me the opportunity to help them with a total cross-section measurement of natural xenon at the neutron time-of-flight facility nELBE; and for giving me an insight into this interesting and exciting experiment.

APPENDIX

A. THEORY CHAPTER:

Gaussian Error Propagation of Equation (2.7) (^{37}Ar activity):
Only the parameters with the biggest uncertainty were used.

$$\Delta A_{\mathrm{Ar37}}(t) = \sqrt{\left(\frac{\mathrm{d}A_{\mathrm{Ar37}}(t)}{\mathrm{d}N^0_{\mathrm{Ar36}}}\Delta N^0_{\mathrm{Ar36}}\right)^2 + \left(\frac{\mathrm{d}A_{\mathrm{Ar37}}(t)}{\mathrm{d}\sigma_{\mathrm{Ar36}}}\Delta\sigma_{\mathrm{Ar36}}\right)^2 + \left(\frac{\mathrm{d}A_{\mathrm{Ar37}}(t)}{\mathrm{d}\sigma_{\mathrm{Ar37}}}\Delta\sigma_{\mathrm{Ar37}}\right)^2} \tag{5.1}$$

with

$$\begin{aligned}
\frac{\mathrm{d}A_{\mathrm{Ar37}}(t)}{\mathrm{d}N^0_{\mathrm{Ar36}}} &= \ln(2)\cdot\frac{\Delta N^0_{\mathrm{Ar36}}}{\tau^{\mathrm{Ar37}}_{1/2}}\frac{\sigma_{\mathrm{Ar36}}}{\sigma_{\mathrm{Ar37}}-\sigma_{\mathrm{Ar36}}}\cdot\left(e^{-\sigma_{\mathrm{Ar36}}F_{\mathrm{n}}t}-e^{-\sigma_{\mathrm{Ar37}}F_{\mathrm{n}}t}\right)\\
\frac{\mathrm{d}A_{\mathrm{Ar37}}(t)}{\mathrm{d}\sigma_{\mathrm{Ar36}}} &= \ln(2)\cdot\frac{N^0_{\mathrm{Ar36}}}{\tau^{\mathrm{Ar37}}_{1/2}}\left[\frac{1}{\sigma_{\mathrm{Ar37}}-\sigma_{\mathrm{Ar36}}}\cdot\left(e^{-\sigma_{\mathrm{Ar36}}F_{\mathrm{n}}t}-e^{-\sigma_{\mathrm{Ar37}}F_{\mathrm{n}}t}\right)+\right.\\
&\quad+\frac{\sigma_{\mathrm{Ar36}}}{(\sigma_{\mathrm{Ar37}}-\sigma_{\mathrm{Ar36}})^2}\cdot\left(e^{-\sigma_{\mathrm{Ar36}}F_{\mathrm{n}}t}-e^{-\sigma_{\mathrm{Ar37}}F_{\mathrm{n}}t}\right)+\\
&\quad\left.+\frac{\sigma_{\mathrm{Ar36}}}{\sigma_{\mathrm{Ar37}}-\sigma_{\mathrm{Ar36}}}\cdot\left(-F_{\mathrm{n}}t\,e^{-\sigma_{\mathrm{Ar36}}F_{\mathrm{n}}t}-e^{-\sigma_{\mathrm{Ar37}}F_{\mathrm{n}}t}\right)\right]\\
\frac{\mathrm{d}A_{\mathrm{Ar37}}(t)}{\mathrm{d}\sigma_{\mathrm{Ar37}}} &= \ln(2)\cdot\frac{N^0_{\mathrm{Ar36}}}{\tau^{\mathrm{Ar37}}_{1/2}}\left[-\frac{\sigma_{\mathrm{Ar36}}}{(\sigma_{\mathrm{Ar37}}-\sigma_{\mathrm{Ar36}})^2}\cdot\left(e^{-\sigma_{\mathrm{Ar36}}F_{\mathrm{n}}t}-e^{-\sigma_{\mathrm{Ar37}}F_{\mathrm{n}}t}\right)+\right.\\
&\quad\left.+\frac{\sigma_{\mathrm{Ar36}}}{\sigma_{\mathrm{Ar37}}-\sigma_{\mathrm{Ar36}}}\cdot\left(e^{-\sigma_{\mathrm{Ar36}}F_{\mathrm{n}}t}+F_{\mathrm{n}}t\,e^{-\sigma_{\mathrm{Ar37}}F_{\mathrm{n}}t}\right)\right]
\end{aligned}$$

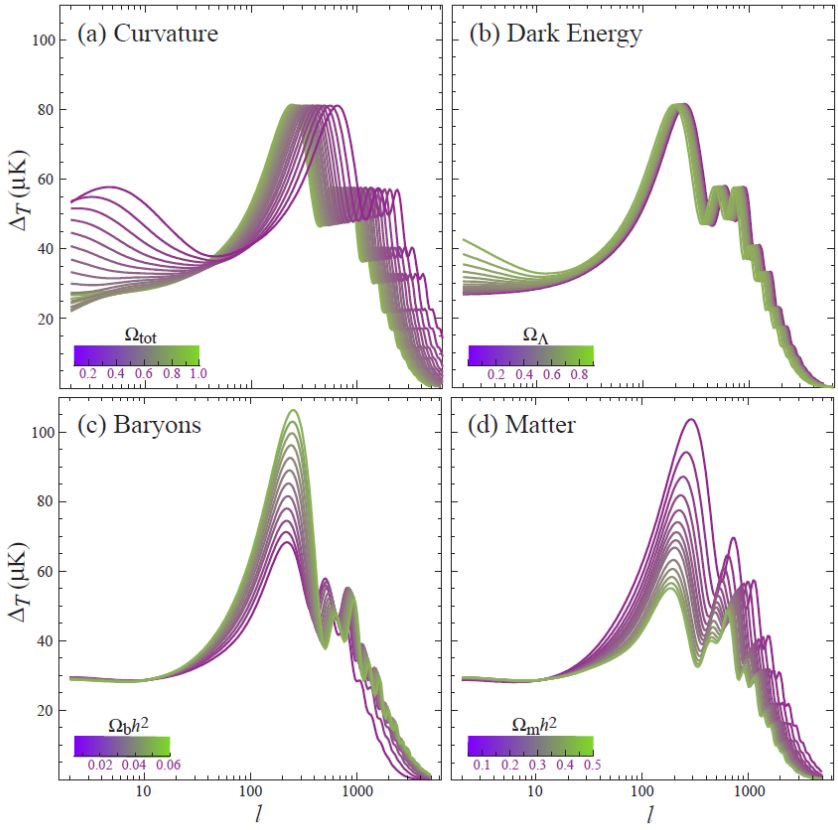

Figure 5.1 – *Variation of the acoustic peak position, depending on different cosmological parameter [HD02].*

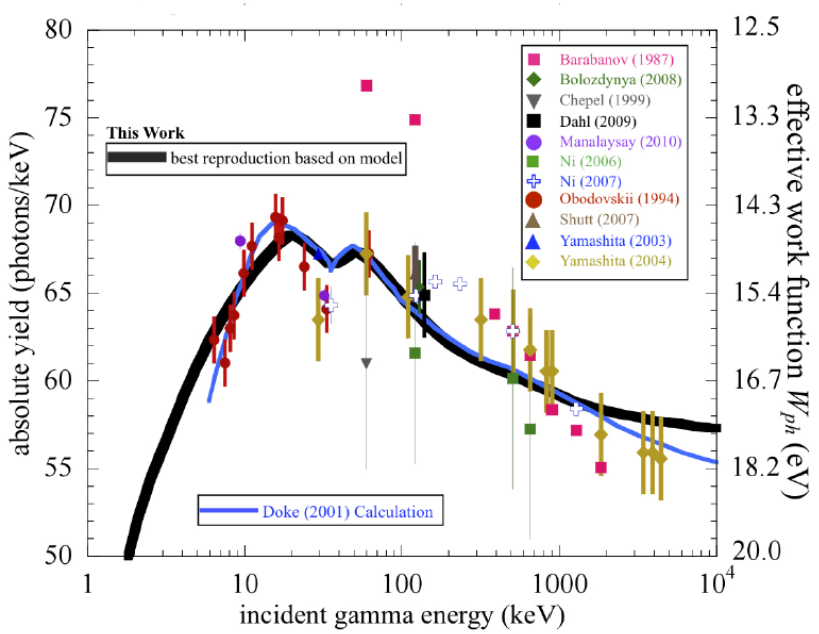

Figure 5.2 – *Absolute scintillation yield of liquid xenon predicted by the nest model compared to a variety of measurements for incident γ-rays [S+11].*

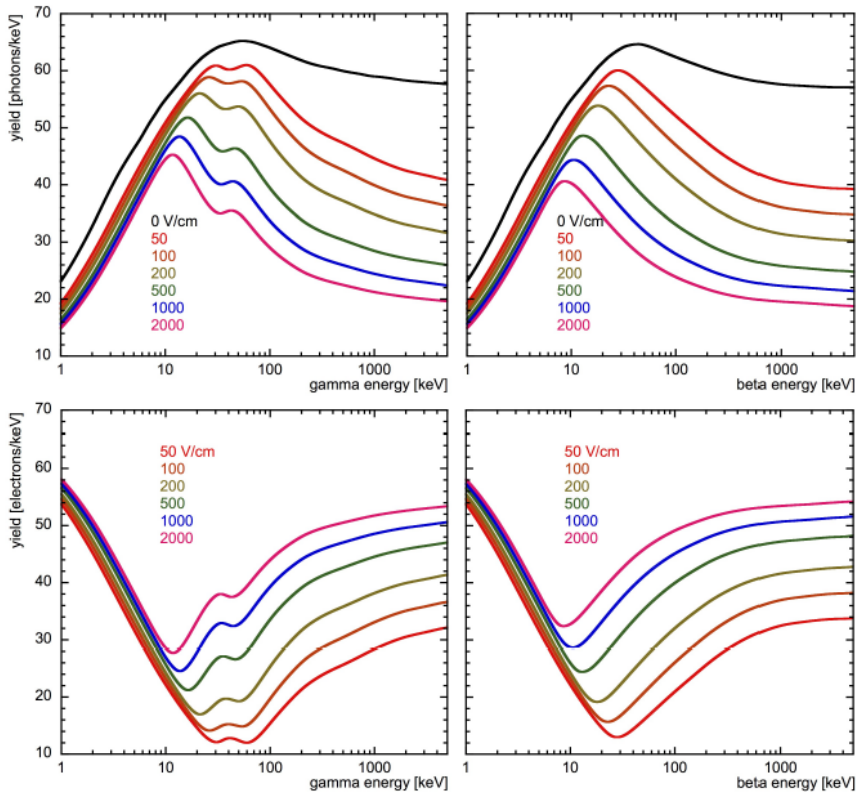

Figure 5.3 – *Absolute charge and scintillation yield for incident γ-rays and electrons for different drift field settings. The upper row presents the light and the lower row the charge yield [S+13].*

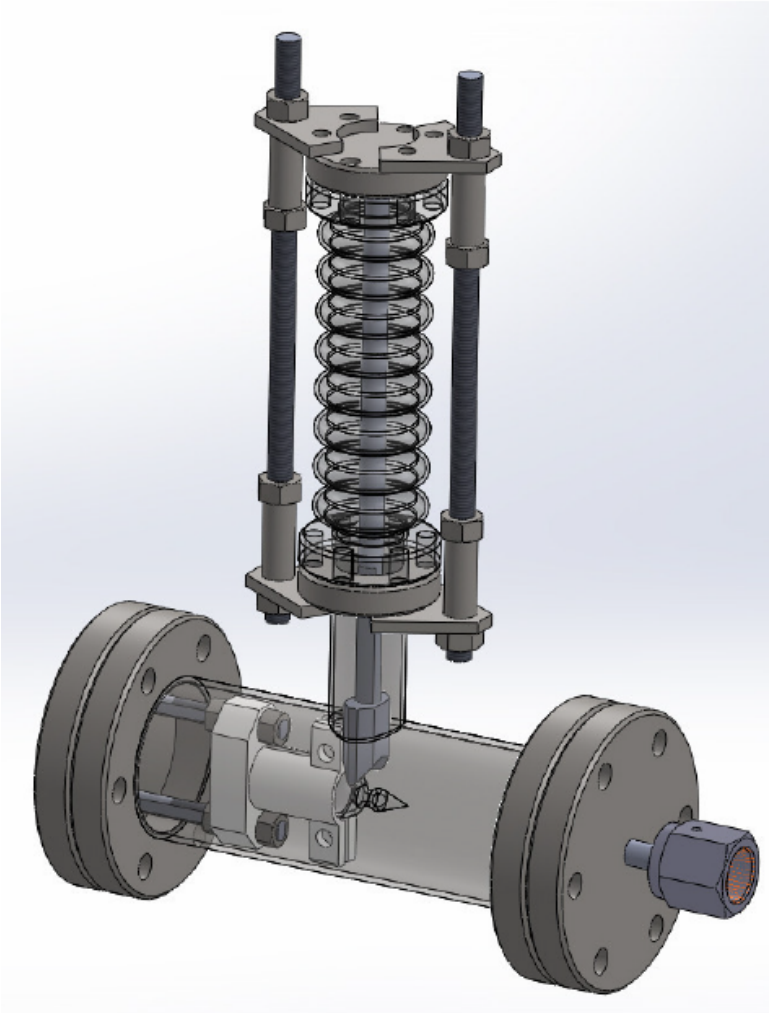

Figure 5.4 – *CAD drawing of the guillotine mechanism. In the center of the CF-40 pipe the quartz ampule together with the PEEK holder is shown. Above the quatz ampule is the sharpened edge which cuts of the ampule head when it is pushed down. This mechansim was designed by Christopher Hils in [Hil14].*

B. THE MAINZTPC EXPERIMENT CHAPTER:

C. MEASUREMENTS AND RESULTS CHAPTERS:

Table 5.1 – *Table of the mean values and standard deviations for the different PMT single photo-electron calibration fits. Presented are the values which were estimated based on the fits shown in Figure 5.5, 5.6 and 5.7. Further are if possible the area ratios between the area of the pedestal and the single photo-electron peak stated.*

Run	PMT	μ_{pe} [pC]	σ_{pe} [pC]	μ_{spe} [pC]	σ_{spe} [pC]	χ^2/ndof	area ratio
July	Top (1000 V)	0.308 ± 0.006	0.510 ± 0.007	2.184 ± 0.166	2.551 ± 0.700	6770/984	–
	Bottom (950 V)	-0.002 ± 0.001	0.318 ± 0.001	0.991 ± 0.020	0.76 ± 0.014	1071/819	0.177
October	Top (1000 V)	0.0001 ± 0.0005	0.3129 ± 0.0004	1.858 ± 0.0136	0.900 ± 0.013	3399/893	0.047
	Bottom (1000 V)	-0.0020 ± 0.0007	0.3695 ± 0.0005	1.423 ± 0.032	0.900 ± 0.013	1247/847	0.050
March	Top (1000 V)	0.0046 ± 0.0009	0.5394 ± 0.0006	4.149 ± 0.036	3.037 ± 0.039	5100/849	0.10
	Bottom (1000 V)	0.3261 ± 0.0009	0.4437 ± 0.0006	3.195 ± 0.158	2.177 ± 0.079	3731/705	–

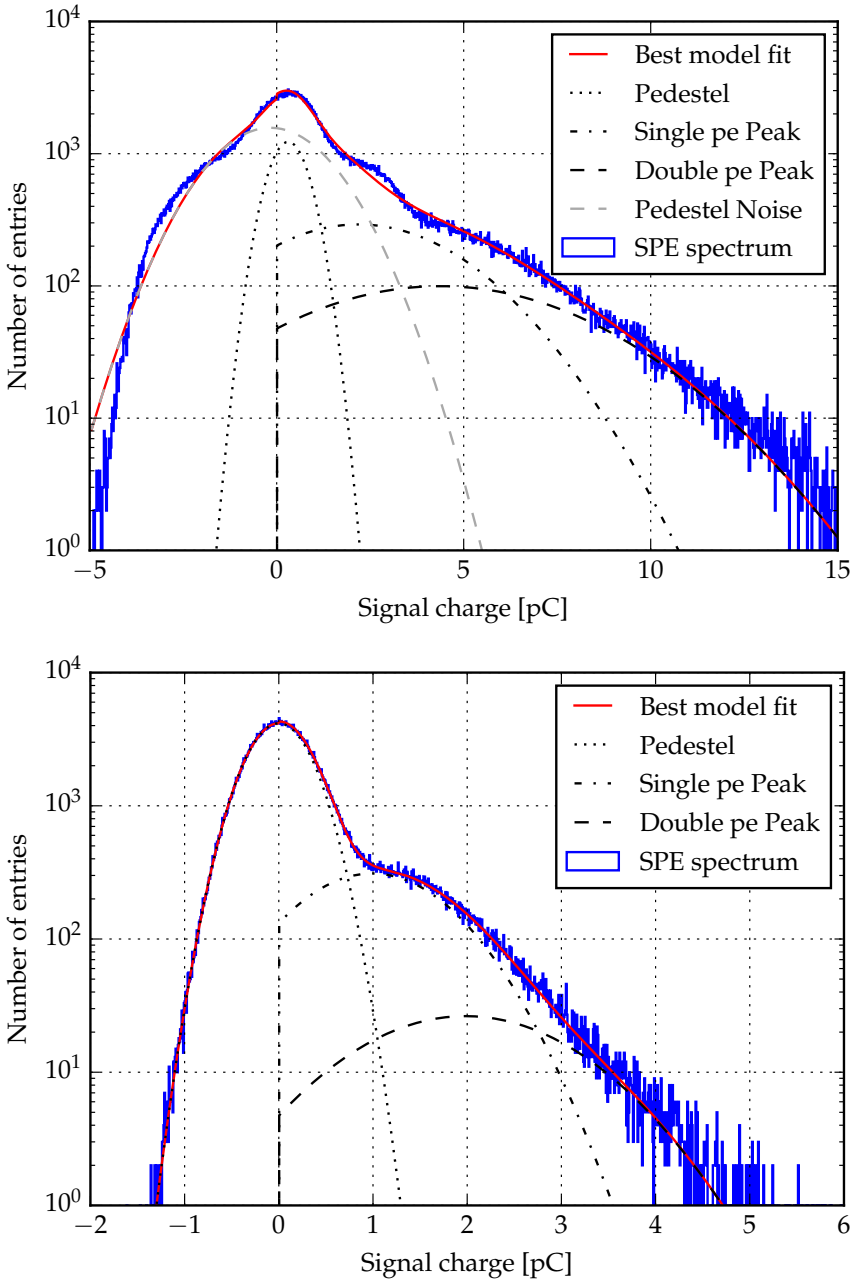

Figure 5.5 – *Single photo electron calibration measurements for the amplified top and bottom PMT with the July 2017 run read-out setting. The upper picture shows the calibration measurement of the top PMT, while the lower plot shows the measurement with the bottom PMT. The top PMT was amplified with the Detector Lab amplifier 1. and biased with 1000 V and the bottom PMT was amplified with the KPH amplifier 1. and biased with 950 V. For the fit of the top PMT the fit model in equation (4.2) was extended by another modified normal distribution $N'(A_{noise}, \mu_{noise}, \sigma_{noise})$ in order to model the noise shoulder of the pedestal peak. This noise was induced by the on-board DC-DC converter of the amplifier which broke after the July measurements.*

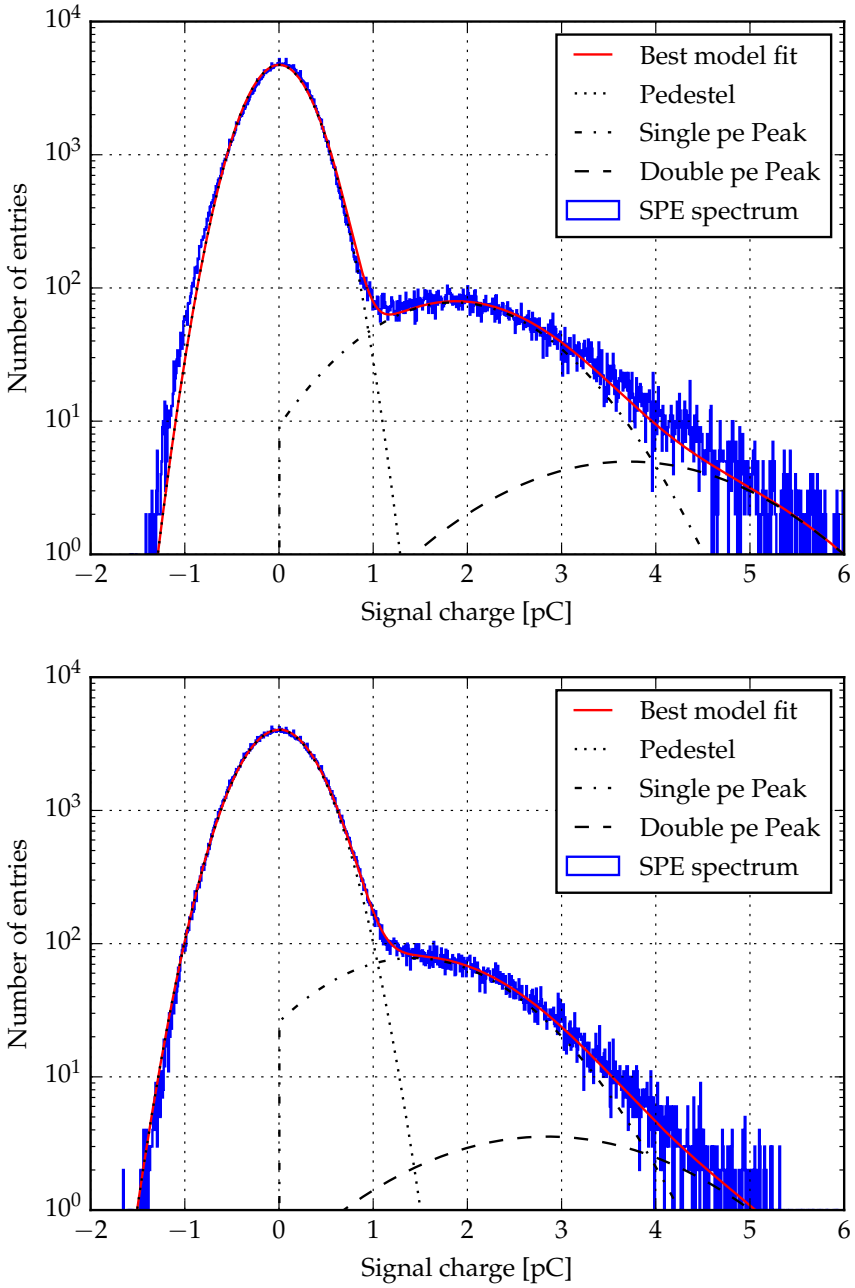

Figure 5.6 – *Single photo electron calibration measurements for the amplified top and bottom PMT with the March 2018 run read-out setting. The upper picture shows the calibration measurement of the top PMT, while the lower plot shows the measurement with the bottom PMT. Both PMTs were biased with 1000 V. The top PMT was amplified with the Detector Lab amplifier 1. and the bottom PMT with the second Detector Lab amplifier.*

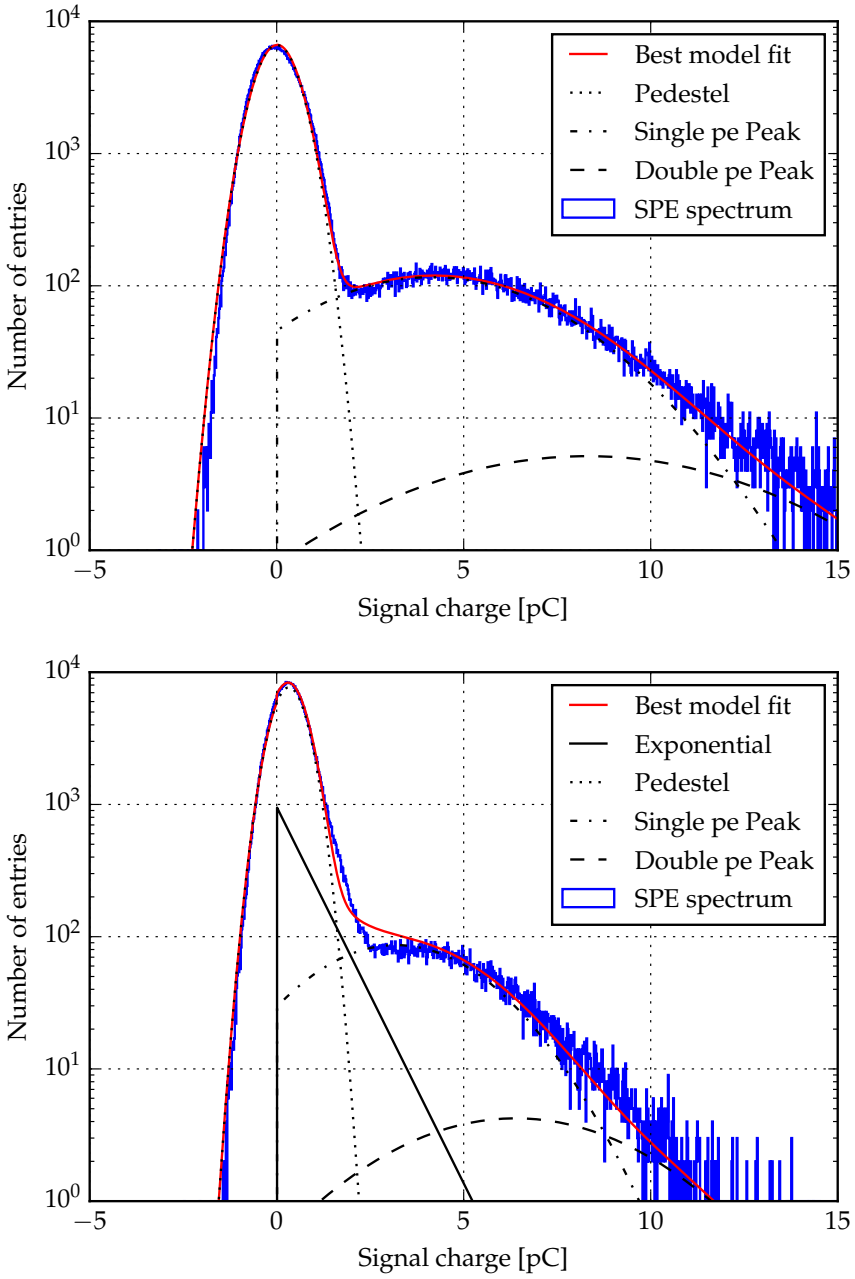

Figure 5.7 – *Single photo electron calibration measurements for the amplified top and bottom PMT with the March 2018 2017 run read-out setting. The upper picture shows the calibration measurement of the top PMT, while the lower plot shows the measurement with the bottom PMT. Both PMTs were biased with 1000 V. The top PMT was amplified with the Detector Lab amplifier 1. and the bottom PMT with the second Detector Lab amplifier. For the fit of the bottom PMT the second term of fit model specified in equation (4.2) was modified with an additional exponential function* $A \cdot \exp(-m \cdot x)$ *which shall take care of the extended noise between pedestal and single photo-electron peak. Although this additionally modified model does not catch the whole spectrum the single photo-electron peak is well represented through its normal distribution.*

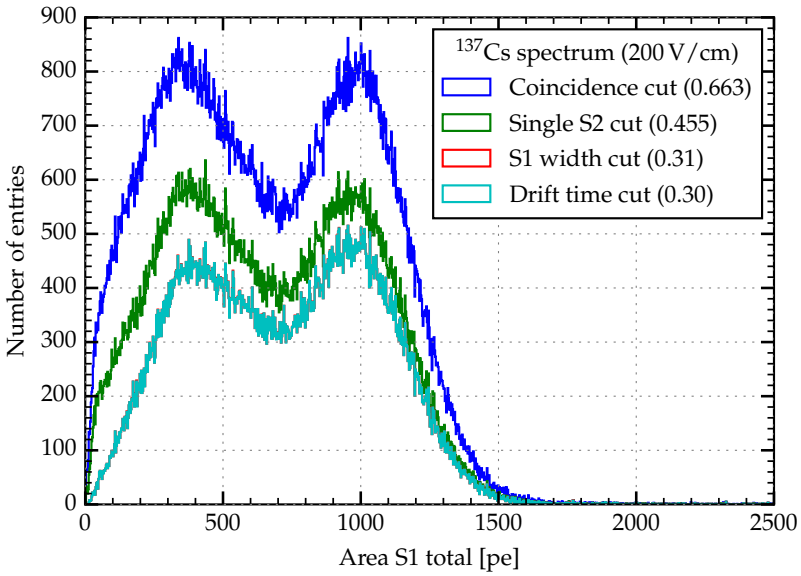

Figure 5.8 – *^{137}Cs energy spectrum for the 200 V/cm drift field measurement during the October 2017 run. Presented is the number of entries versus the total S_1 area in photo-electrons. The colored spectra represent the energy spectrum with an accumulated number of quality cuts. The number in the round brackets corespondents to the fraction of waveforms which are left over compared to the initial number of waveforms. Initially 496885 waveforms were recorded. Compared to the ^{137}Cs spectrum measured with a drift field of 800 V/cm the full-energy-peak is well separated from the Compton regime.*

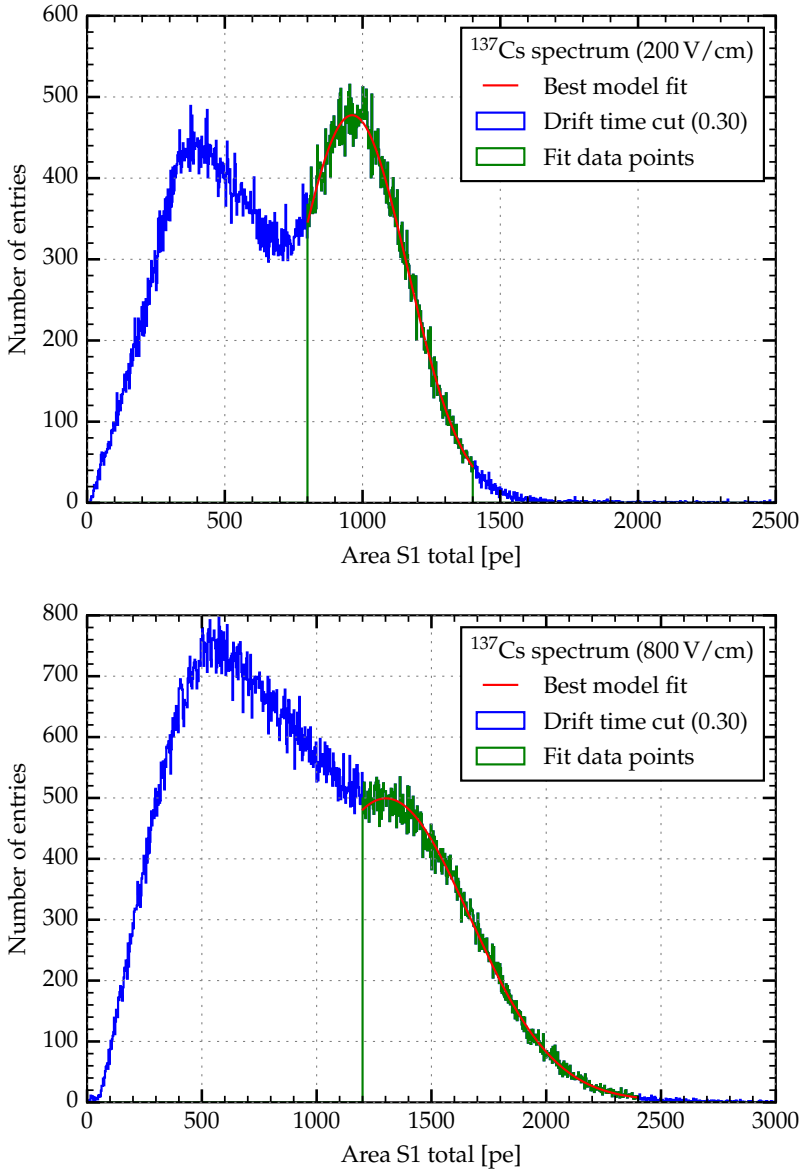

Figure 5.9 – *Fit of the ^{137}Cs full-energy-peak in the 200 V/cm and 800 V/cm measurement taken during the October and July 2017 run respectively.*

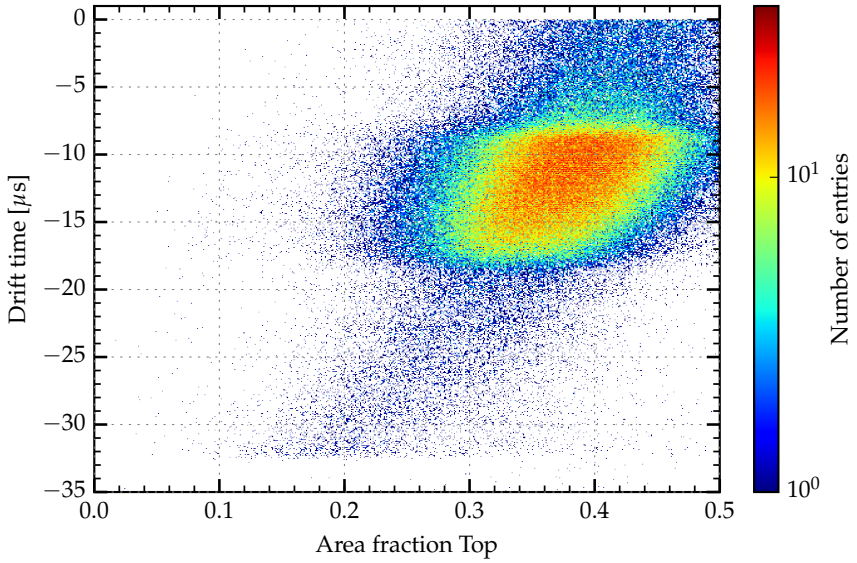

Figure 5.10 – *Drift time versus area fraction top of the collimated ^{137}Cs source measurement with a drift field of 200 V/cm, taken during the October 2017 run. The area fraction of the top PMT increased compared to the July run measurement presented in Figure 4.8.*

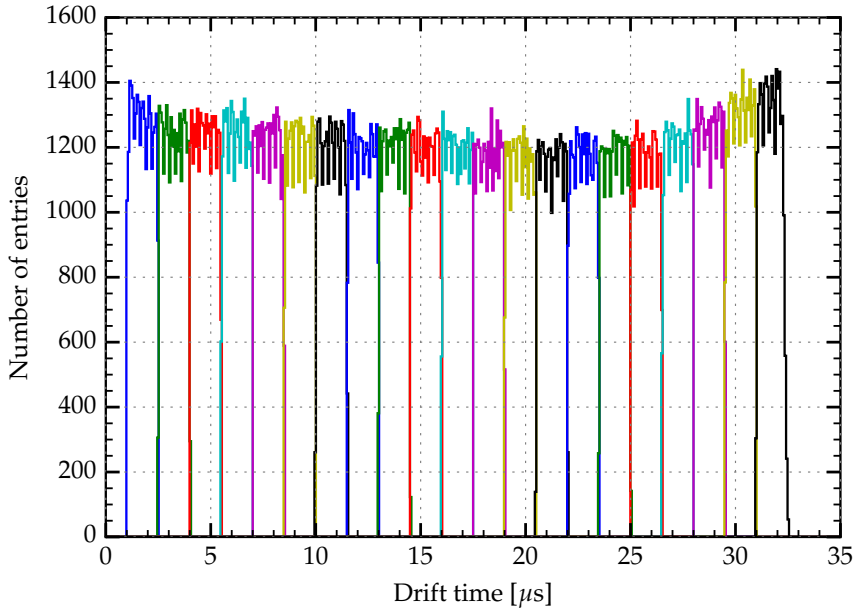

Figure 5.11 – *Drift time slices for the drift time calibration of the area fraction top parameter.*

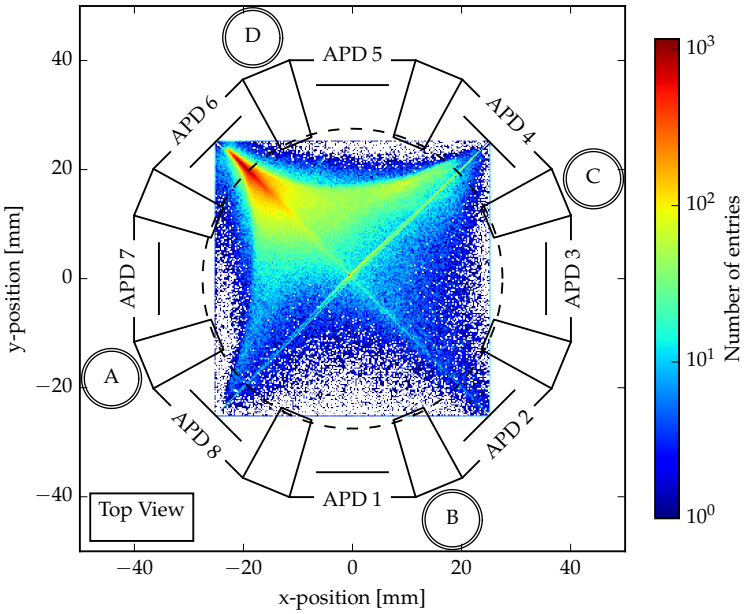

Figure 5.12 – *XY-position reconstruction pattern of the even numbered APDs, when the pseudo Q.E. values of Table 4.4 are applied.*

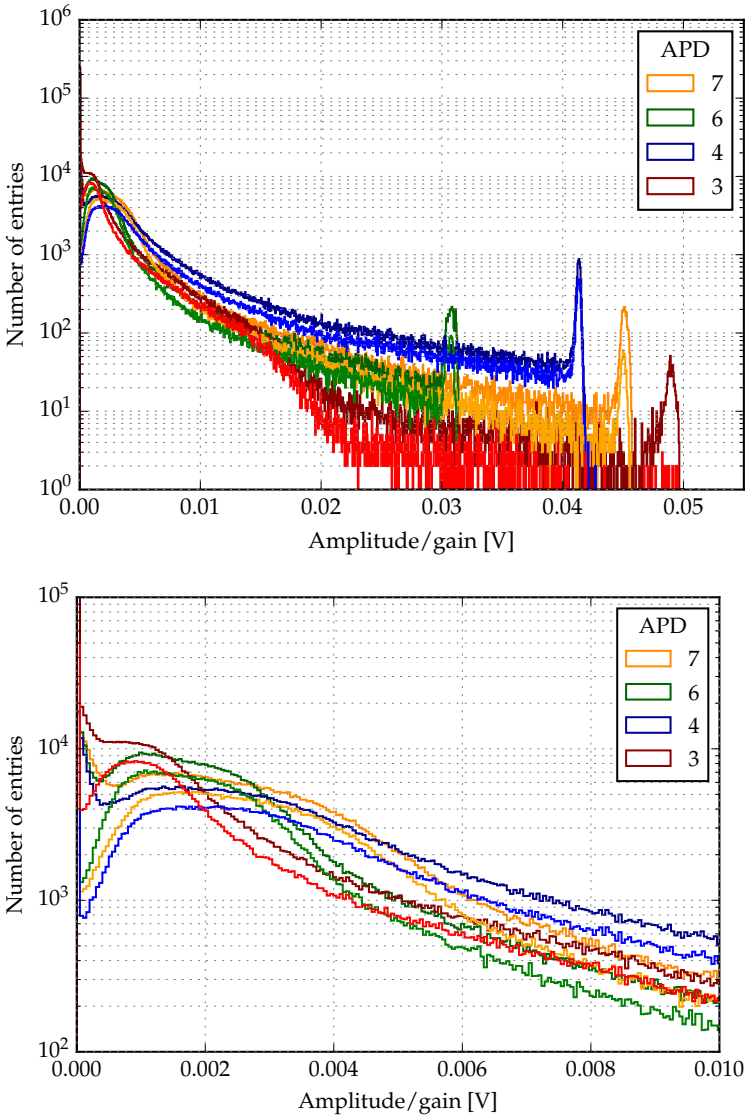

Figure 5.13 – *APD energy spectrum of a uncollimated ^{133}Ba source measured with the APDs 3,4,6 and 7. The number of entries versus the measured signal amplitude (charge) divided by the gain of each APD are plotted. The upper plot shows the spectrum over the hole dynamic range of the SIS3316 while the lower plot focuses on the full energy peaks of ^{133}Ba. The dark colored spectra represent the data without any further cuts, while the brighter colored spectra were cut according to the full energy peaks of the ^{133}Ba spectrum presented in Section 4.3.*

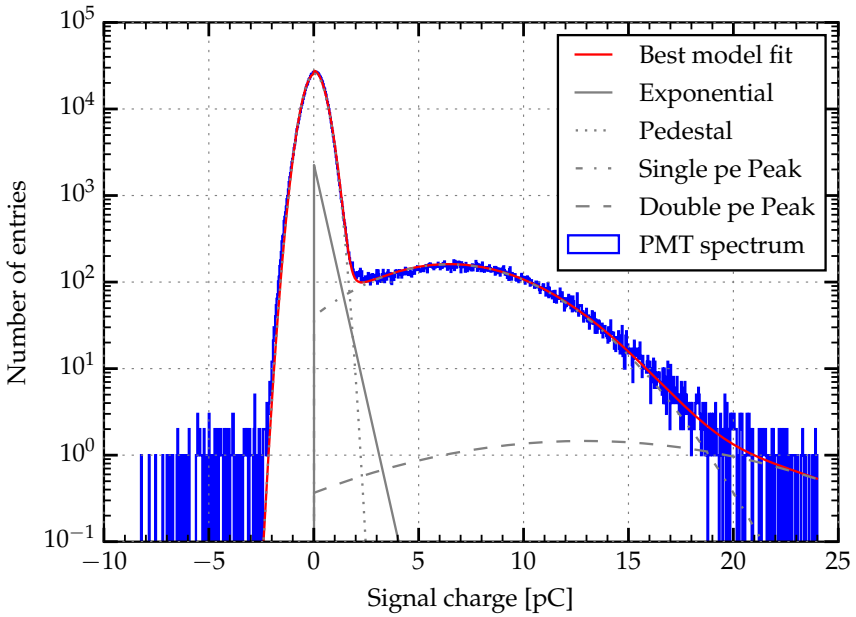

Figure 5.14 – *Calibration of the dosimetry PMT. Presented is the measured single photo-electron spectrum together with the best model fit and the individual contribution of the fit function. The fit yielded for the pedestal* $\mu_{pe} = (0.040 \pm 0.001)\,pC$; $\sigma_{pe} = (0.488 \pm 0.001)\,pC$ *and for the single photo-electron peak* $\mu_{spe} = (6.460 \pm 0.0364)\,pC$; $\sigma_{spe} = (3.884 \pm 0.031)\,pC$ *with a* $\chi^2/ndof$ *of 2930/790 and a area ratio between the two peaks of 0.050.*

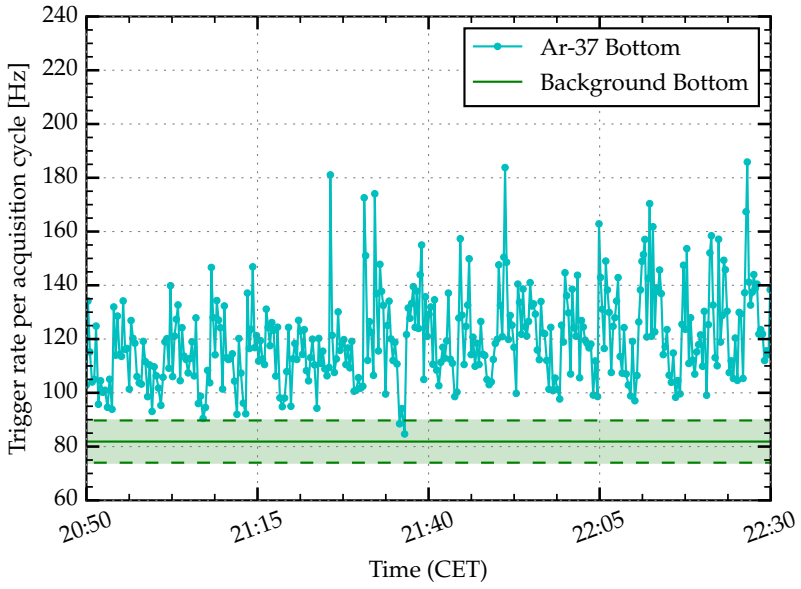

Figure 5.15 – *Excerpt of the bottom PMT triggered* ^{37}Ar *measurement presented in Figure 5.16. The data points had been interpolated linearly.*

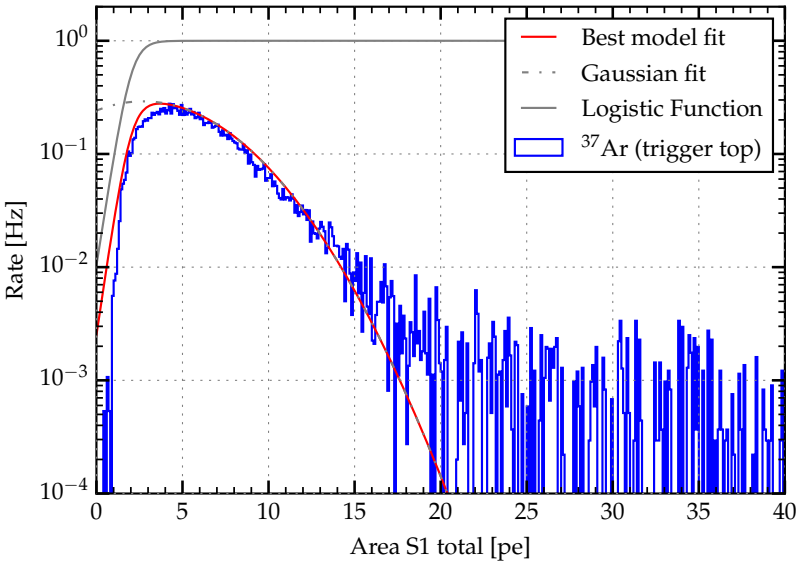

Figure 5.16 – *Fit of the background corrected ^{37}Ar spectrum.*

BIBLIOGRAPHY

[A+] E. Altstadt et al. *nELBE: Neutron time-of-flight experiment at ELBE*. Helmholtz Zentrum Dresden Rossendorf. https://www.hzdr.de/db/Cms?pNid=317,16.04.2018.

[A+71] Luis W. Alvarez et al. A high precision particle detector using noble liquids. *Letter to Nature*, 1971.

[A+00] D. N. Abdurashitov et al. ^{37}Ar yield from irradiated calcium oxide under thermal treatment. *NUCLEAR EXPERIMENTAL TECHNIQUES*, 43(3):287–290, 2000.

[A+07] E. Aprile et al. Observation of anticorrelation between scintillation and ionization for mev gamma rays in liquid xenon. *Physical Review B*, 76(014115), 2007.

[A+12] E. Aprile et al. The XENON100 Dark Matter Experiment. *Astropart. Phys.*, 35:673–590, 2012.

[A+13] D. S. Akerib et al. The large underground xenon (lux) experiment. *Nuclear Inst. and Methods in Physics Research A*, 704:111–126, 2013.

[A+16a] D. S. Akerib et al. Tritium calibration of the LUX dark matter experiment. *Phys. Rev. D*, 93(072009), 2016.

[A+16b] E. Aprile et al. Physics reach of the xenon1t dark matter experiment. *Journal of Cosmology and Astroparticle Physics*, 14. April 2016.

[A+17a] D.S. Akerib et al. ^{83m}Kr calibration of the 2013 LUX dark matter search. *Phys. Rev. D*, 96(112009), 2017.

[A+17b] E. Aprile et al. Results from a calibration of xenon100 using a source of dissolved radon-220. *Phys. Rev. D*, 95(072008), 2017.

[A+17c] E. Aprile et al. The XENON1T dark matter experiment. *EPJ C (submitted)*, 23. August 2017.

[A+17d] E. Aprile et al. First dark matter search results from the xenon1t experiment. 23. November 2017.

[ABMJ81] R. Abjean A. Bideau-Mehu, Y. Guern and A. JohanningGilles. Measurement of the Refractive indices of Neon, Argon, Krypton and Xenon in the 253.7-140.4 nm wavelength range. Dispersion relations and estimated oscillator strengths of the Resoncance lines. *J. Quant. Spectrosc. Radiat. Transfer*, 25(5):395–402, 1981.

[AD10] E. Aprile and T. Doke. Liquid xenon detectors for particle physics and astrophysics. *Reviews of Modern Physics*, 82:2053–2097, July 2010.

[Air] *Enceyclopedia of Airliquide*. https://encyclopedia.airliquide.com, 06.04.2018.

[Ald18] Alderamin. *Artikel-Quckie: Was is der Bullet Cluster?* ScienceBlogs, April 2018. http://scienceblogs.de/alpha-cephei/2018/04/11/artikel-quickie-was-ist-der-bullet-cluster/,15.04.2018.

[Ana] Analog Devices. *Low Distortion Amplifier AD8009*. www.analog.com/media/en/technical-documentation/data-sheet/AD8009.pdf,16.04.2018.

[Ang04] J. Angrik. Katrin Design Report 2004. *FZKA Scientific Report*, 7090, 2004.

[B+06] V. I. Barsanov et al. A technology and facility for extraction, purification, and collection of ^{37}Ar from calcium oxide. *NUCLEAR EXPERIMENTAL TECHNIQUES*, 49(4):454–460, 2006.

[B+07] V. I. Barsanov et al. Artificial neutrino source based on the ^{37}Ar isotope. *PHYSICS OF ATOMIC NUVLEI*, 70(2):300–310, 2007.

[B+11] Marie-Martine Bé et al. Table of radionuclides. *Laoratoire National Henri Becquerel*, 2011.

[B+14] Bastian Beskers et al. A small dual-phase xenon tpc with apd and pmt readout for the study of liquid xenon scintillation. *PoS*, June 2014.

[B+17] E.M. Boulton et al. Calibration of a two-phase xenon time projection chamber with ^{37}Ar source. *JINST*, 12(P08004), August. 2017.

[Bau12] Laura Baudis. Dark Universe. *Elsevier*, page 94–108, 2012.

[Ber10] Gianfranco Bertone. *Particle Dark Matter*. Cambridge University Press, 2010.

[Bes17] Bastian Beskers. "MainzTPC" design and commissioning of a dual-phase xenon time-projection-chamber for studies of the scintillation pulse shape. Doctor of sience, Institut für Physik Joahnnes Gutenberg-Universität Mainz, 2017. xenon.physik.uni-mainz.de/theses.html, 27.03.2018.

[C+95] A. Chan et al. Performance of the HPC calorimeter in DELPHI. *IEEE Transactions on Nuclear Sience*, 42(4):491–498, 1995.

[CA13] V. Chepel and H. Araújo. Liquid noble gas detectors for low energy particle physics. *JINST*, 8, April 2013.

[CAEa] CAEN S.p.A. *A1422*. www.cean.it/csite/CaenProd.jsp?parent=14&idmod=604,16.04.2018.

[CAEb] CAEN S.p.A. *V6533*. www.cean.it/csite/CaenProd.jsp?idmod=657&parent=23,16.04.2018.

[CAE06a] CAEN S.p.A. *DT5800 Desktop Digital Detector Emulator*, October 2006. http://www.caen.it/csite/CaenProd.jsp?idmod=837&parent=59,18.05.2018.

[CAE06b] CAEN S.p.A. *N1145*, October 2006. http://www.caen.it/jsp/Template2/CaenProd.jsp?parent=12&idmod=299,17.04.2018.

[CER] CERN. *ROOT Data Analysis Framework*. https://root.cern.ch, 25.04.2018.

[Col16] Planck Collaboration. Planck 2015 results. XIII. Cosmological parameters. *A&A*, 594(A13), 2016.

[Cow98] Glen Cowan. *Statistical Data Analysis*. Oxford Science Publications, 1998.

[E+01] V. Eckardt et al. Calibration of the star forward time projection chamber with krypton-83m. *arXiv:nucl-ex/0101013*, January 2001.

[ESA] ESA. *Planck*. https://www.esa.int/Our_Activities/Space_Science/Planck/,28.04.2018.

[Fen10] Jonathan L. Feng. Dark Matter Candidates from Particle Physics and Methods of Detection. *Annu. Rev. Astron. Astrophys*, 48:495–545, 2010.

[GBS05] Dan Hooper Gianfranco Bertone and Joseph Silk. Particle Dark Matter: Evidence, Candidates and Constraints. *Phys. Rept.*, 405:279–390, 2005.

[GEA] GEA Ecoflex Gmbh. *GBS-Serie-Gelötete Plattenwärmetauscher*. https://www.ck-heiztechnik.de/media/kataloge/geaGEA-WTT%20Serie%20GBS%20%2002-13.pdf, 16.04.2018.

[Gei18] Christopher Geis. The XENON1T water Cherenkov muon veto system and comissioning of the XENON1T Dark Matter experiment. Doctor of sience, Institut für Physik Joahnnes Gutenberg-Universität Mainz, 2018. (to be published).

[Hax88] W. C. Haxton. ^{37}Ar as a calibration source for solar neutrino detectors. *PHYSICAL REVIEW C*, 38(5):2474–2477, NOVEMBER 1988.

[HD02] Wayne Hu and Scott Dodelson. Cosmic Microwave Background Anisotropies. *Ann. Rev. Astron. Astrophys*, 40:171–216, 2002.

[Hil14] Christopher Hils. "Studie von internen Kalibrationsmethoden für Flüssig-Xenon-TPCs zur direkten Suche nach Dunkler Materie". Diploma Thesis, Institut für Physik, January 2014.

[HvR09] Wilhelm Hrsg. v. Raith. *Sterne und Weltraum*. DE Gruyter, 2009.

[ise01] iseg Spezialelektronik GmbH. *NHQ x2xx Präzisions NIM Hochspannungsquelle der Baureihe NHQ HIGH PRECISON RS232-Interface Bedienungsanleitung*, 3.06 edition, February 2001. https://www.franke-iv.de/Iseg/manual%20NHQ%20High%20Precision.pdf.

[Jen12] Thomas Jennewein. Charakterisierung von Photomultiplier Tubes hinsichtlich deren Verwendung in Flüssig-Xenon Zeitprojektionskammern. Bachelor Thesis, Institut für Physik, May 2012.

[JRC12] JRC. *Karlsruhe Nuclide Chart*, 8 edition, 2012.

[K+75] R. Kishore et al. ^{37}Cl(p,n)^{37}Ar ar excitation function up to 24 mev: Study of (p,n) reactions*. *PHYSICAL REVIEW C*, 12(1):21–27, July 1975.

[Kap18] Wolfgang Kapferer. *Das Rätsel Dunkle Materie*. Springer, 2018.

[Kja12] Elvar Steinn Kjartansson. Realization of a System to Controle and Monitor the Operation of a Liquid Xenon Time Projection Chamber. Bachelor of sience, Institut für Physik Joahnnes Gutenberg-Universität Mainz, 2012. xenon.physik.uni-mainz.de/theses.html, 27.03.2018.

[KNF] KNF Neuberger Inc. *GAS SAMPLING PUMPS WITH KNF DOUBLE DIAPHRAGM SYSTEM*. https://www.knfusa.com/?type=5600&fileref=7478,16.04.2018.

[KVA67] Manzheli V.G. Komarenko V.G. and Radtsig A.V. Viskosität und Dichte von einwertigen n-Alkoholen bei niedrigen Temperaturen. *Ukr.Fiz.Zh.(Russ.Ed.)*, 12:681–685, 1967.

[Leya] Leybold Vacuum GmbH. *Oil-free Scroll Vacuum Pumps SCROLLVAC SC 5D, SC 15D SC 30D*, 171.70.02 edition. www.idealvac.com/files/brochures/Leybold-Scrollvac-SC15-60D_Brochure.pdf, 16.04.2018.

[Leyb] Leybold Vacuum GmbH. *Turbovac operating instructions*, ga05118_1302 edition. www.idealvac.com/files/brochures/Leybold_Turbovac_Operating_Instructions.pdf, 16.04.2018.

[M+10] A. Manalaysay et al. Spatially uniform calibration of a liquid xenon detector at low energies using ^{83m}Kr. *REVIEW OF SCIENTIFIC INSTRUMENTS*, 81(073303), 2010.

[M+17] E. M.Boulton et al. Calibration of a two-phase xenon time projection chamber with an ^{37}Ar soruce. *Submission to Jinst*, 26 June 2017.

[Mak17] David Maksimovic. Die Vermessung der Antwortfunktion von PMT und Elektronik für die MainzTPC, im Zusammenhang mit den XENON Dunkle Materie Experiment. Bachelor of sience, Institut für Physik Joahnnes Gutenberg-Universität Mainz, 2017. xenon.physik.uni-mainz.de/theses.html, 27.03.2018.

[Mor12] Matthias Morbitzer. Aufbau einer testkammer zur Chrakterisierung von Avalanche-Photodioden für eine flüssig Xenon TPC. Bachelor of sience, Institut für Physik Joahnnes Gutenberg-Universität Mainz, 2012. xenon.physik.uni-mainz.de/theses.html, 27.03.2018.

[N+07] K. Ni et al. Preparation of Neutron-activated Xenon for Liquid Xenon Detector Calibration. *Nucl. Instrum. Meth. A*, 582:569–574, 2007.

[Nat] National Institute of Standards and Technology. *NIST Chemistry WebBook, SRD 69*. https://webbook.nist.gov, 20.04.2018.

[Nuc] Nuclear Chemstry Johannes Gutenberg-Universität Mainz. *Technical Properties of the TRIGA-Mark-II*. www.kernchemie.uni-mainz.de/229.php,07.04.2018.

[Nyg76] David R. Nygren. The time-projection chamber -a new 4π detector for charged particles. *Lawrence Berkley Labrotaroy PEP*, 144, 1976.

[ORT] ORTEC. *Ortec General purpose-amplifier 570*. https://www.ortec-online.com/-/media/ametekortec/brochures/570.pdf, 11.05.2018.

[pan17] *pandas, Python Data Analysis Library*, 0.22.0 edition, 2017. https://pandas.pydata.org, 25.04.2018.

[Phia] Phillips Scientific. *Octal Disciminator NIM MODEL 705*. www.phillipsscientific.com/pdf/705ds.pdf,17.04.2018.

[Phib] Phillips Scientific. *Quad Majority Logic Unit, NIM Model 755*. www.phillipsscientific.com/pdf/755.ds.pdf, 16.05.2018.

[S+03] V.N. Solovov et al. Measurement of the refractive index and attenuation length of liquid xenon for its scintillation light. *Nucl. Instrum. Meth.*, A(516):462–474, 2003.

[S+11] M. Szydagis et al. NEST: A comprehensive model for scintillation yield in liquid Xenon. June 2011.

[S+13] M. Szydagis et al. Enhancement of NEST capabilities for simulating low-energy recoils in liquid Xenon. July 2013.

[S+15] S. Stephenson et al. MiX: A position sensetive dual-phase liquid xenon detector. *JINST*, 10(P10040), October 2015.

[sae02] saes getters. *PS4-MT3/15-R/N Specifications*, May 2002. www.saespuregas.com/Library/documents/s110-243_rev_528.pdf.

[Sch12] Marc Schumann. Dark matter search with liquid noble gases. June 2012.

[Sch13] Melanie Scheibelhut. Aufbau und Simulation eines Comptonstreuexperiments mit einem Xenon- und Germaniumdetecktor. Diploma thesis, Institut für Physik Joahnnes Gutenberg-Universität Mainz, 2013. xenon.physik.uni-mainz.de/theses.html, 27.03.2018.

[SISa] SIS GmbH. *PCICPCI-VME LINKINTERFACE*. www.struck.de/pcivme.html,16.04.2018.

[SISb] SIS GmbH. *SIS3305 VME Digitizer User Manual*. http://daq-plone.triumf.ca/HR/VME/SIS/sis3305-M-0x1009-1-v120.pdf,16.04.2018.

[SISc] SIS GmbH. *SIS3316 16 CHANNEL VME DIGITIZER FAMILY*. www.struck.de/sis3316.html,16.04.2018.

[Sisd] Pierre Sissol. "MainzTPC- Detector Commissioning and Study of the Low-Energy Respons of Electronic Recoils in Liquid Xenon for Dark Matter Applications". PhD Thesis, Institut für Physik. (to be published).

[Sis12] Pierre Sissol. Monte-Carlo-Simulationen eines Compton-Streuexperiments zur Messung der Szintillations- und Ionisationseigenschaften von flüssigem Xenon mit einer Zwei-Phasen-Xenon-Zeitprojektionskammer. Diploma Thesis, Institut für Physik, June 2012.

[Sma16] Smartec. *Universal Transducer Interface Datasheet*, December 2016. http://www.smartec-sensors.com/cms/media/Datasheets/UTI%20interface/UTI_datasheet.pdf.

[Sol] SolidWorks Corporation. *SolidWork Website*. www.solidworks.de,20.04.2018.

[Spe] Spellman High Voltage Electronics Corporation. *Bertan 225 HIGH VOLTAGE POWER SUPPLY*. https://www.spellmanhv.com/-/media/en/Products/225.pdf?la=en, 16.04.2018.

[Swa] Swagelok. *VCR Metal Gasket Face Seal Fittings*. https://www.swagelok.com/downloads/webcatalogs/en/MS-01-24.pdf,16.04.2018.

[Tel] Teledyne Hastings Instruments. *HFM-300 FLOW METER, HFM-302 FLOW CONTROLLER*. www.teledyne-hi.com/resourcecenter/Documents/Manuals/151-HFM-300_HFC-302_Manual.pdf,16.04.2018.

[Tex] Texas Instruments. *LOW DISTORTION, CURRENT-FEEDBACK AMPLIFIER THS3201*. www.ti.com/lit/ds/slos416c/slos416c.pdf,16.04.2018.

[UR16] Teresa Marrodan Undagoitia and Ludwig Rauch. Dark matter direct-detection experiments. *J. Phys.*, G43(01), 2016.

[vD+18] Pieter van Dokkum et al. A gaaxy lacking dark matter. *Nature*, 555:629–632, 29. March 2018.

[W+85] R. O. Weber et al. Cross sections and thermonuclear reactions rates of proton-induced reactions on ^{37}Cl. *Nuclear Physics*, A439:176–188, 1985.

[XEN] XENON Collaboration. *PAX Processor for Analyzing Xenon*. https://github.com/XENON1T/pax, 25.04.2018.

[Zac07] Viktor Zacek. Dark Matter. *arXiv:0707.0472 [astro-ph]*, 2007.